Development of a Planar Piecewise Continuous Lumped Muscle Parameter Model for Investigation of Joint Stiffness in Walking on a Level Surface

by

Qianyi Fu

A dissertation submitted in partial fulfillment
of the requirements for the degree of
Doctor of Philosophy
(Industrial and Operations Engineering)
in the University of Michigan
2020

Doctoral Committee:

Professor Thomas J. Armstrong, Co-Chair
Professor Albert J. Shih, Co-Chair
Research Professor James A. Ashton-Miller
Associate Professor Bernard J. Martin

Qianyi Fu

qifu@umich.edu

ORCID iD: 0000-0002-4623-3550

DEDICATION

To my mother, father, wife, and daughter Michi E. Fu

ACKNOWLEDGMENTS

This dissertation was completed thanks to the help, support, and guide of many people. First, I want to thank my advisors Dr. Thomas J. Armstrong and Dr. Albert Shih for all their support and guidance through the years of my Ph.D. Dr. Armstrong has provided tremendous guidance and how to think like a professional researcher. Dr. Shih has kindly provided lots of support and time to help me through the difficulties in both life and academia. I appreciate your advice that helps me grow as a researcher. I would also like to thank the members of my dissertation committee, Dr. Bernard Martin, Dr. James Ashton-Miller, and Dr. Clive D'Souza. All of your suggestions and comments made this dissertation better.

I am grateful to my colleagues, Robert Chisena and Deema Totah, under the NSF Cyber-Physical Service System for 3D-Printing of Adaptive Custom Orthoses Project (PFI:BIC project #1534003) for their support and guidance. I am also grateful to Darren Bolger and Jeff Wensman, who work at the University of Michigan Orthotic and Prosthetic Center for their help on recruiting patients and providing ideas.

To my fellow Ph.D. students and labmates, Miguel Funes, Yadrianna Acosta, Michael Daly, Aanya Agarwal, Na Du, Teerachart Soratana, Kieran Obrien, Nicholas Sandhu, Yidu Lu, Kamolnat Tabattanon, Yifan Li, Rosemarie Figueroa, Vernnaliz Carrasquillo, Yuzhi Wan, Justin Young, Brandon Pitts, thank you for your advice on both life and research during my Ph.D. years. Especially, Miguel Funes figured out the hardware for the inertial measurement unit mounted on the ankle-foot orthosis, Yadrianna Acosta helped me with the electromyogram setup

for my experiment, Michael Daly developed the basis of the webpage presented in this dissertation, and Aanya Agarwal assisted on subject recruitment and most of the data collection.

I am grateful to all faculty and staff in the Department and the Center for Ergonomics. A special thanks to Charles Wooley, Matt Ireland, Tina Picano Blay, Chris Konrad, Eyvind Claxton, Olof (Mint) Minto, and Rodney Capps for their steady support.

Last but not least, thanks to the support from my family, especially to my father and mother, for their support and encouragement!

TABLE OF CONTENTS

DEDICATION ii
ACKNOWLEDGMENTS iii
LIST OF TABLES vi
LIST OF FIGURES viii
LIST OF APPENDICES xi
ABSTRACT xii
CHAPTER 1 Introduction 1
1.1. Overview 1
1.2. Aims 1
1.3. Background and Significance 2
1.4. Dissertation Organization 5
CHAPTER 2 A Planar Piecewise Continuous Lumped Muscle Parameter Model for Prediction of Walking Gait with Passive-Dynamic Ankle-Foot Orthosis 6
2.1. Introduction 7
2.2. The Planar Piecewise Continuous Lumped Muscle Parameter (PPCLMP) Model 8
2.2.1. Lumped Muscle Parameters 12
2.2.2. Single Stance Phase 13
2.2.3. Double Stance Phase 14
2.2.4. Swing Phase 16
2.2.5. Phases Continuity – Forward Dynamics 17
2.2.6. Initial Conditions at the Right TO 19
2.2.7. Sensitivity Analysis 20
2.2.8. Summary of the Planar Piecewise Continuous Lumped Muscle Parameter (PPCLMP) Model 27
2.3. Experiment Setup 28
2.4. Results 30
2.4.1. Pilot Study 31
2.4.2. Model Prediction for Six Subjects 38

2.5. Discussion 39
2.5.1. Knee ROM 40
2.5.2. Hip ROM and Step Length 41
2.5.3. Swing and Stance Time 42
2.5.4. Model Applications, Assumptions, and Limitations 42
2.6. Conclusions 46
CHAPTER 3 Utilization of the Inertial Measurement Unit for Evaluation of Gait with Passive Dynamic Ankle-foot Orthosis based on the PPCLMP Model 47
3.1. Introduction 48
3.2. Algorithm for Estimating Initial Conditions and Lumped Muscle Parameters based on IMU Data – Inverse Dynamics 51
3.2.1. Overview 51
3.2.2. Framework for Gait Event Identification and Angle Estimation 52
3.2.3. Optimization Problem for Searching the Initial Conditions and Lumped Muscle Parameters 54
3.2.4. Sensitivity Analysis 60
3.2.5. Algorithm Summary 62
3.3. Subjects and Methods 62
3.4. Results 65
3.4.1. Observed and Estimated Initial Joint Angles and Angular Velocities 65
3.4.2. Estimated Lumped Muscle Parameters 67
3.4.3. Observed and Predicted Gait Parameters 68
3.4.4. Gait Symmetry and Efficiency for Evaluation 70
3.5. Discussion 74
3.5.1. Initial Joint Angles and Angular Velocities Differences 74
3.5.2. Estimated Lumped Muscle Parameters 74
3.5.3. Gait Parameters 75
3.5.4. Evaluation of Gait with AFOs 78
3.5.5. Limitations 80
3.6. Conclusions 81
CHAPTER 4 An Investigation of Gait Prediction Accuracy of the PPCLMP Model 82
4.1. Introduction 84
4.2. Methods 86

4.2.1. Subjects 86
4.2.2. Procedure 86
4.2.3. Data Collection 87
4.2.4. Data Processing 89
4.2.5. Statistical Analysis 91
4.3. Results 92
4.3.1. RMSE between Observed and Predicted Results 93
4.3.2. ANOVA 93
4.3.3. Accuracy of Initial Conditions 95
4.3.4. Accuracy of Lumped Muscle Parameters 95
4.3.5. Accuracy of Step Lengths and Swing Time 95
4.3.6. Accuracy of Gait Symmetry Index (SI) 97
4.3.7. Accuracy of Walking Speed 98
4.4. Discussion 98
4.4.1. Accuracy of the Initial Conditions and Lumped Muscle Parameters 98
4.4.2. Accuracy of the Step Lengths, Swing Time, Gait Symmetry, and Walking Speed 101
4.4.3. Other Subject Variables 101
4.4.4. Limitations and Future Work 102
4.5. Conclusions 102
CHAPTER 5 Discussion 104
5.1. Broader Applications 104
5.1.1. Developing a Decision Support System of AFO Design 104
5.1.2. Developing a Cyber-based System for AFO Evaluation 106
5.1.3. Investigating of Joint Stiffness 107
5.2. Suggestions for Future Work 109
CHAPTER 6 Conclusions 113
APPENDICES 118
REFERENCE 145

LIST OF TABLES

Table 2-1: The link-length and link-mass ratios used to estimate the link lengths and masses for simulation, and the measured link lengths and estimated link masses for the male subject in Section 2.3 12

Table 2-2: Summary of lumped muscle parameters in the model 13

Table 2-3: Summary of variables and equations used in Appendix A to solve the movement during the DS 16

Table 2-4: Summary of observed joint angles for hip, knee, and ankle, joint angular velocities for hip and knee at right TO, and the step length (S_L) to stature (L_0) ratio during the walking gait. . 22

Table 2-5: Range of initial conditions for the sensitivity analysis and simulation 24

Table 2-6: The statistics of sensitivity analysis output (error vectors and gait parameters) and the percent contributions of variations in initial state vectors to variations in error vectors and gait parameters for all 918 valid combinations of initial state vectors. 26

Table 2-7: Summary of AFO stiffness, error vectors, and comparisons between observed (O) and predicted (P) initial conditions for simulations (hip flexion/extension with +/–; knee flexion with +). The errors were estimated with the scalar factor, *f*, equal to 0.1 seconds 32

Table 2-8: Correlation coefficient (CC) and root mean square error (RMSE) between observed and predicted ankle, knee, and hip flexion angles for 10 complete gait cycles 34

Table 2-9: Comparison between the observed (O) and predicted (P) range of motion (ROM) for knee and hip angles 35

Table 3-1: Summary of 10 lumped muscle parameters in the model. 58

Table 3-2: Ranges of the initial conditions and lumped muscle parameters for the enumeration method and the ranges of AFO stiffness and subject parameters for the sensitivity analysis. 60

Table 3-3: Percent contribution of variations in the initial conditions, lumped muscle parameters, AFO stiffness, gender, stature, and body mass to variations in gait parameters. 62

Table 3-4: Anthropometry of Subjects 1 and 2 and the stiffnesses of AFOs used in the experiment 63

Table 3-5: Summary of the estimated swing time, stance time, and shank pitch angles and angular velocities at TOs and HS for the impaired leg based on the IMU attached to the impaired-side shank. 66

Table 3-6: Comparison of initial impaired-leg hip and ankle joint angles and angular velocities between observed values (O) and predicted (P) values. 66

Table 3-7: Statistics of lumped muscle parameters of the hip and knee joints, k_{ijp}, in Nm/deg, and ankle joints, r_{i32}, in Nm/kg summarized in Table 3-2. 68

Table 3-8: Summary of the observed (O) and predicted (P) gait parameters. 69

Table 4-1: Anthropometry of six subjects 86

Table 4-2: ANOVA table for independent variables with significant effects ($p < 0.05$). L represents the left side, R represents the right side, M represents the male, and F represents the female. The significant effect of gender is shown as pooled value comparisons between males and females. The significant effect of stature is shown as the first-order coefficient and the intercept from ANOVA. The body mass and the interaction terms had no significant effect on the dependent variables. 94

Table 4-3: The correlation coefficients between the stature and ε_{IC} of initial angles and angular velocities. The ε_{IC} of all initial angles and angular velocities were ANOVA-significant ($p < 0.05$) affected by stature except the ε_{IC} of the initial back-ankle angle ($\theta_{13}(t0)$). 95

Table 4-4: The r_{EMG} during the SW and DS for six subjects. The L and R for r_{EMG} during DS represent the side of the back-leg. 95

Table 4-5: Calculated gait symmetry indices (SIs) for observed (O) and predicted (P) step lengths and swing time of six subjects. 97

Table B1: Combinations of joint angles (θ_{22} = 20 deg) 128

Table B2: Combinations of joint angles (θ_{22} = 25 deg) 129

Table B3: Combinations of joint angles (θ_{22} = 30 deg) 130

Table B4: Combinations of joint angles (θ_{22} = 35 deg) 131

Table B5: Combinations of joint angles (θ_{22} = 40 deg) 132

Table B6: Combinations of joint angles (θ_{22} = 45 deg) 133

Table B7: Combinations of joint angular velocities 134

Table C1: The slope, intercept, and goodness of fitting of the linear regression between reaction torque and bending angle 137

Table D1. Observed (O) and predicted (P) initial angles (initial shank pitch angle $\theta(t_0)$, back-hip angle $\theta_{11}(t_0)$, and back-ankle angle $\theta_{13}(t_0)$) and angular velocities (shank pitch angular velocity $\dot{\theta}(t_0)$, back-hip angular velocity $\dot{\theta}_{11}(t_0)$, and back-ankle angular velocity $\dot{\theta}_{13}(t_0)$) for 40 gait cycles (n = 40) for each subjects under each condition. 138

Table E1. The measured SEMG root mean square (RMS) for left biceps femoris (lBF), left rectus femoris (lRF), right biceps femoris (rBF), and right rectus femoris (rRF), and the predicted hip and knee lumped muscle parameters during the SW and DS. n = 40 for each subject under each condition. 140

Table F1. Observed (O) and predicted (P) step lengths, swing time, and walking speed for six subjects with 40 gait cycles (n = 40) for each subject under each condition. 142

LIST OF FIGURES

Figure 1-1: Definitions of gait phases reprinted from [9]. 3

Figure 2-1: The phases and events of the left (red) and right (green) legs during a gait cycle: the gait starts from the right TO, then to the right SW and left SS, then to the right HS, then to the DS (right leg in front), then to the left TO, then to the right SS and left SW, then to the left HS, then to the DS (right leg in the back), and then back to the right TO (start of the gait). 9

Figure 2-2: (a) Biomechanical model with definitions of limb links, joints, and joint angles in the sagittal plane and (b) the foot anatomy and dimensions in the sagittal plane (part of the image adopted from [52]). 11

Figure 2-3: Summary of state vectors transferred between phases and forces and equations related to each phase assuming the AFO is on the left ankle. Top diagrams represent the joint angles and lumped muscle parameters related to the right leg (solid black) movement during each phase: (a) The right leg movement during the SW is simulated by a double-pendulum with two rotational springs on the knee and hip joints, from right TO (t_0) to right HS (t_1), (b) the leg movements during the DS are simulated by a kinematic chain model with the right leg in front, from right HS (t_1) to left TO (t_2), (c) the right leg movement during the SS is simulated by an inverted pendulum, from left TO (t_2) to left HS (t_3), and (d) the leg movements during the DS are simulated by a kinematic chain model with the right leg in the back, from left HS (t_3) to right TO (t_4). 15

Figure 2-4: Flowchart of the proposed PPCLMP model for predicting gait parameters. 28

Figure 2-5: Marker settings for the controlled experiment. 30

Figure 2-6: Comparisons between the observed (n = 10) and predicted hip flexion angles for the left and right legs under each condition. The presented phase blocks are colored based on the model-predicted time of SS, SW, and DS. 33

Figure 2-7: Comparisons between the observed (n = 10) and predicted knee flexion angles for the left and right sides under each condition. The presented phase blocks are colored based on the model-predicted time of SS, SW, and DS. 33

Figure 2-8: Comparisons between the observed (n = 10) and predicted ankle flexion angles for the left and right sides under each condition. The presented phase blocks are colored based on the model-predicted time of SS, SW, and DS. 34

Figure 2-9: Comparisons between the observed and predicted step length for left (AFO) and right sides under each condition (n = 10). Values are mean ± SE. 36

Figure 2-10: Comparisons between the observed and predicted swing time for left (AFO) and right sides under each condition (n = 10). Values are mean ± SE. 37

Figure 2-11: Comparisons between observed and predicted stance time for left (AFO) and right sides under each condition (n = 10). Values are mean ± SE..... 37

Figure 2-12: Comparison between observed and predicted step lengths for left (AFO) and right sides under each condition for six subjects (n = 40). Values are mean ± SE. 38

Figure 2-13: Comparison between observed and predicted swing time for left (AFO) and right sides under each condition for six subjects (n = 40). Values are mean ± SE. 39

Figure 2-14: Hill muscle model that contains a contractile element (CE), a series spring element (SE), and a parallel spring element (PE). Diagram downloaded from [167]..... 44

Figure 3-1: The global coordinate system (x_0-, y_0-, and z_0-axes) and local coordinate system (x-, y-, and z-axes) of the IMU defined in this study from (a) the side view of the IMU-attached AFO and (b) the back view of the IMU-attached AFO, and (c) the local coordinate system of the IMU attached to the back of the AFO calf rotating with respect to the global coordinate system in the sagittal plane (side view). 50

Figure 3-2: The framework for gait event identification and angle estimation based on accelerations, angular velocities, and headings measured by the IMU. The peaks of resultant acceleration measured from the accelerometer are used to identify the gait events and calculate swing and stance time. The angular velocities measured from the gyroscope and the headings measured from the magnetometer are used to calculate the shank pitch angle and angular velocities. The swing and stance time and shank pitch angles and angular velocities then are used as the constraints in the optimization problem to find the optimal initial conditions and lumped muscle parameters..... 53

Figure 3-3: The optimization problem for searching the optimal initial conditions and lumped muscle parameters for model prediction and gait evaluation based on the estimated swing time, stance time, and shank pitch angles and angular velocities at identified gait events to minimize estimated total energy expenditure. 54

Figure 3-4: The geometry and angle definitions at the impaired-side TO, t_0, as shown in Figure 3-2. 56

Figure 3-5: IMU attachment for the LEGSys^{TM}: one IMU on each thigh, one on each shank, and one on the lower back trunk..... 65

Figure 3-6: Observed and predicted SI under all conditions based on mean step lengths. Values are mean ± SE. 71

Figure 3-7: Observed and predicted SI under all conditions based on mean swing time. Values are mean ± SE. 72

Figure 3-8: Observed and predicted walking speed under all conditions as summarized in Table 3-8. Values are mean ± SE..... 73

Figure 3-9: Predicted energy expenditure under all conditions. Values are mean ± SE. 73

Figure 4-1: Equipment for measuring movements and muscle activities of the BF and RF: (a) the placement of vision-based motion tracking markers from the side view, (b) the IMU attached to the back of the AFO calf, and (c) the placement of four SEMG units on lBF, lRF, rBF, and rRF. 89

Figure 4-2: Amplified SEMG RMS during a sample gait of Subject 3 under the NAFO condition. TO represents the toe-off, HS represents the heel strike, SW represents the swing phase, SS represents the single stance phase, DS1 represents the doubles stance phase with right leg behind, and DS2 represents the double stance phase with left leg behind, lBF represents the left biceps femoris, lRF represents the left rectus femoris, rBF represents the right biceps femoris, and rRF represents the right rectus femoris. The top table shows the mean and standard deviation of the SEMG RMS during each phase that are used to compare with the associated lumped muscle parameters. 91

Figure 4-3: The range of errors of predicted step lengths for subjects with different statures (all conditions pooled). 96

Figure 4-4: The range of errors of predicted swing time for subjects with different statures (all conditions pooled). 96

Figure 4-5: The range of errors of predicted SIs for step length and swing time of subjects with different statures (all conditions pooled). 97

Figure 4-6: The range of errors of predicted walking speed for subjects with different statures (all conditions pooled). 98

Figure 5-1: Workflow for predicting AFO stiffness effect on gait and searching for optimal AFO stiffness. 105

Figure 5-2: Overview of a cyber-based AFO design and evaluation system 107

Figure 6-1: Overview of the model inputs (orange) and model outputs (blue). 114

Figure 6-2: The scope of investigations on model inputs and outputs in Chapters 2, 3, and 4. . 117

Figure A1: Diagram of DS posture with the right leg in front 119

Figure A2: Diagram of forces and torque that applied to the left foot 121

Figure A3: Diagram of forces and torque that applied to the left lower leg 123

Figure A4: Diagram of forces and torque that applied to the left upper leg 125

Figure A5: Diagram of forces and torque that applied to front-leg (right) 126

Figure C1: Component of the SMApp machine developed by Barton Research Group at the University of Michigan 135

Figure C2: The stiffness plots for (a) AFO1 before the trials, (b) AFO1 after the trials, (c) AFO2 before the trials, and (d) AFO2 after the trials 136

Figure G1. The webpage with input predicted animation of gait and joint angles for demonstration of model application 144

LIST OF APPENDICES

Appendix A: Modeling of the Kinematic Chain during DS 118
A1. Geometry 118
A2. Free Body Diagram – Back-Foot (Left) 120
A3. Free Body Diagram – Back-Lower-Leg (Left) 122
A4. Free Body Diagram – Back-Upper-Leg (Left) 124
A5. Free Body Diagram – Front-Leg (Right) 126
A6. Summary 127
Appendix B: List of Combinations for Sensitivity Analysis in Chapter 2 128
Appendix C: AFO Stiffness Test. 135
Appendix D: Observed and IMU Predicted Shank Pitch Angles and Angular Velocities in Chapter 4 138
Appendix E: Measured Electromyography (EMG) Signals and the Estimated Hip Lumped Muscle Parameters during the Swing Phase (SW) and Double Stance Phase (DS) 139
Appendix F: Observed and Predicted Gait Parameters in Chapter 4 141
Appendix G: Webpage for Demonstration of Model Application 143

ABSTRACT

When joint stiffnesses are affected by injuries or illnesses they can interfere with gait and with activities of daily living, work, and leisure. Biomechanical models have been proposed for describing the effects of these conditions and various interventions on the different phases of gait.

This dissertation reports the development of a planar piecewise continuous lumped muscle parameter (PPCLMP) model for investigating how different joint stiffnesses affect the gait phases individually and collectively. The proposed PPCLMP model characterizes the movements of lower limbs during each gait phase by a simplified dynamic system: the single stance phase by an inverted pendulum, the double stance phase by a kinematic chain, and the swing phase by a double pendulum. The model uses lumped muscle parameters to characterize the joint torques during each phase. The phase continuity is achieved by setting the joint angles and angular velocities at the end of one phase equal to those at the start of the next phase. The model can predict gait movements from given initial conditions (initial joint angles and angular velocities), anthropometry, lumped muscle parameters, and joint stiffness in a forward-dynamic mode. Also, if the gait movements are known, the model could estimate the lumped muscle parameters in an inverse-dynamic mode.

In the first study, the model was used in the forward-dynamic mode to predict joint angles and gait parameters for six healthy subjects' anthropometry, ankle joint stiffnesses (without ankle-foot orthosis (AFO), with a low-stiffness AFO, and with a high-stiffness AFO),

initial conditions, and constant lumped muscle parameters. Results showed that the trend of gait parameters changings (longer step length and shorter swing time on the AFO-side for higher AFO stiffness) with different AFO stiffnesses were qualitatively well predicted by the model but quantitative prediction accuracy was limited (the mean errors were 0.15 m and 5% for the predicted step length and swing time, respectively) due to the constant values of lump muscle parameters.

The second study examined the use of the model in an inverse-dynamic mode using data from a single inertial measurement unit (IMU) attached to the lower shank in order to estimate the initial conditions and lumped muscle parameters for each gait cycle. These were used by the model in the forward-dynamic mode to enhance the gait prediction. Results from two patients wearing AFOs demonstrated that the model prediction was markedly improved comparing with the first study by utilizing the inverse-dynamic mode as the mean RMSE was 0.07 m and 2% for predicted step length and swing time, respectively.

The third study investigated the PPCLMP model prediction accuracy using the inverse- and forward-dynamic processes proposed in the second study. Three male and three female healthy subjects were recruited to walk with IMU-instrumented AFOs on their left feet to measure step lengths and swing time, while surface electrodes measured selected muscle activities for comparison with lumped muscle parameters. Results showed that the model prediction accuracy of step lengths and walking speed improved significantly ($p < 0.05$) with increasing stature; however, model prediction accuracy of swing time unaffected by stature.

It was concluded that the PPCLMP model of gait has the potential for predicting how the prescription of an AFO of a given stiffness will affect gait, but more research is needed to refine model predictions by improving the representation of joint torques during gait.

CHAPTER 1 Introduction

1.1. Overview

Joint stiffness that describes the linear relationship between joint torques and joint angles can be affected by impairments, assistive devices, and activities [1–4]. Biomechanical models of human walking gait can be used to characterize joint stiffness and predict gait performance. These models are useful in investigating how the change of joint stiffness, like suffering from muscle spasticity or wearing ankle-foot orthosis (AFO), affects gait. This thesis develops and evaluates a planar piecewise continuous lumped muscle parameter (PPCLMP) model that characterizes gait phases as continuous dynamic systems and lumps joint muscle forces to simplify the analysis of human gait and predict gait with different joint stiffnesses based on the kinematic data measured from an inertial measurement unit (IMU) attached to the AFO.

1.2. Aims

The general aim of this work is to develop and evaluate the PPCLMP model that can be used to predict walking gait based on anthropometry, lumped muscle parameters, joint stiffness (ankle with AFO as an example), and the initial conditions (initial joint angles and angular velocities) of the gait. To achieve this aim, the following objectives are established:

1. Develop a PPCLMP model that predicts how joint stiffness affects gait via forward dynamics.

2. Utilize IMU data to estimate the initial conditions and lumped muscle parameters of each gait cycle via inverse dynamics to enhance the model prediction of gait.

3. Evaluate the model prediction accuracy for various anthropometric inputs by comparing predicted gait parameters with measurements.

1.3. Background and Significance

Joint stiffness change and underlying pathologies have been identified based on observations of gait patterns by clinicians as movements and gait patterns reveal much about the physical and behavioral aspects of individuals [5–7]. For example, stroke patients may tend to circumduct or lift their legs as a result of increasing joint stiffnesses in their ankle and knee [5,8].

To learn the mechanism of human gait, gait patterns are commonly divided into “stance” and “swing” phases as shown in Figure 1-1 [9]. The stance phase accounts for approximately 60% of the total gait cycle and begins at the heel strike (HS), which is the instance that the heel of the forward-moving foot makes contact with the walking surface. This phase continues while the foot is in contact with the walking surface and ends when the foot leaves the walking surface at “toe-off” (TO). The swing phase (SW) begins at the TO and ends at the HS. The stance and swing phases alternate between the right and left legs during gait. Since there are overlaps between the stance phases of the right and left legs, investigators have further divided the stance phase into two phases: 1) single stance phase (SS) when only one leg is in stance phase and 2) double stance phase (DS) when both legs are in stance phase [10–12]. These definitions help when building biomechanical models for characterizing movements during each phase of walking gait.

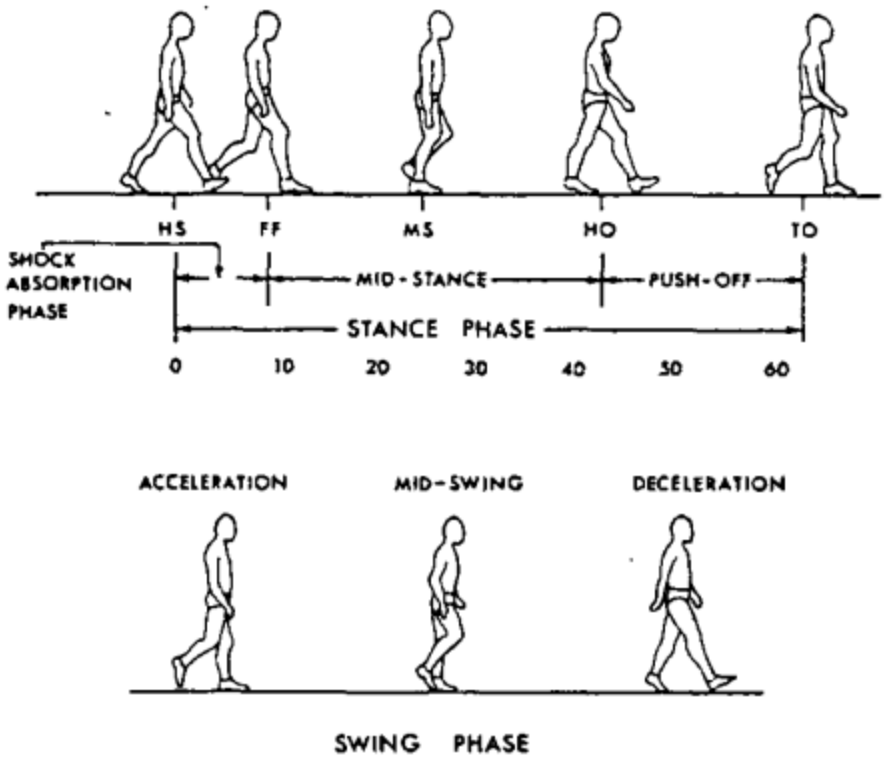

Figure 1-1: Definitions of gait phases reprinted from [9].

Biomechanical models have been developed to characterize, predict, and study various aspects of human gait movement [10,13–15]. The human body is characterized as an array of link lengths, l_j, and time-dependent joint angles, $\theta_{ij_{x,y,z}}(t)$, in biomechanical models [13,16–18]. These biomechanical models can be used to describe the spatial and temporal relationship between the segments of the body during walking [19]. Further, biomechanical models can explain how individual physical attributes, behavior attributes, task attributes, and environmental attributes affect biomechanical loads and contribute to gait performance [20–22]. Common approaches using biomechanical models to study walking gait include: 1) dividing the walking gait into separate phases, 2) characterization of the legs as a series of links, 3) adding inertial properties to lower limbs, and 4) adding muscle forces to joints.

By adding inertial properties to lower limbs, models have been developed to characterize lower limb movements during the SS by an inverted pendulum [13,23–25]. The inverted pendulum models were attempts to simplify gait in order to investigate leg movements. However, these models for the SS assume no active joint torques, which is not true for the SW and DS.

Biomechanical models have been developed to investigate lower limb movements during the SW and DS by characterizing hip, knee, and ankle joint torques as they were found to be related to gait performance and stability [26–28]. Double pendulum models were proposed to calculate the duration of SW and step length by characterizing the movements of lower limbs during the SW by a double pendulum with torques on the hip and knee joints [29–33]. Kinematic chain models have been used to characterize the lower limb movements during the DS with the active push-off torque at the back-ankle [34,35].

However, all these models focus on a specific phase or aspect of normal walking gait and are not used to investigate how different joint stiffnesses resulted from impairments and wearing assistive devices could affect movements across the whole gait cycle. This work contributes a planar piecewise continuous lumped muscle parameter, PPCLMP, model describing how anthropometry, lumped muscle parameters, joint stiffness, and initial conditions of gait contribute to gait performance across the entire gait cycle by using gait with an AFO as an example. The proposed model could be used to:

- Predict the effect of different joint stiffnesses on step length and swing time
- Utilize IMU data to estimate initial conditions and lumped muscle parameters for each gait cycle to enhance model prediction

- Evaluate AFOs for gait performance based on predicted gait performance concerning gait efficiency and symmetry

1.4. Dissertation Organization

The remainder of the dissertation has four additional chapters. Chapter 2 derives the PPCLMP model and demonstrates the model in the forward-dynamic mode for gait prediction. Chapter 3 derives an algorithm that uses the model developed in Chapter 2 in the inverse-dynamic mode to estimate the initial conditions and lumped muscle parameters for each gait cycle based on the kinematic data measured from an IMU attached to the AFO. Chapter 4 examines the model prediction accuracy of walking gaits with AFOs for males and females of various sizes. Chapter 5 discusses model applications and suggests future work regarding the proposed model. Chapter 6 summarizes the dissertation.

CHAPTER 2 A Planar Piecewise Continuous Lumped Muscle Parameter Model for Prediction of Walking Gait with Passive-Dynamic Ankle-Foot Orthosis

Abstract

This work proposes a planar piecewise continuous lumped muscle parameter (PPCLMP) model for predicting human walking gait with the passive-dynamic ankle-foot orthosis (AFO) based on forward dynamics. The model characterizes the sagittal-plane movement of the lower limbs during the single stance phase as an inverted pendulum, the double stance phase as a kinematic chain, and the swing phase as a double pendulum. For the normal gait, the model-predicted step length was sensitive (> 1% contribution) to the initial joint angle, and the predicted swing and stance time were sensitive to the initial angular velocity. To demonstrate the model could predict how different AFO stiffnesses affect gait in the forward-dynamic mode and validate the results, two AFOs with low (3.4 Nm/deg) and high (6.9 Nm/deg) stiffnesses were tested on seven healthy subjects (four males and three females) for level-walking. The model successfully predicted that the high-stiffness AFO resulted in longer step length and shorter swing time on the side wearing the AFO comparing to the gait with the low-stiffness AFO. The same trend was found in the experimentally observed step length and swing time. The model was good at qualitatively predicting the trend of three gait parameters (step lengths, swing time, and stance time) changing with different AFO stiffnesses but limited on quantitative prediction accuracy due to the constant values of lump parameters.

2.1. Introduction

Gait impairments that affect walking interfere with activities of daily living, work, and leisure. One of the leading gait impairment syndromes is the drop foot, and stroke is the leading cause of the drop foot syndrome. Approximately 795,000 people suffer a new or recurrent stroke each year [36], and 20% to 30% of stroke patients are affected by drop foot during their rehabilitation [37]. Drop foot affects patients' gait and abilities to participate in regular daily activities safely. To help improve and restore normal gait functions for drop foot patients, passive-dynamic ankle-foot orthoses (AFOs) are commonly used as assistive devices. The bending stiffness of AFO has been found to be the main factor that affects the patient's gait performance [38–41]. Currently, determining the ideal stiffness of an AFO for a patient is a subjective process based on the observation and experience of clinicians, as well as feedback from the patient. A knowledge gap addressed in this chapter is how or if the stiffness of the prescribed AFO would improve the patient's gait is barely predictable.

Biomechanical modeling has been investigated in quantifying the walking gait to aid clinicians in evaluating gait after treatment. The gait for walking is commonly divided into single stance phase (SS), double stance phase (DS), and swing phase (SW). Detailed biomechanical models have been built to characterize the leg movements in SS, DS, and SW. The SS was characterized by the inverted pendulum model with the leg rotating about the ankle joint [13,23–25]. The DS was characterized by a kinematic chain model with both feet constrained on the ground [34,35]. The SW was characterized by a double pendulum model with the upper leg as the upper pendulum and lower leg as the lower pendulum [29–33]. However, the ability to combine these models into a continuous gait model for the whole gait prediction is still missing. The goal of this work, therefore, is to develop a planar piecewise continuous lumped muscle

parameter (PPCLMP) model in which each leg is continuously looped from SW to DS to SS to DS, and then back to SW. The concept of piecewise continuous proposed by Fu et al. [42] specifies that the joint angles and angular velocities of hips, knees, and ankles at the end of one phase should be equal to those values at the start of the next phase. After being given the initial hip, knee, and ankle joint angles and angular velocities at the start of SW, the PPCLMP model should be able to predict the joint angles and angular velocities as well as the step lengths, swing time, and stance time throughout the walking gait cycle.

Toward this end, the goal of this study is to develop a PPCLMP model to predict human walking gait, as well as the effect of AFO stiffness on gait performance. Section 2.2 derives the PPCLMP model. Section 2.3 outlines the experimental setup to measure the human walking gait. Section 2.4 compares the model-predicted and the experimentally observed gait parameters of a healthy male subject. Section 2.5 discusses the model prediction accuracy, potential applications, and limitations.

2.2. The Planar Piecewise Continuous Lumped Muscle Parameter (PPCLMP) Model

As shown in Figure 2-1, the model simulates each gait cycle starting from and ending at the right toe-off (TO). For the right leg, the gait loops from SW to DS to SS to DS, and then back to SW. Accordingly, for the left leg, the gait loops from SS to DS to SW to DS, and then back to SS. Between the right TO and the right heel strike (HS) are the right SW and left SS. After the right HS and before the left TO is the DS with the right leg being the front-leg. After the left TO and before the left HS are the right SS and left SW. After the left HS and before the right TO is the DS with the right leg being the back-leg.

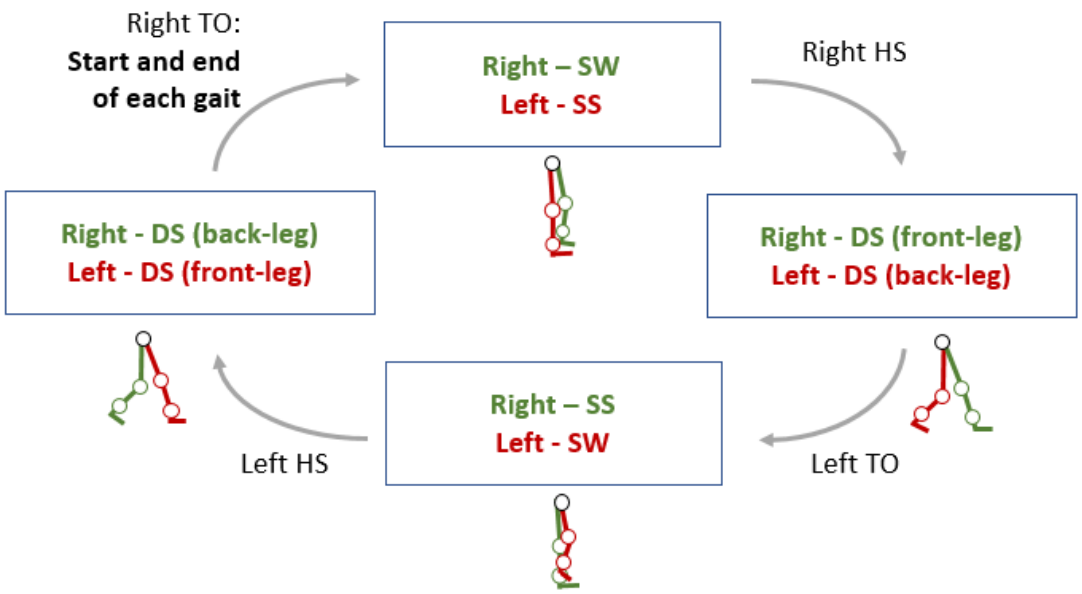

Figure 2-1: The phases and events of the left (red) and right (green) legs during a gait cycle: the gait starts from the right TO, then to the right SW and left SS, then to the right HS, then to the DS (right leg in front), then to the left TO, then to the right SS and left SW, then to the left HS, then to the DS (right leg in the back), and then back to the right TO (start of the gait).

As shown in Figure 2-2(a), the planar link system of lower limbs [43–45] has been adopted in this study to characterize the movements of four gait phases. The planar link system contains six body segments (left upper leg, right upper leg, left lower leg, right lower leg, left foot, and right foot) and six hinge joints (left hip, right hip, left knee, right knee, left ankle, and right ankle joints). Body segments are represented as homogenous rod links with lengths of L_i and uniformly distributed masses of M_i. The foot dimensions are characterized by the rocker model [46–48] in four parts: forefoot, mid-foot, heel, and ankle, as shown in Figure 2-2(b).

The length of link *i* is denoted as L_i, which could be from direct measurements of individuals. When the direct measurements of the subject are not accessible, the link length can also be estimated based on the link-length ratio that follows:

$$L_i = L_0 l_i \tag{2-1}$$

where l_i is the link-length ratio of link i and L_0 is the measured stature of the subject. Similarly, the mass of link i is denoted as M_i follows:

$$M_i = M_0 m_i \tag{2-2}$$

where m_i is the mass-ratio of link i and M_0 is the measured body mass.

The l_i and m_i are commonly used to estimate the length and mass of each body link [16,49–51]. The l_i (upper leg, lower leg, ankle, forefoot, mid-foot, and heel length ratios) and m_i (upper body, upper leg, lower leg, and foot mass ratios) for male are listed in Table 2-1.

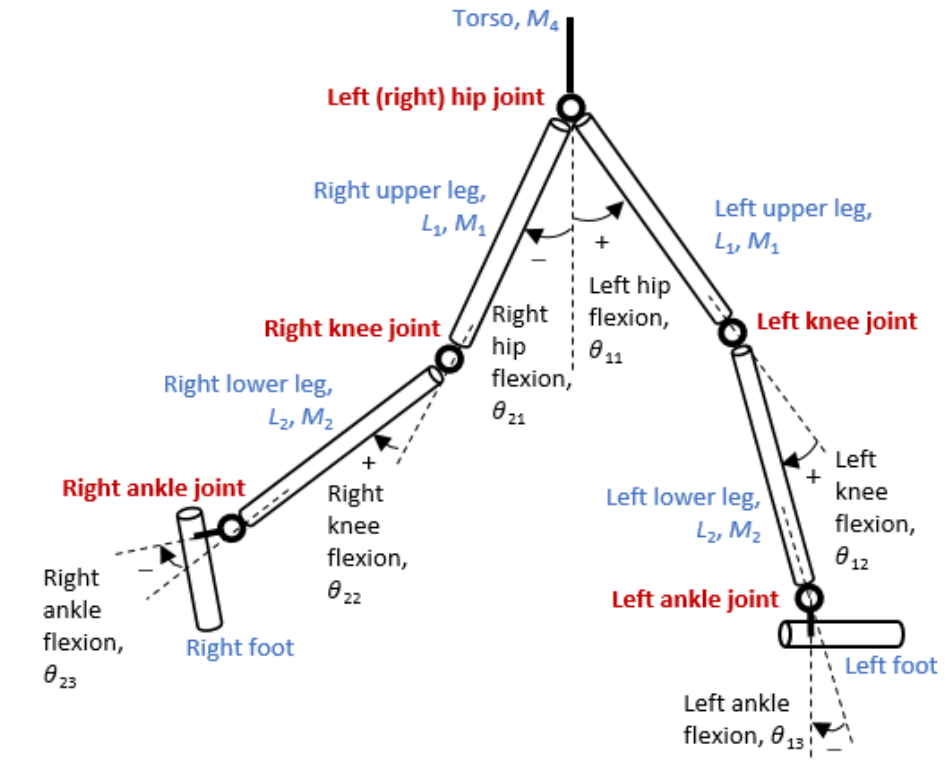

(a)

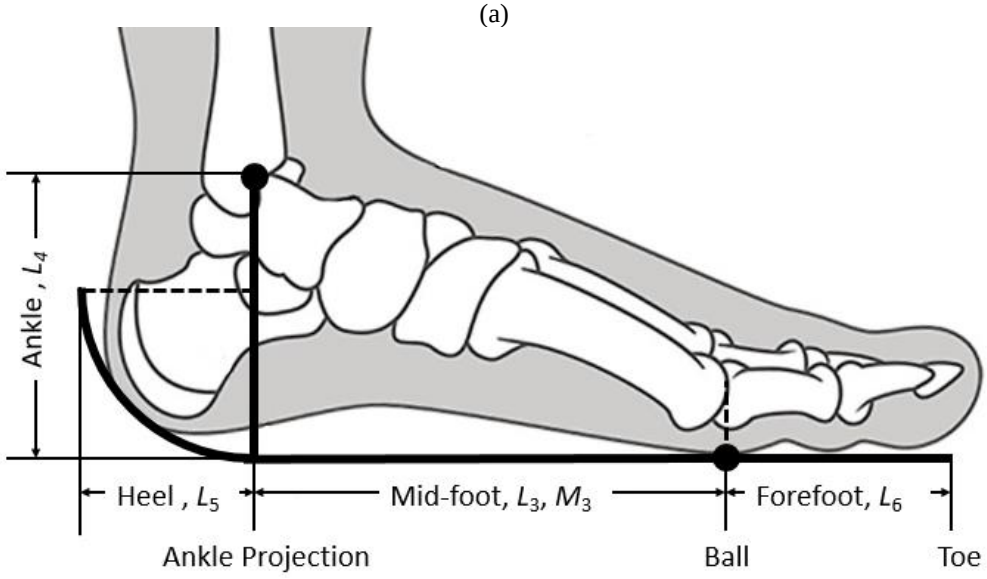

(b)

Figure 2-2: (a) Biomechanical model with definitions of limb links, joints, and joint angles in the sagittal plane and (b) the foot anatomy and dimensions in the sagittal plane (part of the image adopted from [52]).

Table 2-1: The link-length and link-mass ratios used to estimate the link lengths and masses for simulation, and the measured link lengths and estimated link masses for the male subject in Section 2.3.

	Parameters	i	Ratios*, l_i	Subject's values**, L_i (cm)
Anthropometry data	Stature		1	178
	Upper leg length	1	0.257	41
	Lower leg length	2	0.229	40
	Ankle height	3	0.042	7
	Forefoot length	4	0.026	4
	Mid-foot length	5	0.1	13
	Heel length	6	0.03	5
	Parameters		Ratios, m_i	Subject's values***, M_i (kg)
	Body mass		1	68.4
	Upper leg mass	1	0.132	9
	Lower leg mass	2	0.044	3
	Foot mass	3	0.014	1
	Upper body mass	4	0.62	42.4

* The link-length ratios are from ANSUR II [53]. The heel ratio is separately estimated based on data reported by Hansen et al. [48].
** The link lengths are from the direct measurement from the subject in Section 2.3.
*** The body mass value is from direct measurement of the subject in Section 2.3. The link masses are estimated from the link-mass ratios reported by Drillis and Contini [16].

As shown in Figure 2-2(a), the joint angles are denoted as θ_{ij} where *i* represents the side (1 for left and 2 for right) and *j* represents the joint (1 for hip, 2 for knee, and 3 for ankle). All the angles are measured from the standing neutral posture angles. Flexion directions (dorsiflexion for ankle joint) are considered positive, and extension directions (plantar flexion for ankle joint) are considered negative.

2.2.1. Lumped Muscle Parameters

For the planar link system used in this work, it is assumed that the adjacent links are connected by a hinge joint where muscle torques are lumped into one joint torque that linearly changing with the associated joint angle. This linear relationship is characterized by the lumped muscle parameters (stiffness of a rotational spring), k_{ijp}, in Nm/deg, where *i* represents the side (1 for left and 2 for right), *j* represents the joint (1 for hip, 2 for knee, and 3 for ankle), and *p* represents the phase (1 for SS, 2 for DS, and 3 for SW). Especially, the ankle torque during DS is characterized by the lumped muscle parameter, r_{i32}, in Nm/kg, as normalized by body mass. A summary of the lumped muscle parameters used in the planar link system is listed in Table 2-2.

The definitions of the hip, knee, and ankle joint angles are shown in Figure 2-2(a). The biomechanical models of the three phases are described in the following sections.

Table 2-2: Summary of lumped muscle parameters in the model

	Phase	Joint (i = 1 and 2)	Value
Lumped muscle parameters	DS	Hip, k_{i12} (Nm/deg)	20
		Knee, k_{i22} (Nm/deg)	20
		Ankle, r_{i32} (Nm/kg)	1.5
	SW	Hip, k_{i13} (Nm/deg)	20
		Knee, k_{i23} (Nm/deg)	8

*The lumped muscle parameters of the hip and knee joints describe the joint torques by spring stiffness. The lumped muscle parameters of ankle joints describe the joint torques normalizing by body mass.

2.2.2. Single Stance Phase

An inverted pendulum model is used to predict the leg movement during the SS (Figure 2-3(a)). The upper leg and lower leg are rotating about the ankle joint with the knee being straight. By assuming the knee is straight and the foot is flat on the ground during SS, the equation of motion for the inverted pendulum can be adapted from [31] as:

$$\ddot{\theta}_{i1} = \ddot{\theta}_{i3} = \frac{6g(M_1L_1 + M_2L_2 + 2M_1L_2 + 2M_4(L_1 + L_2))}{M_2L_2^2 + M_1(L_1 + 2L_2)^2 + 12M_4(L_1 + L_2)^2}\sin\theta_{i1} - \frac{12k_{AFO}\theta_{i1}}{M_2L_2^2 + M_1(L_1 + 2L_2)^2 + 12M_4(L_1 + L_2)^2} \quad (2\text{-}3)$$

where θ_{i1} is the hip angle, θ_{i3} is the ankle angle, L_1 is the upper leg length, L_2 is the lower leg length, M_1 is the upper leg mass, M_2 is the lower leg length, M_4 is the upper body mass, g is the gravitational acceleration, and k_{AFO} is the stiffness of the AFO. Additionally, it is assumed that θ_{i1} is equal to θ_{i3} (knee straight) during the SS. The first term of Eq. (2-3) is from Srinivasan and Ruina [31]. The second term is added by this work to simulate the effect of AFO stiffness.

2.2.3. Double Stance Phase

As shown in Figures 2-3(b) and (d), the movements of both legs during the DS is characterized as a series of planar kinematic chain movements in the sagittal plane. This kinematic chain model is simplified from the existing kinematic chain model [35] by assuming the front knee is straight during the DS. The kinematic chain is constrained at the toe of the back-foot, which is on the ground, and the front-foot, which is flat on the ground. A series of force and torque balance equations are solved to achieve the equations of motion for the leg movement during the DS. A summary of variables and equations is shown in Table 2-3Table 2-3 for a total of 31 equations and 34 variables. Three equations of motion for $\ddot{\theta}_{i1}(t)$, $\ddot{\theta}_{i2}(t)$, and $\ddot{\theta}_{i3}(t)$ for the back-leg are derived from these equations for finding the implicit solution if the initial conditions of the DS are known. The detailed derivation for the equations of motion during DS is presented in Appendix A.

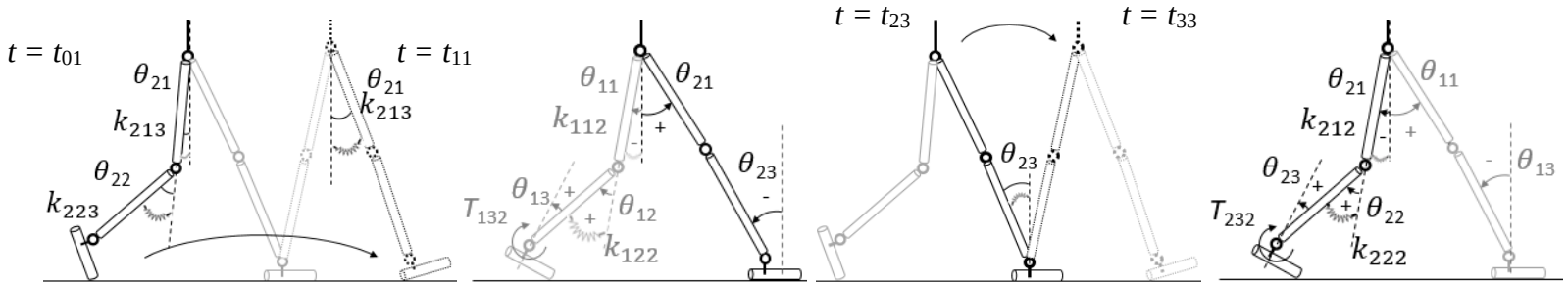

(a) SS ($t = t_{01} \rightarrow t_{11}$) (b) DS ($t = t_{12} \rightarrow t_{22}$) (c) SW ($t = t_{23} \rightarrow t_{33}$) (d) DS ($t = t_{34} \rightarrow t_{44}$)

Time	t_0	$t_{01} \rightarrow t_{11}$	t_1	$t_{12} \rightarrow t_{22}$	t_2	$t_{23} \rightarrow t_{33}$	t_3	$t_{34} \rightarrow t_{44}$	$t_4 = t_0$
Right	TO	SW Eqs. (2-5) and (2-6) Inertial and muscle forces	HS	DS (front-leg) (Appendix A) Inertial forces		SS Eq. (2-3) Inertial forces		DS (back-leg) (Appendix A) Inertial and muscle forces	TO
Left (AFO)		SS Eq. (2-3) Inertial and AFO forces		DS (back-leg) (Appendix A) Inertial, muscle, and AFO forces	TO	SW Eqs. (2-5) and (2-6) Inertial and muscle forces	HS	DS (front-leg) (Appendix A) Inertial forces	
State vector Eq. (2-6)	$\boldsymbol{\theta_s}(t_0)$ $\dot{\boldsymbol{\theta}}_{\boldsymbol{s}}(t_0)$	$\boldsymbol{\theta_s}(t_{01}) \rightarrow \boldsymbol{\theta_s}(t_{11})$ $\dot{\boldsymbol{\theta}}_{\boldsymbol{s}}(t_{01}) \rightarrow \dot{\boldsymbol{\theta}}_{\boldsymbol{s}}(t_{11})$	$\boldsymbol{\theta_s}(t_1)$ $\dot{\boldsymbol{\theta}}_{\boldsymbol{s}}(t_1)$	$\boldsymbol{\theta_s}(t_{12}) \rightarrow \boldsymbol{\theta_s}(t_{22})$ $\dot{\boldsymbol{\theta}}_{\boldsymbol{s}}(t_{12}) \rightarrow \dot{\boldsymbol{\theta}}_{\boldsymbol{s}}(t_{22})$	$\boldsymbol{\theta_s}(t_2)$ $\dot{\boldsymbol{\theta}}_{\boldsymbol{s}}(t_2)$	$\boldsymbol{\theta_s}(t_{23}) \rightarrow \boldsymbol{\theta_s}(t_{33})$ $\dot{\boldsymbol{\theta}}_{\boldsymbol{s}}(t_{23}) \rightarrow \dot{\boldsymbol{\theta}}_{\boldsymbol{s}}(t_{33})$	$\boldsymbol{\theta_s}(t_3)$ $\dot{\boldsymbol{\theta}}_{\boldsymbol{s}}(t_3)$	$\boldsymbol{\theta_s}(t_{34}) \rightarrow \boldsymbol{\theta_s}(t_{44})$ $\dot{\boldsymbol{\theta}}_{\boldsymbol{s}}(t_{34}) \rightarrow \dot{\boldsymbol{\theta}}_{\boldsymbol{s}}(t_{44})$	$\boldsymbol{\theta_s}(t_4)$ $\dot{\boldsymbol{\theta}}_{\boldsymbol{s}}(t_4)$

Figure 2-3: Summary of state vectors transferred between phases and forces and equations related to each phase assuming the AFO is on the left ankle. Top diagrams represent the joint angles and lumped muscle parameters related to the right leg (solid black) movement during each phase: (a) The right leg movement during the SW is simulated by a double-pendulum with two rotational springs on the knee and hip joints, from right TO (t_0) to right HS (t_1), (b) the leg movements during the DS are simulated by a kinematic chain model with the right leg in front, from right HS (t_1) to left TO (t_2), (c) the right leg movement during the SS is simulated by an inverted pendulum, from left TO (t_2) to left HS (t_3), and (d) the leg movements during the DS are simulated by a kinematic chain model with the right leg in the back, from left HS (t_3) to right TO (t_4).

Table 2-3: Summary of variables and equations used in Appendix A to solve the movement during the DS

	Types	Number of variables	Number of equations
Geometry	Angles	5	7
	Angular velocities	5	
Dynamics	External forces	2	24 (Non-linear simultaneous equations)
	Internal forces	6	
	Joint velocities	6	
	Link center of mass velocities	6	
	Link rotation angular velocities	4	

Since the active ankle torque during the DS does not follow the spring property [13], the active ankle torque is estimated based on the body mass. The effect of AFO stiffness on the ankle joint is simulated by changing the ankle stiffness. For the ankle wearing the AFO, it is assumed that the active ankle torque does not change with different AFO stiffnesses. Thus, the total ankle torque, T_{i32}, is determined as:

$$T_{i32}(t) = r_{i32}M_0 + k_{AFO}\theta_{i3}(t) \tag{2-4}$$

where $\theta_{i3}(t) > 0°$ represents the dorsiflexion of the ankle, $\theta_{i3}(t) < 0°$ represents the plantar flexion of the ankle, and r_{i32} is the active ankle torque of the push-off ankle (Table 2-2) normalized by body mass.

2.2.4. Swing Phase

For the SW, the swing leg is characterized as a double-pendulum, with knee and hip muscle torques linearly changing with the associated joint angles, as shown in Figure 2-3(c). Equations of motion for the double-pendulum are solved by the Euler-Lagrange differential equations [54] and given by:

$$12M_1L_1^2\ddot{\theta}_{i1} + 6M_2L_1^2\ddot{\theta}_{i1} + 3M_2L_1L_2\ddot{\theta}_{i2}\cos(\theta_{i1} - \theta_{i2}) + 3M_2L_1L_2\dot{\theta}_{i2}^2\sin(\theta_{i1} - \theta_{i2}) + 3M_1L_1g\sin\theta_{i1} + 6M_2L_1g\sin\theta_{i1} + 6k_{i13} = 0 \quad (2\text{-}5)$$

$$3M_2L_1L_2\ddot{\theta}_{i1}\cos(\theta_{i1} - \theta_{i2}) + 2M_2L_2^2\ddot{\theta}_{i2} - 3M_2L_1L_2\dot{\theta}_{i1}^2\sin(\theta_{i1} - \theta_{i2}) + 3M_2L_2g\sin\theta_{i2} + 6k_{i23} = 0 \quad (2\text{-}6)$$

where θ_{i2} is the knee angle, k_{i13} is the lumped muscle parameter of the hip joint during the SW, and k_{i23} is the lumped muscle parameter of the knee joint during the SW. The ankle angle, θ_{i3}, was assumed neutral (θ_{i3} = 0) during the SW.

2.2.5. Phases Continuity – Forward Dynamics

The angle and angular velocity of each joint (Figure 2-2(a)) at time *t*, $\theta_{ij}(t)$ and $\dot{\theta}_{ij}(t)$, are summarized in an angle state vector and an angular velocity state vector, $\boldsymbol{\theta_S}(t)$ and $\dot{\boldsymbol{\theta}}_{\boldsymbol{S}}(t)$:

$$\boldsymbol{\theta_S}(t) = \begin{Bmatrix} \theta_{11}(t) \\ \theta_{12}(t) \\ \theta_{13}(t) \\ \theta_{21}(t) \\ \theta_{22}(t) \\ \theta_{23}(t) \end{Bmatrix} \quad (2\text{-}7)$$

$$\dot{\boldsymbol{\theta}}_{\boldsymbol{S}}(t) = \begin{Bmatrix} \dot{\theta}_{11}(t) \\ \dot{\theta}_{12}(t) \\ \dot{\theta}_{13}(t) \\ \dot{\theta}_{21}(t) \\ \dot{\theta}_{22}(t) \\ \dot{\theta}_{23}(t) \end{Bmatrix} \quad (2\text{-}8)$$

In between the phases, these state vectors are transferred from the end of one phase to the start of the next phase to pass the values of angle and angular velocity of each joint. The state vectors flow between phases and the equations associated with each phase are summarized in

Figure 2-3. The initial state vectors are defined as the initial conditions of the right SW and left SS, $\boldsymbol{\theta_S}(t_0)$ and $\dot{\boldsymbol{\theta}}_{\boldsymbol{S}}(t_0)$. By solving the forward dynamics based on the equations of motion of right SW and left SS, the end conditions of this phase are calculated and used as the initial conditions of the next phase. This process continues through all four phases and finally ends at the start of the right SW and left SS. The state vectors for the end conditions of the gait are represented as $\boldsymbol{\theta_S}(t_4)$ and $\dot{\boldsymbol{\theta}}_{\boldsymbol{S}}(t_4)$.

The gait event time is denoted as t_i, where i represents the gait event (0 for right TO, 1 for right HS, 2 for left TO, 3 for left HS, and 4 for right TO). Similarly, the start time and end time of each phase are denoted as t_{ij}, where i represents the start or end gait event of the phase, and j represents the phase (1 for right SW, 2 for DS with right leg in front, 3 for right SS, and 4 for DS with right leg in the back). Considering the continuity of the gait, the time denotation follows:

$$t_i = t_{i(i+1)} - \Delta t = t_{ii} + \Delta t \qquad \text{for } i = 0, 1, 2, 3, \text{ and } 4 \quad (2\text{-}9)$$

where Δt is short enough time in between phases. Consequently, the continuity between phases can be expressed with the equations of state vectors as:

$$\boldsymbol{\theta_S}\left(t_{i(i+1)} - \Delta t\right) = \boldsymbol{\theta_S}(t_i) = \boldsymbol{\theta_S}(t_{ii} + \Delta t) \qquad \text{for } i = 0, 1, 2, 3, \text{ and } 4 \quad (2\text{-}10)$$

$$\dot{\boldsymbol{\theta}}_{\boldsymbol{S}}(t_{i(i+1)} - \Delta t) = \boldsymbol{\theta_S}(t_i) = \dot{\boldsymbol{\theta}}_{\boldsymbol{S}}(t_{ii} + \Delta t) \qquad \text{for } i = 0, 1, 2, 3, \text{ and } 4 \quad (2\text{-}11)$$

The errors between the initial conditions and end conditions are defined with two error vectors:

$$\boldsymbol{\varepsilon_{\theta}} = \begin{Bmatrix} \varepsilon_{\theta_{11}} \\ \varepsilon_{\theta_{12}} \\ \varepsilon_{\theta_{13}} \\ \varepsilon_{\theta_{21}} \\ \varepsilon_{\theta_{22}} \\ \varepsilon_{\theta_{23}} \end{Bmatrix} \tag{2-12}$$

$$\boldsymbol{\varepsilon_{\dot{\theta}}} = \begin{Bmatrix} \varepsilon_{\dot{\theta}_{11}} \\ \varepsilon_{\dot{\theta}_{12}} \\ \varepsilon_{\dot{\theta}_{13}} \\ \varepsilon_{\dot{\theta}_{21}} \\ \varepsilon_{\dot{\theta}_{22}} \\ \varepsilon_{\dot{\theta}_{23}} \end{Bmatrix} \tag{2-13}$$

where each element is the absolute value of differences between the elements in the state vector at the initial conditions and the associated end conditions:

$$\varepsilon_{\theta_{ij}} = \left|\theta_{ij}(t_0) - \theta_{ij}(t_4)\right| \quad \begin{matrix} \text{for } i = 1 \text{ and } 2 \\ \text{for } j = 1, 2, \text{ and } 3 \end{matrix} \tag{2-14}$$

$$\varepsilon_{\dot{\theta}_{ij}} = \left|\dot{\theta}_{ij}(t_0) - \dot{\theta}_{ij}(t_4)\right| \quad \begin{matrix} \text{for } i = 1 \text{ and } 2 \\ \text{for } j = 1, 2, \text{ and } 3 \end{matrix} \tag{2-15}$$

2.2.6. Initial Conditions at the Right TO

To simplify the state vectors for the initial conditions, several assumptions are made to reduce the dimension of the state vectors. Since front-foot and back-toe are assumed to be on the ground (Figure 2-3(d)) during the DS and at the right TO (start of the gait), the vertical distances between them and the hip joints satisfy:

$$\begin{aligned} (L_1 + L_2)\cos\theta_{11} + L_4 \\ = L_4\cos(\theta_{22} - \theta_{21} - \theta_{23}) \\ + L_3\sin(\theta_{22} - \theta_{21} - \theta_{23}) + L_2\cos(\theta_{22} - \theta_{21}) \\ - L_1\cos\theta_{21} \end{aligned} \tag{2-16}$$

Thus, the back-ankle angle and angular velocity, θ_{23} and $\dot{\theta}_{23}$, can be derived from other joint angles (θ_{11}, θ_{21}, and θ_{22}) and angular velocities ($\dot{\theta}_{11}$, $\dot{\theta}_{21}$, and $\dot{\theta}_{22}$) and link lengths (L_1, L_2, L_3, and L_4). Also, the front-leg is assumed straight, and the front-foot is assumed flat on the ground during the DS and at the right TO (start of the gait):

$$\theta_{12}(t_0) = \dot{\theta}_{12}(t_0) = 0 \tag{2-17}$$

$$\theta_{13}(t_0) = -\theta_{11}(t_0) \tag{2-18}$$

$$\dot{\theta}_{13}(t_0) = -\dot{\theta}_{11}(t_0) \tag{2-19}$$

Thus, the state vectors for the initial conditions can be simplified as:

$$\boldsymbol{\theta_S}(t_0) = \begin{Bmatrix} \theta_{11}(t_0) \\ 0 \\ -\theta_{11}(t_0) \\ \theta_{21}(t_0) \\ \theta_{22}(t_0) \\ \theta_{23}(t_0) \end{Bmatrix} \tag{2-20}$$

$$\dot{\boldsymbol{\theta}}_{\boldsymbol{S}}(t_0) = \begin{Bmatrix} \dot{\theta}_{11}(t_0) \\ 0 \\ -\dot{\theta}_{11}(t_0) \\ \dot{\theta}_{21}(t_0) \\ \dot{\theta}_{22}(t_0) \\ \dot{\theta}_{23}(t_0) \end{Bmatrix} \tag{2-21}$$

where the angle state vector has 3 dimensions, $\theta_{11}(t_0)$, $\theta_{21}(t_0)$, and $\theta_{22}(t_0)$, and the angular velocity state vector has 3 dimensions, $\dot{\theta}_{11}(t_0)$, $\dot{\theta}_{21}(t_0)$, and $\dot{\theta}_{22}(t_0)$. $\theta_{23}(t_0)$ and $\dot{\theta}_{23}(t_0)$ can be derived from other angles and angular velocities based on Eq. (2-16).

2.2.7. Sensitivity Analysis

A sensitivity analysis was performed to investigate the effect of different initial conditions on error vectors and gait parameters. The inputs (independent variables) were $\boldsymbol{\theta_S}(t_0)$,

which includes the initial left hip angle, $\theta_{11}(t_0)$, the initial right hip angle, $\theta_{21}(t_0)$, and the initial right knee angle, $\theta_{22}(t_0)$, and $\dot{\boldsymbol{\theta}}_{\boldsymbol{S}}(t_0)$, which includes the initial left hip angular velocity, $\dot{\theta}_{11}(t_0)$, the initial right hip angular velocity, $\dot{\theta}_{21}(t_0)$, and the initial right knee angular velocity, $\dot{\theta}_{22}(t_0)$. The outputs (dependent variables) were $\boldsymbol{\varepsilon_{\theta}}$, $\boldsymbol{\varepsilon_{\dot{\theta}}}$, step length, swing time, and stance time. The subject variables were the stature and body mass.

To determine the normal range of the inputs, 11 references on joint angles (hip, knee, and ankle angles) and angular velocities (hip and knee angular velocities) in the sagittal plane for the normal gait at TO were studied. As the range summarized in Table 2-4, the hip flexion angles of the front- and back-leg at TO were ranged from 5 to 30° and –30 to –5°, respectively [13,55–60]. The knee flexions of the front- and the back-leg were ranged from 0 to 20° and 20 to 45°, respectively [13,55–64]. Part of these investigators also reported that the hip flexion angular velocities for front- and back-leg at TO were ranged from –200 to –100° per second and 100 to 150° per second, respectively [59,60]. Tong and Granat [60] reported the observed knee flexion angular velocities for front- and back-leg were 20° per second and ranged from 100 to 270° per second, respectively. Some investigators reported that ankle flexion angles for front- and back-leg were ranged from –5 to 10° and –45 to 0°, respectively [13,55–57,59,61,62,64]. These studies gave a reference on the normal range of joint angles and angular velocities as inputs for the model.

Table 2-4: Summary of observed joint angles for hip, knee, and ankle, joint angular velocities for hip and knee at right TO, and the step length (S_L) to stature (L_0) ratio during the walking gait.

Paper	*n*	Front-leg					Back-leg					S_L/L_0
		Hip		Knee		Ankle	Hip		Knee		Ankle	
		θ_{11} (deg)	$\dot{\theta}_{11}$ (deg/s)	θ_{12} (deg)	$\dot{\theta}_{12}$ (deg/s)	θ_{13} (deg)	θ_{21} (deg)	$\dot{\theta}_{21}$ (deg/s)	θ_{22} (deg)	$\dot{\theta}_{22}$ (deg/s)	θ_{23} (deg)	
Begg et al., 2006 [62]	24			5		–5			30 ~ 45		–30 ~ 0	0.41 ~ 0.45*
Buczek et al., 2010 [55]	25	25 ~ 30		0 ~ 10		–5 ~ 5	–15 ~ –5		25 ~ 30		–46 ~ –25	
Collins et al., 2009 [56]	10	25		10		5	–10		20		–5	
Eltoukhy et al., 2017 [57]	10	15		10		0			25		–5	0.44*
Kiss et al., 2004 [63]	51			10					45			0.27 ~ 0.29**
Mills et al., 2007 [64]	10			5		10			45		–25	
Ramakrishnan et al., 1991 [58]	1	30		0			–5		30			
Seel et al., 2014 [61]	1			4		–5			30		–30	
Tadano et al., 2013 [59]	5	20 ~ 30	–200 ~ –100	10 ~ 15		–5 ~ 5	–10 ~ –5	100 ~ 120	30 ~ 50		–20 ~ –10	0.22 ~ 0.36***
Tong et al., 1999 [60]	2	5 ~ 15	–130 ~ –100	15	20		–30 ~ –25	100 ~ 150	20 ~ 30	100 ~ 270		
Winter, 1984 [13]	16	10		20		–5	–15		35		–15	
Range	212	5 ~ 30	–200 ~ –100	0 ~ 20	20	–5 ~ 10	–30 ~ –5	100 ~ 150	20 ~ 45	100 ~ 270	–45 ~ 0	0.22 ~ 0.45

* S_L/L_0 for self-selected comfort walking speed.
** S_L/L_0 for preset walking speed on a treadmill (0.83 m/s).
*** S_L/L_0 for self-selected comfort walking speed estimated by a lower-limbs-mounted IMU system.

To validate the model-predicted step length, the step length-to-stature ratio reported in the references are also summarized in the last column of Table 2-4, with a range from 0.22 to 0.45 [57,59,62,63]. This range will be compared with the model-predicted step length-to-stature ratio in this work.

The sensitivity analysis was performed for a 50th percentile healthy male (176.3 cm and 86.4 kg) walking with no AFO to preliminary examine the effect of initial conditions on global errors. The link length and mass were estimated based on the ratios reported in Table 2-1. The lumped muscle parameters were estimated based on joint torques during gait reported by Winter [13], as shown in Table 2-2. The range of the initial conditions was determined based on the range summarized in Table 2-4. The sensitivity analysis examined all possible combinations of initial conditions within the range and calculated the error vectors for each combination. The first set of combinations examined was with $\theta_{11}(t_0)$ from 5 to 30° with steps of 5°, while $\theta_{21}(t_0)$ = –5°, $\theta_{22}(t_0)$ = 20°, $\dot{\theta}_{11}(t_0)$ = –50° per second, $\dot{\theta}_{21}(t_0)$ = 100° per second, and $\dot{\theta}_{22}(t_0)$ = 100° per second. Then $\theta_{21}(t_0)$ was decreased by 5°, and the same process was performed for $\theta_{11}(t_0)$ from 5 to 30° with steps of 5°. This whole process was performed until all combinations of $\theta_{11}(t_0)$, $\theta_{21}(t_0)$, $\theta_{22}(t_0)$, $\dot{\theta}_{11}(t_0)$, $\dot{\theta}_{21}(t_0)$, and $\dot{\theta}_{22}(t_0)$ had been examined. A summary of the start, stop, and step values for each initial angle and angular velocity is shown in Table 2-5. A complete list and explanations of combinations examined can be found in Appendix B.

Table 2-5: Range of initial conditions for the sensitivity analysis and simulation

State vector	Elements	Unit	Range (start, stop, step)	
			Sensitivity analysis (Section 2.2.7)	Simulation (Section 2.3)
$\boldsymbol{\theta_s}(t)$	$\theta_{11}(t)$	deg	(5, 30, 5)	(5, 30, 1)
	$\theta_{21}(t)$		(–5, –30, –5)	(–5, –30, –1)
	$\theta_{22}(t)$		(20, 45, 5)	(20, 45, 1)
$\dot{\boldsymbol{\theta}}_{\boldsymbol{s}}(t)$	$\dot{\theta}_{11}(t)$	deg/s	(–100, –200, –50)	(–100, –200, –50)
	$\dot{\theta}_{21}(t)$		(100, 150, 50)	(100, 150, 50)
	$\dot{\theta}_{22}(t)$		(100, 300, 50)	(100, 300, 50)

There were in total 6,480 combinations of the initial conditions examined during the sensitivity analysis via simulation. Part of the combinations had invalid geometry at the initial conditions or resulted in incomplete phases. Only 918 of the combinations resulted in complete gaits and were considered valid. For these valid combinations, a series of regressions were performed with the initial conditions as the predictor, and the error vectors and gait parameters as responses to examine the contributions of variations in each input.

Contributions of variations in each dimension of the initial state vectors to variations in each element of the error vectors and gait parameters are listed in

Table 2-6. Only the front-hip (left) and back-hip (right) initial angle explained more than 1% of the variations in error vectors. The back-knee initial angle explained more than 0.5% of the variations in error vectors. None of the initial angular velocities explained more than 0.1% of the variations in error vectors. This implied that reducing the magnitude of the error vectors should mainly focus on changing initial angles in smaller steps. This also implied that the velocity vector did not contribute much to the error vectors. For this reason, the angular velocity error vector should be weighted less than the angle error vector.

Table 2-6: The statistics of sensitivity analysis output (error vectors and gait parameters) and the percent contributions of variations in initial state vectors to variations in error vectors and gait parameters for all 918 valid combinations of initial state vectors.

		$\boldsymbol{\varepsilon_{\theta_S}}$ (deg)						$\boldsymbol{\varepsilon_{\dot{\theta}_S}}$ (deg/s)						S_L (m)	T_{SW} (s)	T_{ST} (s)
		ε_{11}	ε_{12}	ε_{13}	ε_{21}	ε_{22}	ε_{23}	$\dot{\varepsilon}_{11}$	$\dot{\varepsilon}_{12}$	$\dot{\varepsilon}_{13}$	$\dot{\varepsilon}_{21}$	$\dot{\varepsilon}_{22}$	$\dot{\varepsilon}_{23}$			
Statistics	Mean	0.62	-	0.62	0.75	0.46	0.49	11	-	11	37	35	9.5	0.70	0.31	0.42
	SD	0.41	-	0.41	0.60	0.40	0.58	18	-	18	62	62	19	0.13	0.17	0.27
	Min	0.06	-	0.06	0	0	0	0	-	0	0.3	0.2	0	0.35	0.10	0.21
	Max	2.2	-	2.2	6.2	5.6	2.8	245	-	245	135	970	289	0.76	0.56	1.1
Contribution (%)	$\theta_{11}(t_0)$	0.3	-	0.3	2.6	3.8	0.1	0.5	-	0.5	7.7	3.5	0.1	67	1.3	1.3
	$\theta_{21}(t_0)$	7.0	-	7.0	14	11	4.0	1.8	-	1.8	5.0	2.2	0.4	21	0	0
	$\theta_{22}(t_0)$	0	-	0	0.1	0.5	0	0	-	0	0.5	0.6	0	12	0.3	0.3
	$\dot{\theta}_{11}(t_0)$	0	-	0	0	0.1	0.1	0	-	0	0.1	0	0.1	0	12	12
	$\dot{\theta}_{21}(t_0)$	0	-	0	0	0	0	0	-	0	0	0	0	0	5.3	5.2
	$\dot{\theta}_{22}(t_0)$	0	-	0	0	0	0	0	-	0	0	0	0	0	6.0	5.8

* S_L is step length, T_{SW} is swing time, and T_{ST} is stance time (SS+DS).

The step lengths were mainly determined by the initial angle state vector. The predicted step length-to-stature ratio was within 0.20 to 0.43, which was close to the range, 0.22 to 0.45, reported in Table 2-4. The step length was determined by the initial geometry of the gait because the step length is a spatial parameter. Similarly, the swing and stance time were mainly determined by the initial angular velocity state vector.

To quantitatively compare the overall error from different initial conditions, a global error vector, $\boldsymbol{E}$, is proposed in this work with its s^{th} element as:

$$\boldsymbol{E}(s) = ||\boldsymbol{\varepsilon}_{\boldsymbol{\theta}}^{\boldsymbol{s}}|| + f||\boldsymbol{\varepsilon}_{\dot{\boldsymbol{\theta}}}^{\boldsymbol{s}}|| \tag{22}$$

where s is the order of the initial conditions being examined, $||\boldsymbol{\varepsilon}_{\boldsymbol{\theta}}^{\boldsymbol{s}}||$ is the norm of the angle error vector for the s^{th} initial conditions, $||\boldsymbol{\varepsilon}_{\dot{\boldsymbol{\theta}}}^{\boldsymbol{s}}||$ is the norm of the angular velocity error vector for the s^{th} initial conditions, and f is a scalar factor that is used to adjust the weighing between errors in angles and angular velocities.

As shown in Figure 2-3, it was assumed that the end conditions of a gait should be equal to the initial conditions of that gait to maintain the consistency and continuity between phases. Thus, the initial conditions with the minimum global error were considered as the optimal initial conditions for gait prediction.

2.2.8. Summary of the Planar Piecewise Continuous Lumped Muscle Parameter (PPCLMP) Model

The proposed model is based on an inverted pendulum model, a kinematic chain model, and a double pendulum model that correspond to SS, DS, and SW, respectively. The joint angles and angular velocities at the end of each phase are used to determine the initial conditions of the next phase. In other words, elements in Eqs. (2-12) and (2-13) should be all equal to zero. For gait with AFOs, the model changes the ankle stiffness to simulate the effect of AFO stiffnesses.

The flowchart of the model is shown in Figure 2-4. Along with the initial conditions, the additional inputs of the model are anthropometry data, lumped muscle parameters, and AFO stiffness. The model examines all possible combinations of initial conditions and stores the global error of each combination in the global vector. After all combinations are examined, the initial conditions with the minimum global error are found and used to predict the gait parameters.

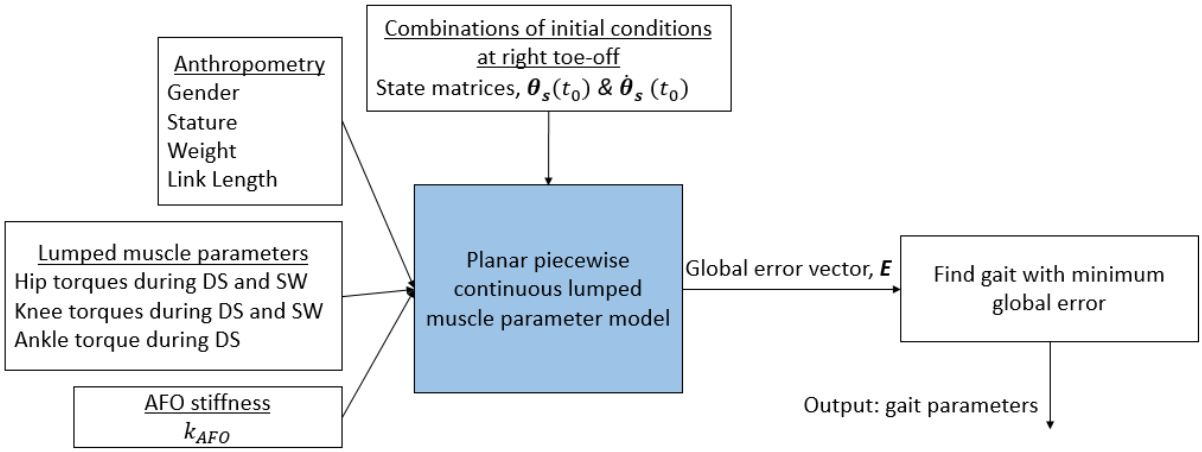

Figure 2-4: Flowchart of the proposed PPCLMP model for predicting gait parameters.

2.3. Experiment Setup

A pilot study was designed to demonstrate the use of the proposed model to predict the effect of three different ankle stiffnesses in a healthy (no known conditions that affect gait) male subject (29-year-old) with 70th percentile stature (178 cm). Then the model prediction of gait parameters was validated with six additional college-age subjects. For the first condition, the subjects wore their regular shoes and socks. For the second and third conditions, they wore two AFOs, respectively, that increased ankle stiffnesses. Before participation, the goal, experimental procedure, and possible risks were explained to the subjects. An informed consent form approved by Institutional Review Boards of the University of Michigan (HUM00090458) was signed by each subject. The anthropometric inputs for the first subject are shown in Table 2-1. The link lengths and body mass were from direct measurement, and the link masses were estimated based on mass ratios reported by Drillis and Contini [16]. The lumped muscle parameters were estimated based on joint torques during gait reported by Winter [13], as shown in Table 2-2. To achieve better prediction outcome from simulating subjects' gaits, the steps for

initial angle state matrix elements was reduced to 1°, as shown in Table 2-5. The steps for angular velocities remained the same, as they did not significantly contribute to the error vectors.

The vision-based measurement system with two sensor units (three cameras each) by NDI Optotrak Certus (NDI Waterloo, Ontario, Canada) was used to capture the locations and movements of lower limbs at 100 Hz. As shown in Figure 2-5, three marker clusters were placed on each upper leg, lower leg, and foot. The marker cluster was used to track the rotation of the associated body segment. Additional markers were placed on the hip, knee, and ankle joints for calibration purposes. Based on the reported common AFO stiffness range of 0.02 to 8.17 Nm/deg from the review by Totah et al. [65], two passive-dynamic AFOs with stiffnesses of 3.4 Nm/deg (denoted as AFO1 hereafter) and 6.9 Nm/deg (denoted as AFO2) were used for this study. Each subject was asked to perform the level ground walking without the AFO (denoted as NAFO), with AFO1, and with AFO2 on his left foot. To gain enough strides ($\geqslant 10$), each subject was asked to walk with self-selected comfort speed for 10 trips within the motion capture area. One trip was defined as walking from one side of the walking area to the other side with at least two complete strides (exclude the first and last strides) for each trip. For each of the AFO condition, each subject was asked to walk with the AFO for 5 minutes before the experiment trial to get used to the stiffness at his ankle.

Figure 2-5: Marker settings for the controlled experiment.

The motion tracking data were imported into MATLAB (MathWorks, Natick, MA, USA) to calculate the joint angles, initial conditions, and gait parameters of each gait cycle to compare with the model prediction. Meanwhile, the joint angles, initial conditions, and gait parameters were also predicted by the model based on the anthropometry data (Table 2-1), lumped muscle parameters (Table 2-2), and AFO stiffness (Table 2-7**Error! Reference source not found.**). The global error was calculated with $\boldsymbol{\varepsilon_{\theta}}$ in degree, and $\boldsymbol{\varepsilon_{\dot{\theta}}}$ in degree per second. Since the magnitude of joint angular velocities in degree per second is on average about 10 times the magnitude of joint angles in degree (Table 2-4) and the angular velocities contributed less to the error vectors, the scalar factor f was assigned as 0.1 seconds. The correlation between the observed and predicted joint angles were calculated using Minitab 18 (Minitab LLC, Chicago, IL, USA).

2.4. Results

In total, 10 complete gait cycles were measured and analyzed for each condition for the first subject. 40 complete gait cycles were measured and analyzed for each condition for each of the six additional subjects. Overall, the model successfully predicted the changing trend of the

gait parameters, except the hip range of motion (ROM) with the AFO2. Moreover, the model is limited in quantitatively predicting the gait parameters.

2.4.1. Pilot Study

The results of initial conditions, error vectors, joint kinematics, step lengths, swing time, and stance time for the subject in the pilot study are summarized in this section to demonstrate the use of the model for investigation of joint stiffness effect on gait.

2.4.1.1 Initial Conditions and Error Vectors

The observed initial conditions, predicted initial conditions, and error vectors of the prediction are shown in Table 2-7. The minimum global errors were less than 3° for all the conditions. The angle errors were all less than 0.5°. The angular velocity errors were all less than or equal to 12° per second, whose magnitude was about 23 times greater than the magnitude of angle errors.

2.4.1.2 Joint Kinematics

Observed and predicted joint angles for left and right legs for each gait cycle are presented in Figures 2-6, 2-7, and 2-8, starting from right TO to right TO. As shown in Table 2-8, the predicted hip flexion angles were strongly correlated with the observed hip flexion angles, with the correlation coefficient (CC) range from 0.85 to 0.98, and the root mean square error (RMSE) range from 5.2 to 11°. The predicted knee flexion angle was strongly correlated with the observed knee flexion angle, with the CC range from 0.87 to 0.99, and the RMSE range from 5.7 to 11°. The predicted ankle flexion angles were strongly correlated with the observed ankle flexion angles, with the CC range from 0.83 to 0.92, and the RMSE range from 4 to 7.2°.

Table 2-7: Summary of AFO stiffness, error vectors, and comparisons between observed (O) and predicted (P) initial conditions for simulations (hip flexion/extension with +/–; knee flexion with +). The errors were estimated with the scalar factor, *f*, equal to 0.1 seconds

	Parameters (i = 1, 2)	NAFO		AFO1		AFO2	
AFO	Structural stiffness, k_{AFO} (Nm/deg)	-		3.4		6.9	
		O	P	O	P	O	P
Initial conditions at right TO	Left hip angle, θ_{11} (deg)	1.7±4.7	19	6.7±3.1	11	7.1±4.5	11
	Left knee angle, θ_{12} (deg)	0.9±1.6	0	8.8±3.3	0	11±2.6	0
	Right hip angle, θ_{21} (deg)	–18±2.7	–19	–5.0±5.1	–11	–8.5±2.1	–9
	Right knee angle, θ_{22} (deg)	26±6.2	32	29±5.2	34	19±2.7	35
	Left hip angular velocity, θ_{11} (deg/s)	–182±167	–150	–81±18	–100	–107±15	–100
	Left knee angular velocity, θ_{12} (deg/s)	68±144	0	75±40	0	77±35	0
	Right hip angular velocity, θ_{21} (deg/s)	94±33	150	88±29	150	166±47	150
	Right knee angular velocity, θ_{22} (deg/s)	205±33	200	239±31	250	265±44	250
Error Vectors	Minimum global error, $min(\boldsymbol{E})$ (deg)		1.2		2.6		2.6
	Left hip angle error, ε_{11} (deg)		0.20		0.37		0.43
	Left knee angle error, ε_{12} (deg)		0		0		0
	Left ankle angle error, ε_{13} (deg)		0.20		0.37		0.43
	Right hip angle error, ε_{21} (deg)		0.12		0.37		0.17
	Right knee angle error, ε_{22} (deg)		0.17		0.35		0.35
	Right ankle angle error, ε_{23} (deg)		0.13		0.20		0.27
	Left hip angular velocity error, $\dot{\varepsilon}_{11}$ (deg/s)		5.9		12		12
	Left knee angular velocity error, $\dot{\varepsilon}_{12}$ (deg/s)		0		0		0
	Left ankle angular velocity error, $\dot{\varepsilon}_{13}$ (deg/s)		5.9		12		12
	Right hip angular velocity error, $\dot{\varepsilon}_{21}$ (deg/s)		2.9		6.0		6.2
	Right knee angular velocity error, $\dot{\varepsilon}_{22}$ (deg/s)		0.12		0.43		0.25
	Right ankle angular velocity error, $\dot{\varepsilon}_{23}$ (deg/s)		0.75		4.4		2.0

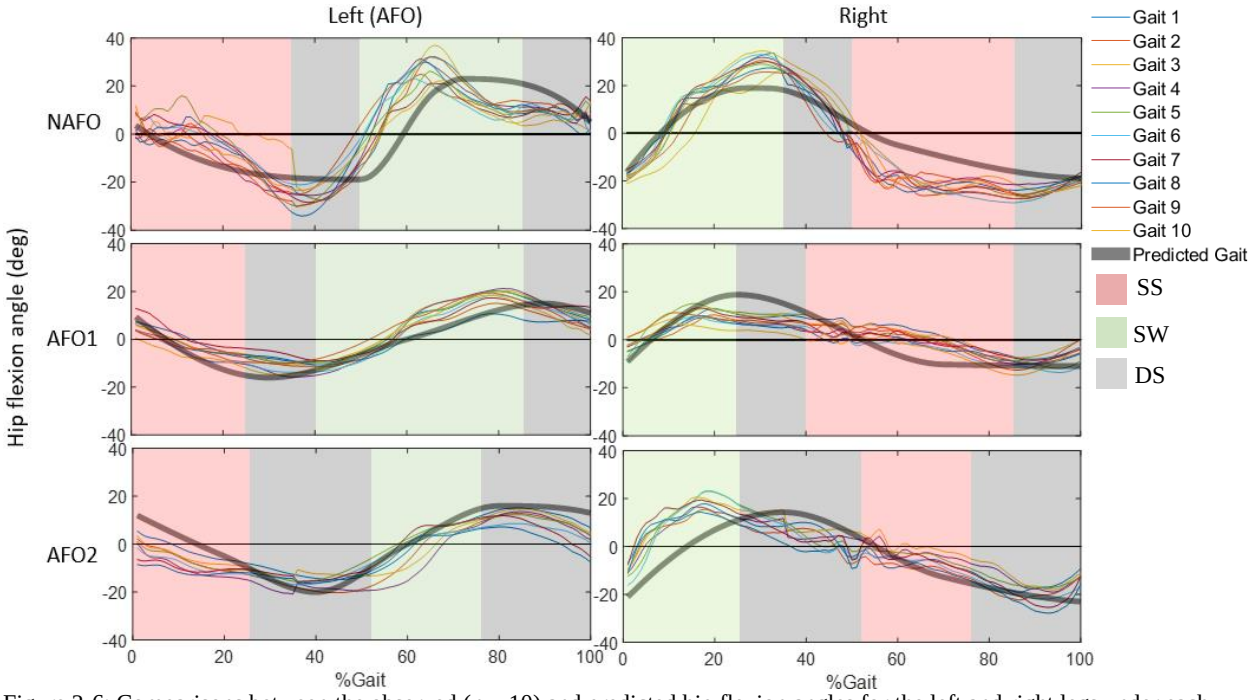

Figure 2-6: Comparisons between the observed (n = 10) and predicted hip flexion angles for the left and right legs under each condition. The presented phase blocks are colored based on the model-predicted time of SS, SW, and DS.

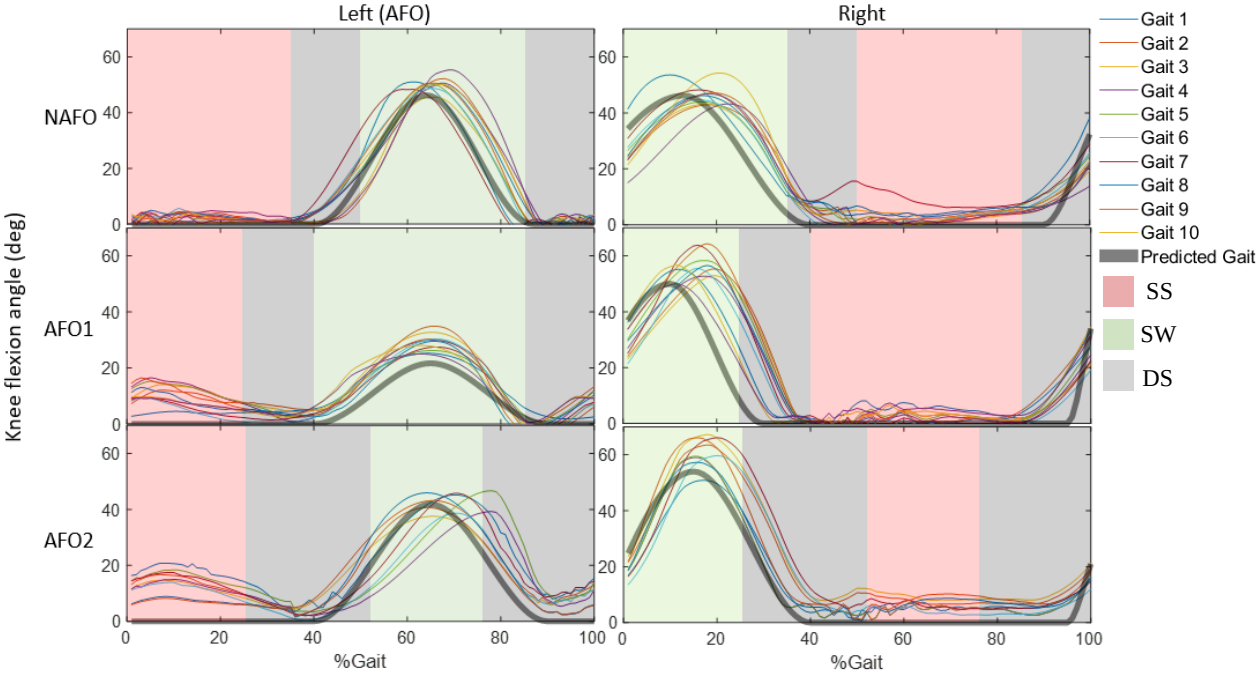

Figure 2-7: Comparisons between the observed (n = 10) and predicted knee flexion angles for the left and right sides under each condition. The presented phase blocks are colored based on the model-predicted time of SS, SW, and DS.

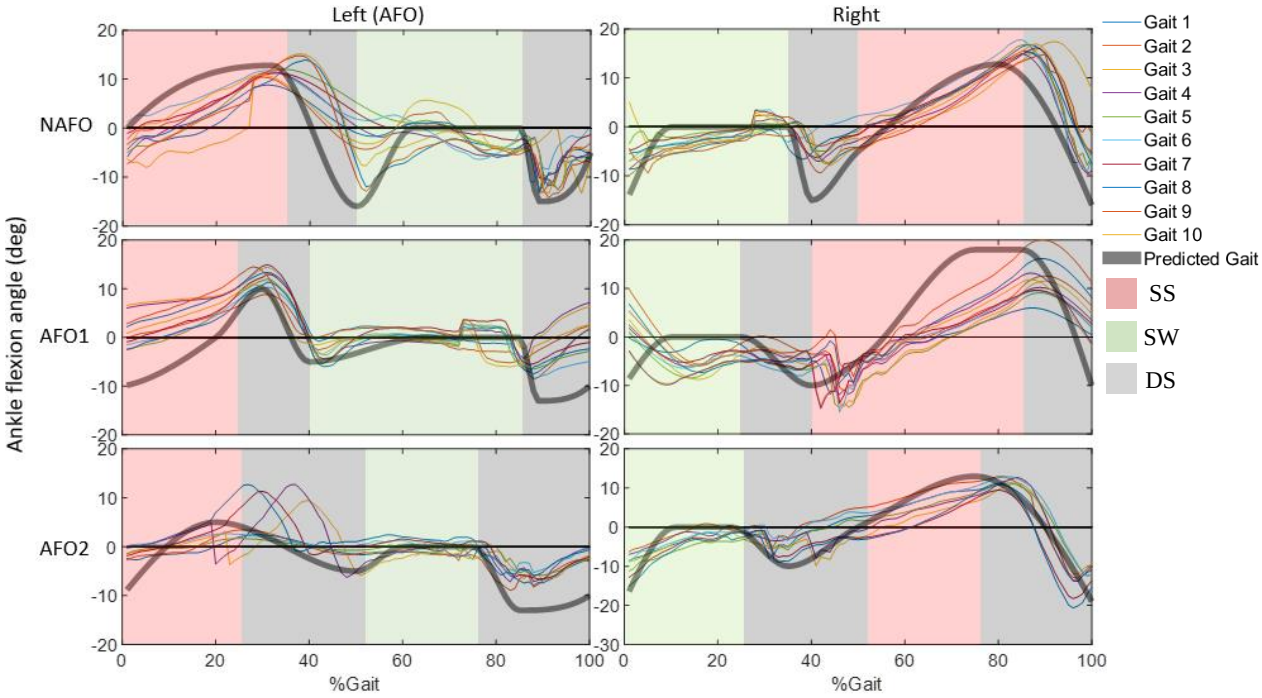

Figure 2-8: Comparisons between the observed (n = 10) and predicted ankle flexion angles for the left and right sides under each condition. The presented phase blocks are colored based on the model-predicted time of SS, SW, and DS.

Table 2-8: Correlation coefficient (CC) and root mean square error (RMSE) between observed and predicted ankle, knee, and hip flexion angles for 10 complete gait cycles

Joint	Side	NAFO		AFO1		AFO2	
		CC	RMSE (deg)	CC	RMSE (deg)	CC	RMSE (deg)
Hip	L (AFO)	0.85	11	0.95	6.0	0.98	5.2
	R	0.97	9.2	0.92	7.1	0.87	9.5
Knee	L (AFO)	0.99	5.7	0.98	7.1	0.99	9.3
	R	0.99	7.7	0.87	11	0.99	7.4
Ankle	L(AFO)	0.83	6.9	0.84	6.8	0.90	4.5
	R	0.87	5.2	0.88	7.2	0.92	4.0

The statistics for ROM of the knee and hip are shown in Table 2-9. Comparing with the NAFO condition, the observed left knee ROM was decreased with the AFO1 and AFO2. The observed right knee ROM was increased with the AFO1 and was further increased with the AFO2. The predicted left and right knee ROMs were changing in the same trend as the observed knee ROM for all conditions. Comparing with the NAFO condition, the observed left hip ROM was decreased with both the AFO1 and the AFO2. The observed right hip ROM was decreased with the AFO1 but slightly decreased with the AFO2. Comparing with the NAFO condition, both

predicted left and right hip ROMs were decreased with the AFO1 but were not decreased with the AFO2.

Table 2-9: Comparison between the observed (O) and predicted (P) range of motion (ROM) for knee and hip angles

Unit: deg			NAFO		AFO1		AFO2	
		Side	O (n = 10)	P	O (n = 10)	P	O (n = 10)	P
Hip	Peak flexion	L (AFO)	28.9±5.8	19.0	19.6±1.1	15.4	14.5±2.6	16.0
		R	30.0±3.0	19.0	13.6±1.6	18.8	20.2±1.9	14.4
	Peak extension	L (AFO)	28.5±5.5	18.9	9.4±1.3	16.0	15.0±0.6	20
		R	26.1±2.0	18.9	9.0±2.8	11.0	18.6±4.4	23.0
Knee	Peak flexion	L (AFO)	50.3±2.4	46.2	29.8±1.0	21.7	41.4±3.1	41.9
		R	46.7±4.0	46.2	54.2±3.2	50.0	60.0±2.3	53.8
Ankle	Peak dorsiflexion	L (AFO)	11.8±2.0	12.8	11±2.2	10	8.5±4.3	5
		R	16.0±1.2	12.8	13±1.3	18	11±0.83	13
	Peak plantar flexion	L (AFO)	12.8±1.1	16.0	5.9±1.6	13	5.2±1.1	13
		R	8.5±1.3	16.0	12±2.4	10	14±2.5	20

2.4.1.3 Step Length

The average observed step lengths of left and right legs for 10 gait cycles, and predicted step lengths are shown in Figure 2-9. Comparing with the NAFO condition, the observed left step lengths were slightly decreased with the AFO1 but were increased with the AFO2. The observed right step lengths were decreased with both the AFO1 and the AFO2. The predicted left and right step lengths were changing in the same trend as the observed step lengths for all conditions.

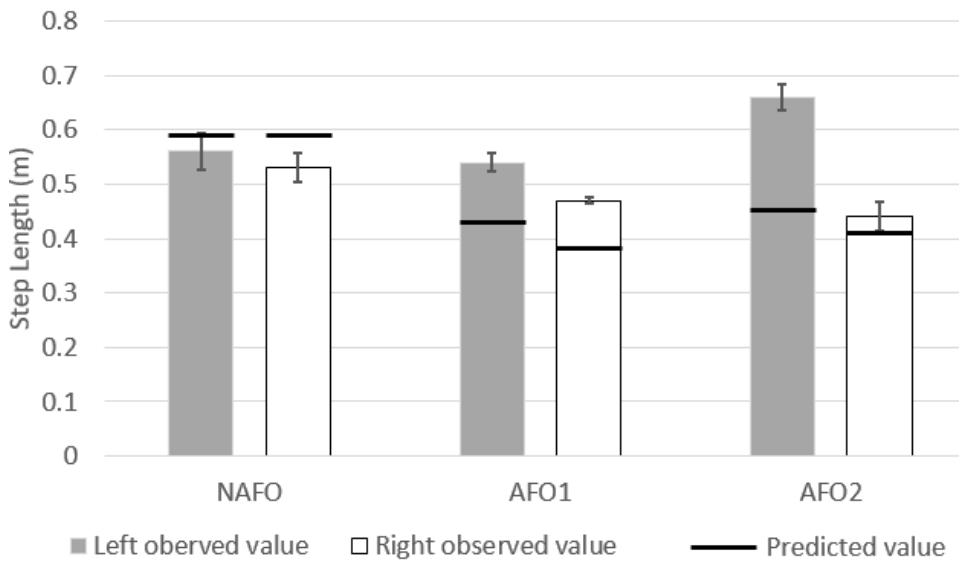

Figure 2-9: Comparisons between the observed and predicted step length for left (AFO) and right sides under each condition (n = 10). Values are mean ± SE.

2.4.1.4 Swing and Stance Time

The average observed swing time of the left and right legs for 10 gait cycles, and predicted swing time are shown in Figure 2-10**Error! Reference source not found.**. Comparing with the NAFO condition, the observed left swing time was increased with the AFO1 but was decreased with the AFO2. The observed right swing time was decreased with both the AFO1 and the AFO2. The predicted left and right swing time was changing in the same trend as the observed swing time for all conditions.

The average observed stance time of the left and right legs for 10 gait cycles, and predicted stance time is shown in Figure 2-11. Comparing with the NAFO condition, the observed left stance time was decreased with both the AFO1 and the AFO2. The observed right stance time was increased with the AFO1 but decreased with the AFO2. The predicted left and right stance time had a similar trend as the observed stance time for all conditions.

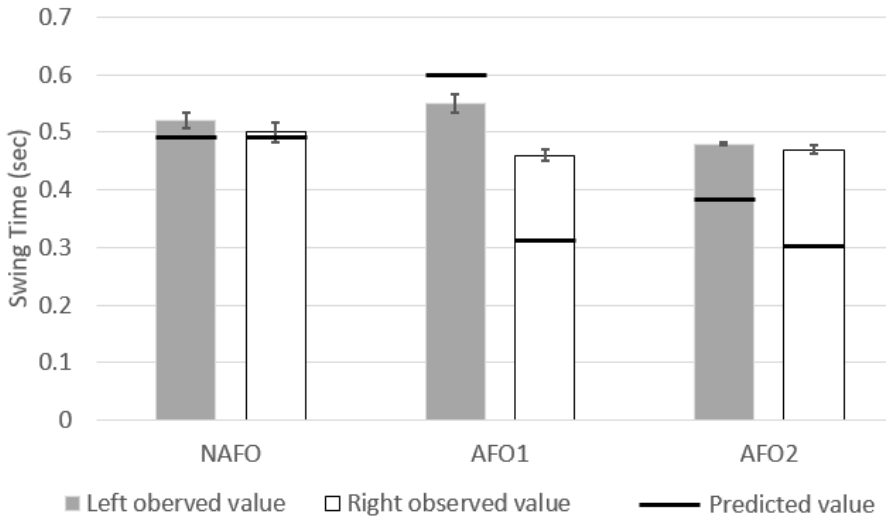

Figure 2-10: Comparisons between the observed and predicted swing time for left (AFO) and right sides under each condition (*n* = 10). Values are mean ± SE.

The average observed stance time of the left and right legs for 10 gait cycles, and predicted stance time is shown in Figure 2-11. Comparing with the NAFO condition, the observed left stance time was decreased with both the AFO1 and the AFO2. The observed right stance time was increased with the AFO1 but decreased with the AFO2. The predicted left and right stance time was changing in the same trend as the observed stance time for all conditions.

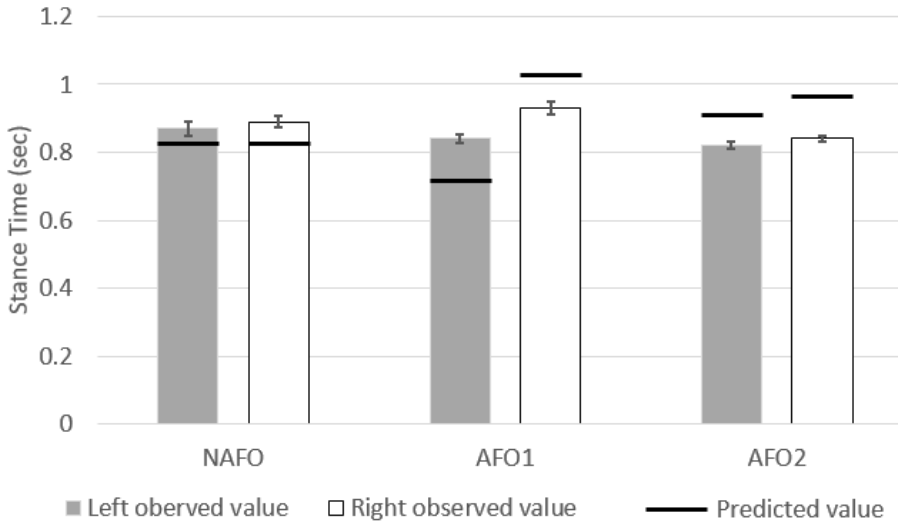

Figure 2-11: Comparisons between observed and predicted stance time for left (AFO) and right sides under each condition (*n* = 10). Values are mean ± SE.

2.4.2. Model Prediction for Six Subjects

The results of step lengths and swing time for the six additional subjects are summarized in this section to validate the model prediction. As shown in Figure 2-12, the predicted left and right step lengths were changing in the same trend as the observed step lengths for all conditions.

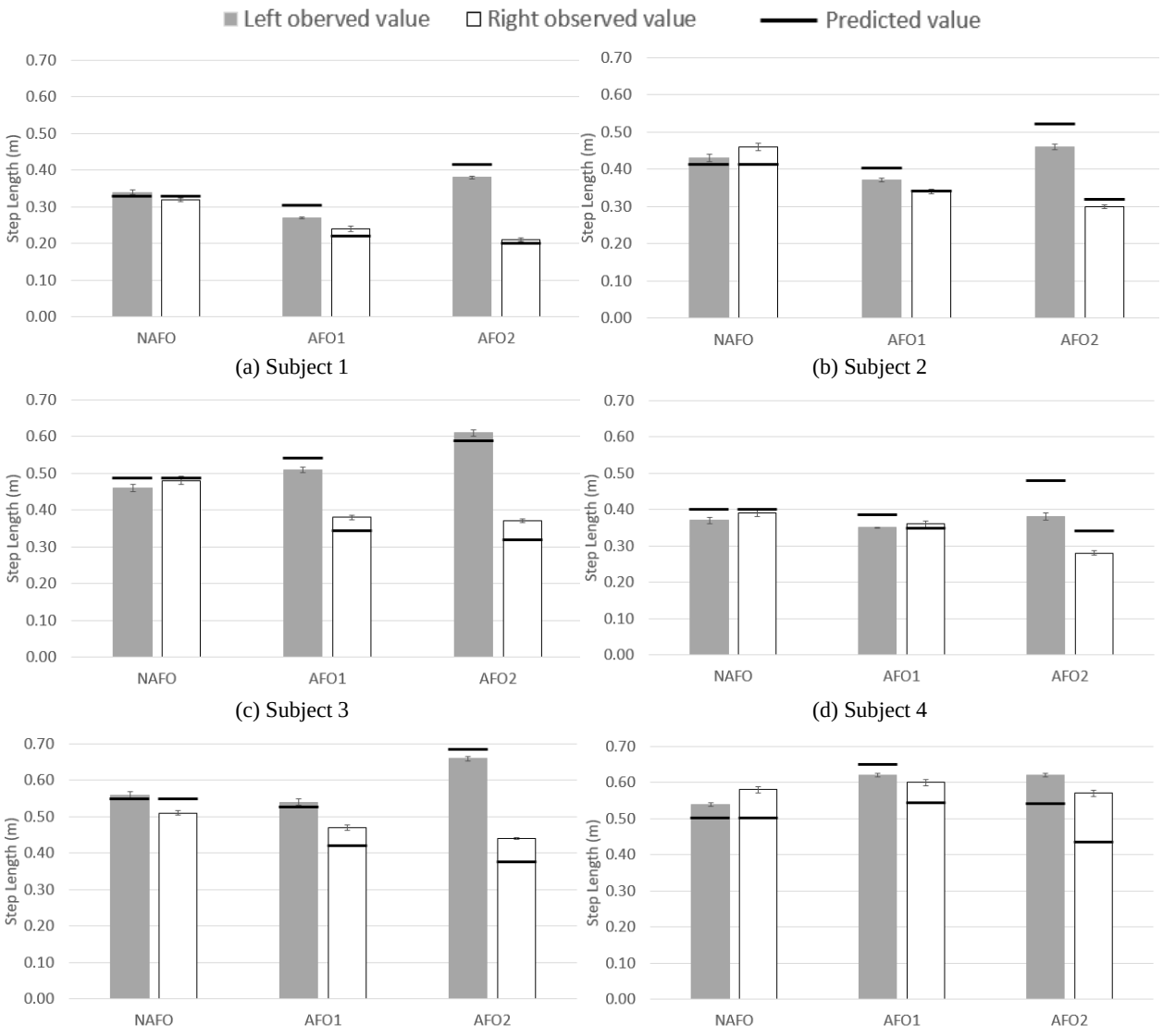

Figure 2-12: Comparison between observed and predicted step lengths for left (AFO) and right sides under each condition for six subjects (n = 40). Values are mean ± SE.

Similarly, the predicted left and right swing time were changing in the same trend as the observed swing time for all conditions as shown in Figure 2-13.

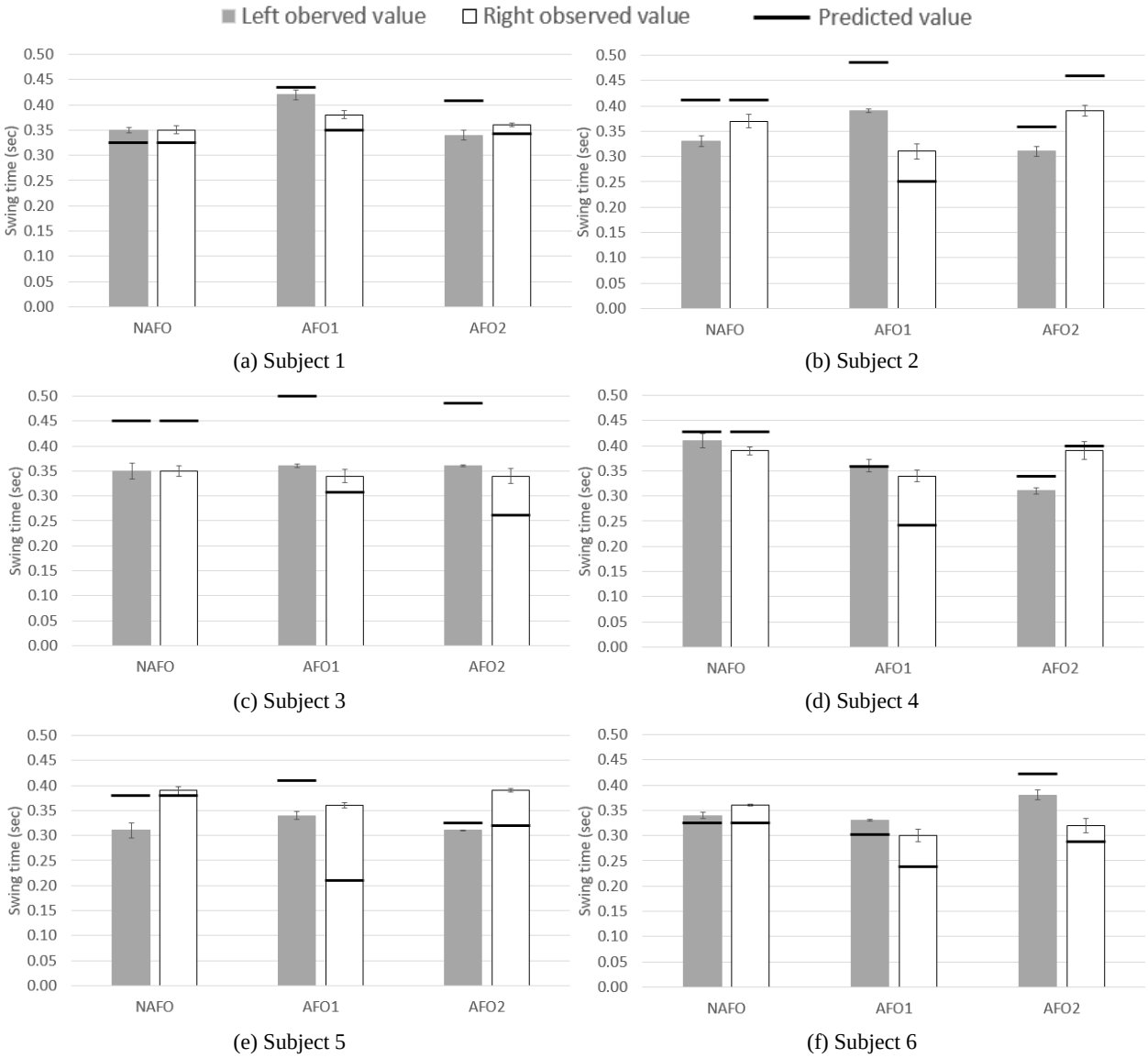

(a) Subject 1

(b) Subject 2

(c) Subject 3

(d) Subject 4

(e) Subject 5

(f) Subject 6

Figure 2-13: Comparison between observed and predicted swing time for left (AFO) and right sides under each condition for six subjects (n = 40). Values are mean ± SE.

2.5. Discussion

This study showed the capability of the proposed PPCLMP model in qualitatively predicting gait changes with AFOs of different stiffnesses. For both the AFO conditions, the model predictions revealed the trend of changing in gait parameters. There were also high correlations between observed and predicted joint angles for both hip and knee under all three

conditions (Table 2-8). Besides, the proposed model reveals how the AFO affects joint kinematics and gait parameters.

Overall, the model prediction had better agreement with observed data for the NAFO condition than for the AFO conditions (Figures 2-9, 2-10, 2-11, 2-12, and 2-13). For the NAFO condition, the predicted gait was symmetric on joint ROMs, step length, swing time, and stance time. However, the observed step lengths were longer for the left side (AFO side for AFO conditions) than the right side. Similarly, asymmetric patterns were found on all the other gait parameters. This asymmetric pattern for normal gait was quantitatively evaluated by using the symmetry index (SI) [66] and observed by a group of investigators [67,68]. They reported the SI of step length was ranged from 0 to 10%, and the SI of swing time was ranged from 0 to 9% for college students. The SI of step length from this study was 6%, and the SI of swing time was 5% under the NAFO condition. Both SIs were within the range from the previous investigations.

2.5.1. Knee ROM

The predicted greater peak knee flexion on the AFO side for AFO2 than for AFO1 might be explained by the energy generation process during the push-off (Table 2-9). Though the passive AFO releases energy during push-off and might decrease overall energy cost for walking [39], it constrained the ankle from performing a plantar flexion during the later push-off stage. Lewis et al. [69] and Malcolm et al. [70] observed that most of the push-off force at the ankle joint was generated when the ankle was in plantar flexion. Comparing with the normal gait, wearing the AFO1 might overall decrease the push-off power, and resulted in the observed and predicted decreasing peak knee flexion on the AFO side, or left side for the subject of this study. Despite the AFO2 was stiffer and constrained the ankle more from performing a plantar flexion,

it released more energy during the push-off. This could explain the predicted greater peak knee flexion on the AFO side for the AFO2 than for the AFO1.

Similarly, explanations can be found for the observed increasing peak knee flexion on the contralateral (right) side with increasing the AFO stiffness (Table 2-9). The AFOs stored energy during the SS, which slowed the forward rotation of the inverted pendulum [71]. To maintain the forward movement, the contralateral-side ankle, or right-side ankle for the subject of this study, had to push-off with greater power. Though the model assumed that the muscle torque patterns did not change between the AFO and NAFO conditions, it found a different dynamic state with greater initial knee angular velocities, greater initial knee angles, and less initial hip angles right after the push-off on the contralateral side as a feasible solution for the model (Table 2-7**Error! Reference source not found.**). Consequently, the model successfully predicted the increasing peak knee flexion with the increasing AFO stiffness. These findings are consistent with the observed excessive knee flexion with AFOs reported by [72].

2.5.2. Hip ROM and Step Length

Comparing with NAFO condition, the AFO-side and contralateral-side hip ROMs were decreased with the AFO1 for observed and predicted results, and consequently led to shorter step lengths on both sides (Table 2-9), which were consistent with the trend reported by other investigators [73,74]. The observed and predicted hip ROMs were not consistent for both sides under the AFO2 condition. As mentioned, the AFO could affect both sides' dynamics. For the AFO side, the AFO deaccelerated the push-off (late DS) by constraining the plantar flexion (Figure 2-8) and accelerated the push-off by releasing stored energy. Depending on which effect was dominant, the initial swing velocities on the AFO side might be increased or decreased. For the contralateral side, either the hip angular velocity at push-off or push-off force during DS

might be increased to compensate for the slowed inverted pendulum movement on the AFO side. However, this slowed movement might be compensated or partially compensated [8,75], which could result in similar hip ROM or reduced hip ROM on the contralateral side. The compensation done by the subject's muscle torque patterns changing might not be equivalent simulated by only changing the initial conditions. This individual compensation strategy might explain the inconsistency between observed and predicted hip ROMs with the AFO2.

2.5.3. Swing and Stance Time

The swing time and stance time were consistent between observed and predicted results under all conditions. The differences in the swing time and stance time among conditions could be explained similarly to the hip ROMs differences. The collective effect between the AFO stiffness and the compensations, either the muscle torque patterns change or the initial velocities change, led to the various gait timing.

2.5.4. Model Applications, Assumptions, and Limitations

The proposed model could form the basis of a decision support system for AFO design. It could be used to provide insight into how an AFO might change a person's gait, and help clinicians determining the appropriate AFO stiffness for each patient. Furthermore, with given movement patterns, the model has the potential to estimate the joint torque patterns based on the estimated lumped muscle parameters.

The two major assumptions of the proposed model were end conditions equaled to initial conditions and the front-knee at the initial conditions (back-leg TO) was straight. The error vectors revealed high agreement ($< 0.5°$ differences) between end angles and initial angles, and fair agreement ($\leqslant 12°$ per second differences) between end angular velocities and initial angular

velocities (Table 2-7). The better agreement in angle errors was due to the scalar factor (*f*) selection in Eq. (2-22). Furthermore, the contributions of initial angular velocities to error vectors were all low (<1%), which justified the scalar factor selection that weighed angular velocity errors less than the angle errors. This scalar factor could be changed to explore different weightings between angle errors and angular velocity errors. For real gait, the assumption of the end conditions equal to the initial conditions might not be true. As shown in Table 2-7**Error! Reference source not found.**, the observed initial conditions were variated among gait cycles. The subject might adjust muscle torque patterns to compensate for the different initial conditions and maintain continuous gait cycles, which could not be predicted by the model. Besides, by assuming the continuity of gait for both joint angles and angular velocities, the model assumed no energy loss, which was observed by a group of investigators during HS [76–78].

For the straight knee assumption, the observed knee flexion at initial TO was about 0° for NAFO condition and around 10° for AFO conditions. Besides, most of the literature reported less than 10° in knee flexion during the DS (Table 2-4). Comparing with a straight knee, 10° in knee flexion would only result in a 1.5% reduction in the front-leg length and was considered negligible in this model.

The model had three limitations: long processing time, spring representation of muscles, and constant lumped muscle parameters. The searching method for optimal initial conditions took several hours and could be improved. Currently, the model examined all combinations within the given range (Table 2-5) and then found the optimal initial conditions with the minimum global error. This process was time-consuming and required a lot of system memory. To reduce the amount of calculation, the step length, or prediction precision was limited to 1°

and 50° per second. An advanced searching algorithm might be useful to reduce the number of iterations, processing time, and increase prediction precision. Further investigations are needed to evaluate different search algorithms for the optimal initial conditions.

The lumped muscle parameters for the knee and hip joints were proposed based on the rotational spring representation of related muscles. This representation was simplified from Hill's muscle model [166] that has a contractile element and two spring elements, as shown in Figure 2-14. The viscoelasticity of muscles can be further represented by adding damping factors to the spring element. The simplification of the muscle model in this dissertation was proposed to reduce the dimensions of variables in the model. Further, Chapter 2 used constant lumped muscle parameters to characterize the joint torques generated by associated muscles. The constant lumped muscle parameter assumption ignores the adjustments, adaptions, and preferences of individuals among different scenarios. Due to this assumption, the model only shows the capability of qualitatively predicting gait parameter changes with different AFO stiffnesses.

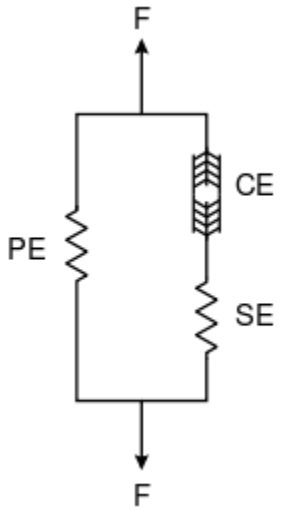

Figure 2-14: Hill muscle model that contains a contractile element (CE), a series spring element (SE), and a parallel spring element (PE). Diagram downloaded from [167].

The other limitation of this model was the assumption of homogenous muscle torque patterns for different people walking under different environments for different tasks. For a

human subject, walking without and with the AFO could involve different muscle torque patterns and different dynamic system states, like velocities and angles. However, the model only adapted the dynamic system states to look for a feasible solution without changing the muscle torque patterns. In other words, the model overestimated the AFO effect on gait. Unsurprisingly, the model predicted less hip ROM and less step length with the AFO2 (Table 2-9), which could be due to significant muscle torque patterns changes to compensate the stiffer AFO. For healthy subjects, the muscle torque patterns could be different between different genders, different ages, and even between individuals with similar anthropometry [79–81]. Furthermore, the final users of the AFOs would be drop foot patients, who could have various muscle strength and activity from a healthy subject with or without the AFOs [37,82–84]. How to determine the correct lumped muscle parameters in the model to make the prediction more individualized is challenging.

Known individual movement patterns could be helpful in determining individual lumped muscle parameters to improve the gait prediction. Luckily, wearable technologies become more available nowadays. As most commonly used gait tracking wearable devices, inertia measurement units (IMUs) have advantages in its accuracy, less intrusive, and robustness in challenging environments [61,85–87]. Most of the studies focused on mounting multiple IMUs for gait tracking, but orthotic clinical applications may only accept a limited number of IMUs. With the proposed model, mounting only one IMU on the AFO would be enough to acquire the needed data to estimate the muscle torque patterns of the person while wearing the AFO for in and post clinical evaluations of the AFO designs. Further investigations are needed to evaluate the IMU assisted prediction.

2.6. Conclusions

The PPCLMP model has the capability to qualitatively predict gait parameter changes with the different ankle stiffnesses in the forward-dynamic mode. The model prediction had the same trend as the experimental measurements regarding step length and swing time. The ankle stiffness increased by the AFO affects the gait in two ways. During the SS, the AFO stiffness slows down the inverted pendulum movement and stores energy. During the DS with the AFO on the back-leg, the AFO releases energy when the ankle is in dorsiflexion but prevents the ankle from generating more energy when the ankle is in plantar flexion. These findings explain how AFO affects gait from the energy perspective besides simply helping lift the foot during SW. Because the lumped muscle parameters in the model were separately estimated based on joint torques reported by a previous study and did not change among different conditions, the model is limited on quantitatively predicting gait parameters regarding step length, swing time, and stance time.

CHAPTER 3 Utilization of the Inertial Measurement Unit for Evaluation of Gait with Passive Dynamic Ankle-foot Orthosis based on the PPCLMP Model

Abstract

This study aims to utilize the data from a single inertial measurement unit (IMU) attached to the passive-dynamic ankle-foot orthosis (AFO) to enhance the planar piecewise continuous lumped muscle parameter (PPCLMP) model for predicting gait patterns. An algorithm utilizing IMU's accelerometer, gyroscope, and magnetometer measurements was developed to estimate the initial conditions and lumped muscle parameters for each gait cycle based on the inverse-dynamic mode of the PPCLMP model. The observed step length, swing time, and stance time using five IMUs (one on each thigh, one on the unimpaired-side shank, one on the impaired-side shank as attached to the AFO, and one on the lower back trunk of the subject) were compared with model prediction results for two patients with drop foot syndrome while walking without and with AFOs with low and high stiffnesses (3.6 and 4.5 Nm/deg). The data from the IMU attached to the AFO was utilized to estimate the optimal initial conditions and lumped muscle parameters of the model for gait prediction. The root mean square errors (RMSEs) of the predicted impaired-side step length, unimpaired step length, and the swing time were less than 0.09 m, less than 0.20 m, and less than 6% of gait duration, respectively.

3.1. Introduction

Various conditions of birth, injuries, and diseases that affect ankle stiffness may adversely affect gait patterns. About 80% of multiple sclerosis (MS) population experience gait problems [88,89], and 20% of the stroke population are affected by the drop foot syndrome during their rehabilitation [65,90,91]. Drop foot gait is asymmetric and different from normal gait. Kottink et al. [5] and Don et al. [8] demonstrated that drop foot patients used two compensatory strategies, increasing the hip abduction or knee flexion angle on the impaired side during the swing phase (SW), to avoid stubbing their toes. Drop foot patients were also found to have shorter step length and longer swing time on the impaired side [6,7]. The differences between the impaired and unimpaired sides resulted in asymmetric gait, which was also considered inefficient.

Ankle-foot orthoses (AFOs) are frequently used to enhance ankle stiffness and help restore gait function for drop foot patients [73,92,93]. Bartonek et al. [73] and Radtka et al. [94] observed increased walking speed (10%) and step length (6%) on the impaired side during SW for a patient's gait while wearing AFOs. The bending stiffness of AFO was found to be the main effect that could affect step length, walking speed, and gait symmetry [91,95,96].

To evaluate pathological gait and the gait improvement made by AFOs, several quality metrics were developed. Gait symmetry index (SI), or Robinson Index [66], was proposed to evaluate the quality of the patient's gait [97–99]:

$$SI = 2\frac{|X_R - X_L|}{X_R + X_L} \times 100\% \tag{3-1}$$

where X_R is the gait parameter on the right side, and X_L is the gait parameter on the left side. Examples of X include the step length and swing time. In addition to the SI, faster walking speed and less energy expenditure during gait have been used as signs of gait improvement [100–103].

While most pathological gait evaluations were performed within laboratory or clinical settings with dedicated optical tracking systems, investigation on patients' gaits with AFOs during daily activities is limited. Because the optical tracking systems are expensive, intrusive, and require structured environments, the cheaper and less intrusive wearable motion tracking system is desirable in measuring the human gait during daily activities [104–108].

Inexpensive inertial measurement units (IMUs) that measure three axes of accelerations, angular velocities, and headings have been utilized for gait tracking in recent studies to estimate gait parameters [61,109–111]. IMUs can be integrated with microprocessors and communication modules to record and transmit data over several days to a server for gait evaluation as patients go about their activities of daily living, work, or recreation. Li et al. [112] estimated the gait speed with a root mean squared error (RMSE) of only 7% based on the data from a shank-mounted IMU. Sijobert et al. [113] instrumented one IMU on the patient's shank to detect the freezing of gait in the early stage of Parkinson's disease. Similar to mounting on the shank, IMU could be attached to the back of the AFO calf (Figures 3-1(a) and (b)) to provide kinematic data of the gait.

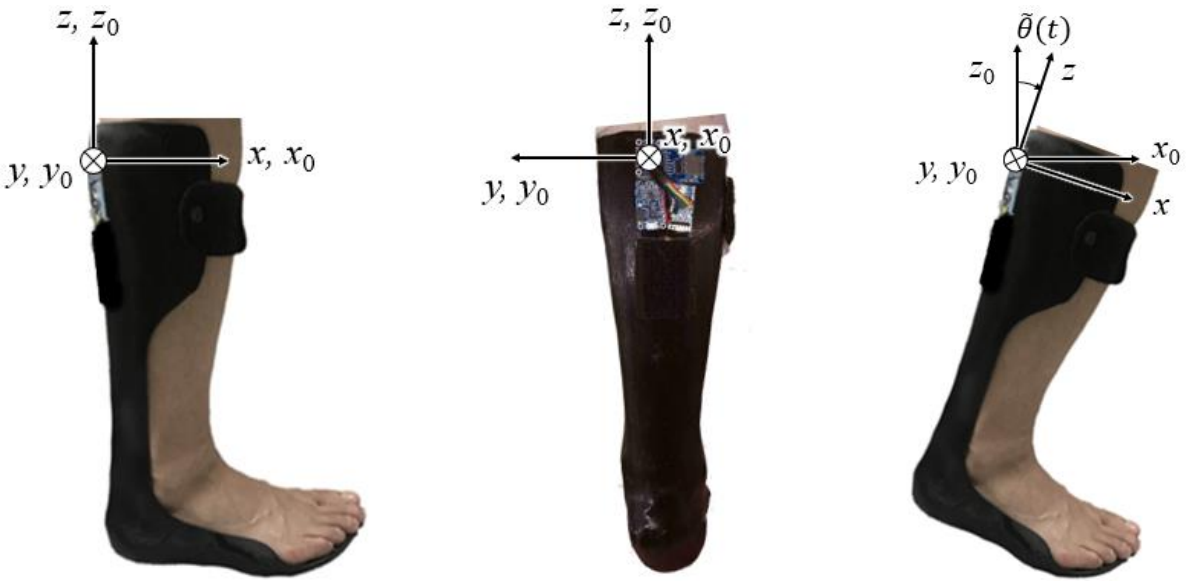

(a) (b) (c)

Figure 3-1: The global coordinate system (x_0-, y_0-, and z_0-axes) and local coordinate system (x-, y-, and z-axes) of the IMU defined in this study from (a) the side view of the IMU-attached AFO and (b) the back view of the IMU-attached AFO, and (c) the local coordinate system of the IMU attached to the back of the AFO calf rotating with respect to the global coordinate system in the sagittal plane (side view).

To interpret the IMU data, the planar piecewise continuous lumped muscle parameter (PPCLMP) model proposed in Chapter 2 is used. The model represents the lower limbs' segments as homogenous rod links with lengths of L_i and uniformly distributed masses of M_i. Adjacent segments are connected by a hinge joint with joint torque linearly changing with the joint angle. This linear relationship is represented by lumped muscle parameters in the model. Furthermore, the model characterizes the single stance phase (SS) by an inverted pendulum, the double stance phase (DS) by a kinematic chain, and the SW by a double pendulum. The joint angles and angular velocities are continuously transferred between adjacent phases so that the joint angles and angular velocities at the end of one phase are equal to those values at the start of the next phase. The model can be used to describe the gait starting from the toe-off (TO) and ending at the next TO of the same side based on the initial conditions and lumped muscle parameters for the gait cycle. This model is limited by the assumption of constant lump parameters, which assumes the same joint torque patterns for gaits with different joint stiffnesses

and among different people. Variabilities among gaits of the same person with different joint stiffnesses and among gaits of different people are not investigated. Instead of assuming constant lumped muscle parameters for all gaits, the lumped muscle parameters for each gait cycle could be estimated based on the kinematic data measured by the IMU attached to AFO. In addition, the kinematic data could be utilized to estimate the initial conditions of each gait cycle at the TO.

The goal of this study is to utilize the data measured from the IMU attached to AFO to improve the gait prediction of the PPCLMP model and use the predicted gait for gait evaluation. The hypothesis is that the model prediction accuracy can be increased by utilizing the data from IMU. Section 3.2 derives the algorithm that estimates the initial conditions and lumped muscle parameters for each gait cycle based on the IMU data. Section 3.3 outlines the experimental setup to measure the walking gaits of two drop foot patients. Section 3.4 compares the model-predicted and the experimentally observed gait parameters of two drop foot patients. Section 3.5 discusses the algorithm estimation accuracy, model prediction accuracy, and potential model applications in evaluating gait with AFOs.

3.2. Algorithm for Estimating Initial Conditions and Lumped Muscle Parameters based on IMU Data – Inverse Dynamics

3.2.1. Overview

To estimate the initial conditions and lumped muscle parameters in the PPCLMP model for each gait cycle, an algorithm is developed to utilize the kinematic data measured by the IMU attached to the back of the AFO calf. The IMU data are first processed by a framework that identifies gait events, calculates phase durations, and estimates shank pitch angles and angular velocities. The duration of gait phases and estimated shank pitch angles and angular velocities

are utilized as constraints in an optimization problem to search for the optimal initial conditions and lumped muscle parameters for the gait cycle. The initial conditions and lumped muscle parameters are inputs for the PPCLMP model to predict and evaluate gait.

3.2.2. Framework for Gait Event Identification and Angle Estimation

As shown in Figures 3-1(a) and (b), the IMU is attached to the AFO in the way that the *x*-, *y*-, and *z*-axes of the IMU's local coordinate are aligned with the global anterior-posterior (x_0-axis), lateral-medial (y_0-axis), and superior-inferior axes (z_0-axis), respectively, while the subject is standing. Because the PPCLMP model only characterizes body movements in the sagittal plane, this study has a special interest in the pitch angle, $\tilde{\theta}(t)$, which the IMU, or shank, rotates about the *y*-axis with in the sagittal plane as shown in Figure 3-1(c).

Figure 3-2 shows the framework for gait event identification and angle estimation based on the IMU measurements. The IMU measures: 1) three accelerations ($\tilde{a}_x(t)$, $\tilde{a}_y(t)$, and $\tilde{a}_z(t)$) from the accelerometer, 2) three angular velocities ($\tilde{\omega}_x(t)$, $\tilde{\omega}_y(t)$, and $\tilde{\omega}_z(t)$) from the gyroscope, and 3) three headings (yaw $\tilde{\varphi}(t)$ for the *x*-axis, pitch $\tilde{\theta}(t)$ for the *y*-axis, and roll $\tilde{\gamma}(t)$ for the *z*-axis) from the magnetometer. The accelerations measured by IMU are inputs to identify the gait events. The angular velocity for the *y*-axis, $\tilde{\omega}_y(t)$, and pitch angle, $\tilde{\theta}(t)$, measured by IMU are used to determine the shank pitch angles and angular velocities at gait events.

The gait event identification algorithm [114] is utilized to determine the time of the initial TO, t_0, heel strike (HS), t_1, and end TO, t_2, based on the resultant acceleration. The swing time of the impaired side, t_{SW}, is calculated as

$$t_{SW} = t_1 - t_0 \tag{3-2}$$

Similarly, the stance time of the impaired side, t_{ST}, which is the time duration of one SS of the impaired side and two DSs before and after the SS, is calculated as

$$t_{ST} = t_2 - t_1 \tag{3-3}$$

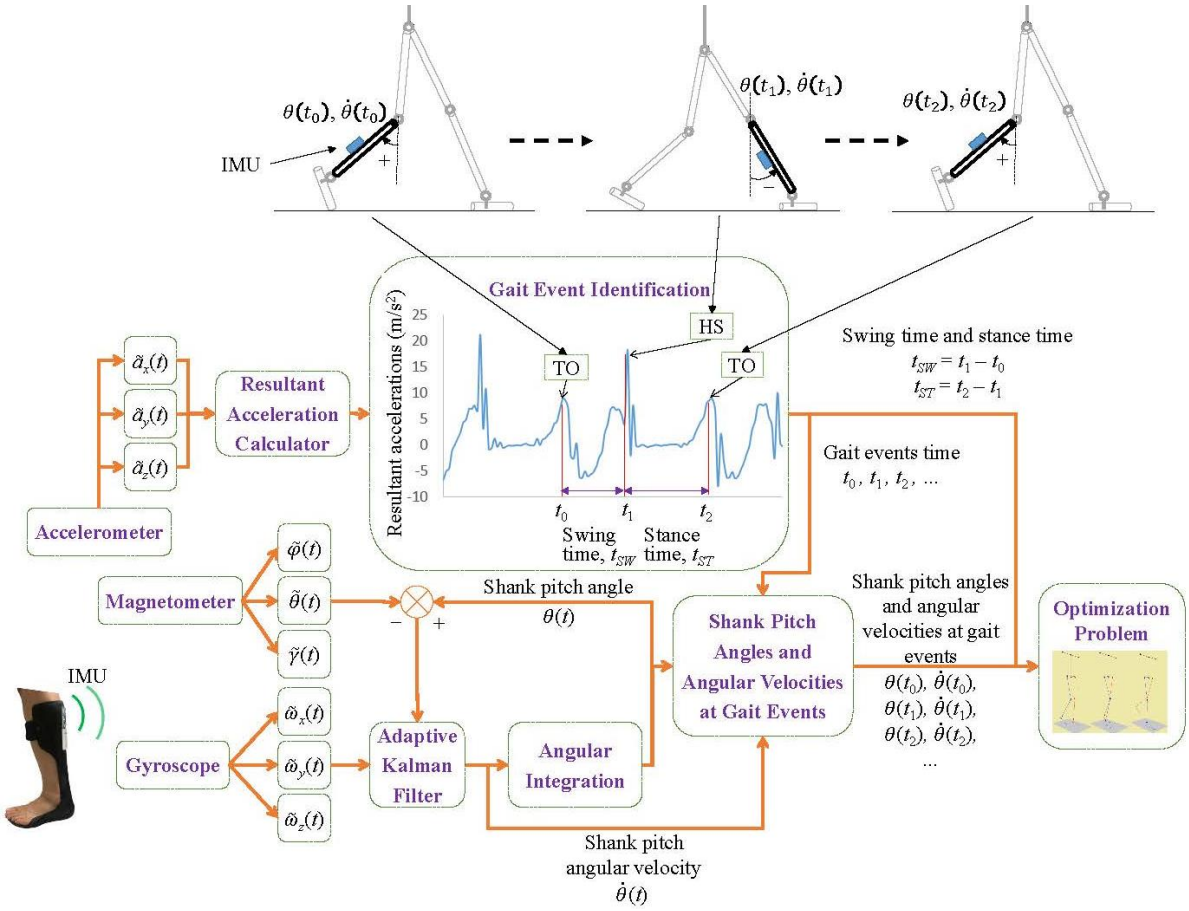

Figure 3-2: The framework for gait event identification and angle estimation based on accelerations, angular velocities, and headings measured by the IMU. The peaks of resultant acceleration measured from the accelerometer are used to identify the gait events and calculate swing and stance time. The angular velocities measured from the gyroscope and the headings measured from the magnetometer are used to calculate the shank pitch angle and angular velocities. The swing and stance time and shank pitch angles and angular velocities then are used as the constraints in the optimization problem to find the optimal initial conditions and lumped muscle parameters.

Since there is redundancy in the heading and angular velocity measurements, the adaptive Kalman Filter [109] can be applied to reduce the drift in the angular velocity measurement by utilizing the heading measurement for better angle estimation. The Kalman-Filter processed shank pitch angular velocity, $\dot{\theta}(t)$, is utilized to calculate the shank pitch angle, $\theta(t)$, via angular

integration. The $\theta(t)$ is compared with the measured pitch angle, $\tilde{\theta}(t)$, to estimate the drift in the angular velocity measurements. The $\theta(t)$ and $\dot{\theta}(t)$ are used to find the shank pitch angles ($\theta(t_0)$, $\theta(t_1)$, $\theta(t_2)$) and angular velocities ($\dot{\theta}(t_0)$, $\dot{\theta}(t_1)$, and $\dot{\theta}(t_2)$) at the identified gait events.

3.2.3. Optimization Problem for Searching the Initial Conditions and Lumped Muscle Parameters

An optimization problem is constructed to use the estimated swing time, stance time, and shank pitch angles and angular velocities at gait events as constraints to search for the optimal initial conditions (the IMU only provides the initial shank pitch angle and angular velocity while the initial joint angles of the lower limbs are unknown) and lumped Muscle parameters of the PPCLMP model, as shown in Figure 3-3. The model then estimates the gait parameters and calculates the quality metrics of gait symmetry and efficiency to evaluate the gait.

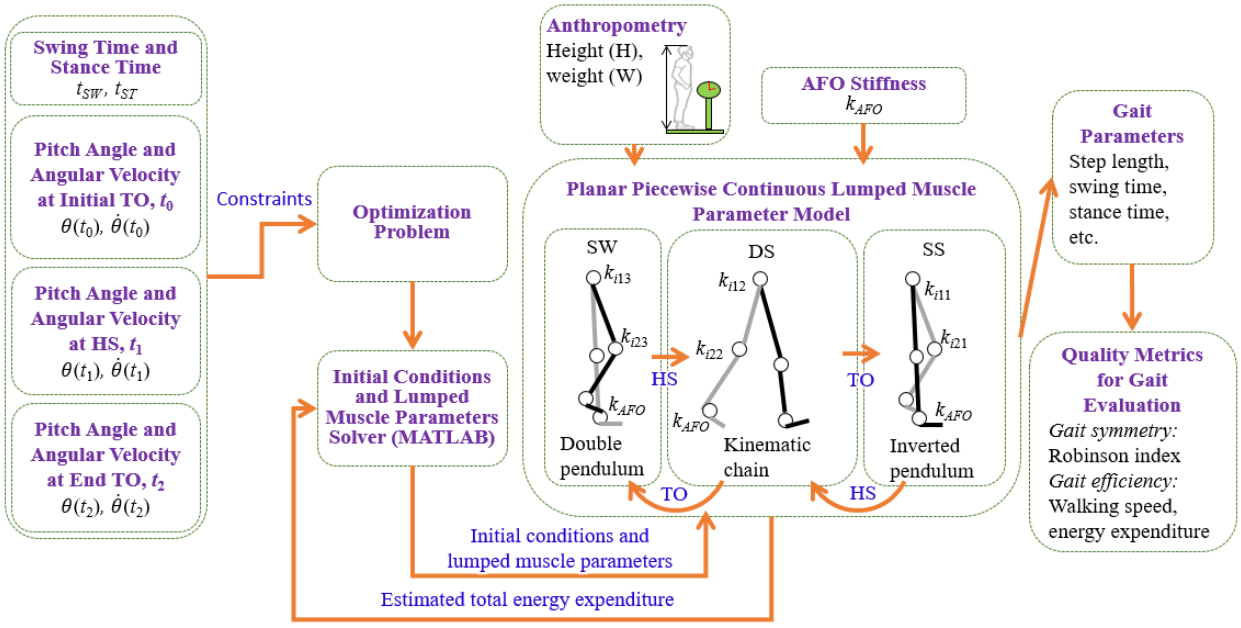

Figure 3-3: The optimization problem for searching the optimal initial conditions and lumped muscle parameters for model prediction and gait evaluation based on the estimated swing time, stance time, and shank pitch angles and angular velocities at identified gait events to minimize estimated total energy expenditure.

3.2.3.1 Initial Conditions at the TO

Since the IMU could only provide the pitch angle and angular velocity of the shank, this section derives the quantitative relationship between the initial joint angles and shank pitch angle. This relationship is further used to decrease the variable dimension of the optimization problem proposed in this study.

Because the IMU is attached to the AFO, which is strapped to the impaired leg, the IMU-identified TO is the impaired-side TO. Thus, the front-leg is the unimpaired leg, and the back-leg is the impaired leg at this TO (Figure 3-4). There are six joint angles determining the initial posture at this TO: 1) the impaired-side hip angle, $\theta_{11}(t_0)$, 2) the impaired-side knee angle, $\theta_{12}(t_0)$, 3) the impaired-side ankle angle, $\theta_{13}(t_0)$, 4) the unimpaired-side hip angle, $\theta_{21}(t_0)$, 5) the unimpaired-side knee angle, $\theta_{22}(t_0)$, and 6) the unimpaired-side ankle angle, $\theta_{23}(t_0)$. All these joint angles are measured from the standing neutral posture angles. Flexion directions (dorsiflexion for ankle joint) are considered positive, and extension directions (plantar flexion for ankle joint) are considered negative.

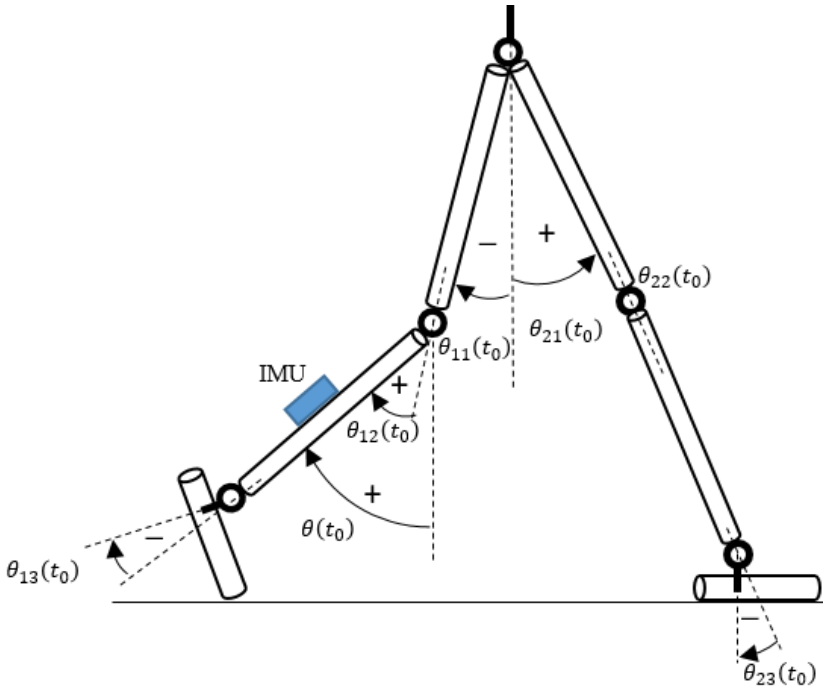

Figure 3-4: The geometry and angle definitions at the impaired-side TO, t_0, as shown in Figure 3-2.

The model assumes the front-knee is straight [58,61,64] and the front-foot is flat on the ground at the TO. Thus, the unimpaired-side joint angles and angular velocities at the TO satisfy:

$$\theta_{22}(t_0) = \dot{\theta}_{22}(t_0) = 0 \tag{3-4}$$

$$\theta_{23}(t_0) = -\theta_{21}(t_0) \tag{3-5}$$

$$\dot{\theta}_{23}(t_0) = -\dot{\theta}_{21}(t_0) \tag{3-6}$$

which means the unimpaired-side leg posture at the TO is only determined by the hip joint angle, $\theta_{21}(t_0)$, or the ankle joint angle, $\theta_{23}(t_0)$. In this way, the number of joint angles determining the initial posture at the TO is reduced to four: $\theta_{11}(t_0)$, $\theta_{12}(t_0)$, $\theta_{13}(t_0)$, and $\theta_{21}(t_0)$. For the impaired-side leg, the estimated shank pitch angle, $\theta(t)$, and angular velocity, $\dot{\theta}(t)$, are:

$$\theta_{12}(t) - \theta_{11}(t) = \theta(t) \tag{3-7}$$

$$\dot{\theta}_{12}(t) - \dot{\theta}_{11}(t) = \dot{\theta}(t) \tag{3-8}$$

Because the back-toe and front-foot are assumed on the ground at the TO, the front-hip (unimpaired-side hip) joint angle at the TO, $\theta_{21}(t_0)$, is:

$$(L_1 + L_2)\cos\theta_{21}(t_0) = L_4\cos(\theta_{12}(t_0) - \theta_{11}(t_0) - \theta_{13}(t_0)) - L_4 + L_3\sin(\theta_{12}(t_0) - \theta_{11}(t_0) - \theta_{13}(t_0)) + L_2\cos(\theta_{12}(t_0) - \theta_{11}(t_0)) - L_1\cos\theta_{11}(t_0) \quad (3\text{-}9)$$

where L_1 is the upper leg length, L_2 is the lower leg length, L_3 is the foot length, and L_4 is the ankle height. Based on Eq. (3-7), Eq. (3-9) can be rewritten as:

$$\theta_{21}(t_0) = \text{acos}\left(\frac{L_4\cos(\theta(t_0) - \theta_{13}(t_0)) - L_4 + L_3\sin(\theta(t_0) - \theta_{13}(t_0)) + L_2\cos\big(\theta(t_0)\big) - L_1\cos\theta_{11}(t_0)}{L_1 + L_2}\right) \quad (3\text{-}10)$$

To summarize, if $\theta(t_0)$, $\theta_{11}(t_0)$, and $\theta_{13}(t_0)$ are known, the other joint angles at the TO can be estimated based on Eqs. (3-5), (3-7), and (3-10).

3.2.3.2 Lumped Muscle Parameters

There are 10 lumped muscle parameters as listed in Table 3-1. The hip and knee lumped muscle parameters are used to describe the linear relationship between the hip and knee joint torques and the associated joint angles. The joint torques are estimated as:

$$T_{ijp} = k_{ijp}\theta_{ij} \quad (3\text{-}11)$$

where *i* represents the side (1 for the impaired side and 2 for the unimpaired side), *j* represents the joint (1 for the hip joint and 2 for the knee joint), and *p* represents the phase (1 for SS, 2 for DS, and 3 for SW). Since the push-off ankle torque during DS does not follow the spring property [13], a lumped ankle torque is separately applied during DS based on the body mass. The ankle torque of the unimpaired side is estimated based on the body mass as:

$$T_{232} = r_{232}M_0 \quad (3\text{-}12)$$

where M_0 is the body mass and r_{232} (the first 2 represents the unimpaired side, 3 represents the ankle joint, and the second 2 represents the DS phase) is the lumped muscle parameter of the unimpaired-side ankle.

The ankle torque of the impaired side is affected by the AFO stiffness and estimated as:

$$T_{132} = r_{132}M_0 + k_{AFO}\theta_{13} \tag{3-13}$$

where r_{132} is the lumped muscle parameter of the impaired-side ankle and k_{AFO} is the AFO stiffness that is simulated by changing the ankle stiffness.

Table 3-1: Summary of 10 lumped muscle parameters in the model.

Side	Phase	Lumped muscle parameter	Representation
Impaired	DS	Hip	k_{112}
		Knee	k_{122}
		Ankle	r_{132}
	SW	Hip	k_{113}
		Knee	k_{123}
Unimpaired	DS	Hip	k_{212}
		Knee	k_{222}
		Ankle	r_{232}
	SW	Hip	k_{213}
		Knee	k_{223}

For each gait cycle (from initial TO, t_0, to end TO, t_2), there are two initial joint angles ($\theta_{11}(t_0)$ and $\theta_{13}(t_0)$), two initial joint angular velocities ($\dot{\theta}_{11}(t_0)$ and $\dot{\theta}_{13}(t_0)$), and ten lumped muscle parameters (Table 3-1) needed to be solved. The constraints need to be satisfied are the information provided by the IMU: three shank pitch angles ($\theta(t_0)$, $\theta(t_1)$, and $\theta(t_2)$), three shank pitch angular velocities ($\dot{\theta}(t_0)$, $\dot{\theta}(t_1)$, and $\dot{\theta}(t_2)$), swing time (t_{SW}), and stance time (t_{ST}).

3.2.3.3 Optimization Problem

To find the optimal initial conditions and lumped muscle parameters for each gait cycle, an optimization problem is constructed. Since the most commonly used objective function for gait simulation is minimizing system energy expenditure [115–117], the objective function for this study is proposed as minimizing the model estimated total energy expenditure at the hip, knee, and ankle joints for each gait cycle:

$$\min_{\boldsymbol{x}} \quad \sum_{i=1}^{2}\left(\int T_{i32}dt + \sum_{j=1}^{2}\sum_{p=1}^{3}\int k_{ijp}\theta_{ijp}(t)dt\right) \tag{3-14}$$

where $\int T_{i32}dt$ is the total energy expenditure at the ankle joint and $\sum_{j=1}^{2}\sum_{p=1}^{3}\int k_{ijp}\theta_{ijp}(t)dt$ is the total energy expenditure at the hip and knee joints. $\boldsymbol{x}$ is the variable vector, which can be written as:

$$\boldsymbol{x} = \{\theta_{11}(t_0), \theta_{13}(t_0), \dot{\theta}_{11}(t_0), \dot{\theta}_{13}(t_0), k_{112}, k_{122}, r_{132}, k_{113}, k_{123}, k_{212}, k_{222}, r_{232}, k_{213}, k_{223}\} \quad (3\text{-}15)$$

where the first four elements are the initial joint angles and angular velocities and the rest elements are the lumped muscle parameters listed in Table 3-1.

To satisfy the IMU measured swing time and stance time, the equality constraints are defined as:

$$t_{SWP} = t_{SW} \quad (3\text{-}16)$$

$$t_{DS1P} + t_{SSP} + t_{DS2P} = t_{ST} \quad (3\text{-}17)$$

where t_{SWP} is the model-predicted SW time of the impaired side, t_{DS1P} is the model-predicted DS time with the impaired leg in front, t_{SSP} is the model-predicted SS time of the impaired side, and t_{DS2P} is the model-predicted DS time with the impaired leg behind.

Furthermore, to satisfy the IMU measured shank pitch angles and angular velocities at the TOs and HS, the inequity constraints are defined as:

$$\left|\left|(\theta_{12}(t_1) - \theta_{11}(t_1))\right| - \theta(t_1)\right| \leq \varepsilon_1 \quad (3\text{-}18)$$

$$\left|\left|\dot{\theta}_{12}(t_1) - \dot{\theta}_{11}(t_1)\right| - \dot{\theta}(t_1)\right| \leq \varepsilon_2 \quad (3\text{-}19)$$

$$\left|\left|\theta_{12}(t_2) - \theta_{11}(t_2)\right| - \theta(t_2)\right| \leq \varepsilon_1 \quad (3\text{-}20)$$

$$\left|\left|\dot{\theta}_{12}(t_2) - \dot{\theta}_{11}(t_2)\right| - \dot{\theta}(t_2)\right| \leq \varepsilon_2 \quad (3\text{-}21)$$

where ε_1 is the error tolerance for angle prediction and ε_2 is the error tolerance for angular velocity prediction.

Because this optimization problem is non-linear and non-convex, the enumeration search method [118,119] is utilized to solve this problem. The searching boundaries of the variable

vector, $\boldsymbol{x}$, for the enumeration method are listed in Table 3-2. The searching boundaries of the lumped muscle parameters are set from 1 Nm/deg to twice the values estimated from Winter [13]. The boundaries of initial angular values are set based on the normal range in the literature review in Table 2-4. The error tolerance for angle predictions, ε_1, is set to 1°, and the error tolerance for angular velocity predictions, ε_2, is set to 10° per second.

Table 3-2: Ranges of the initial conditions and lumped muscle parameters for the enumeration method and the ranges of AFO stiffness and subject parameters for the sensitivity analysis.

Ranges for the enumeration method	Variables	Unit	Range (start, stop, step)
Initial conditions	$\theta(t_0)$	Deg	(–75, –25, 1)
	$\theta_{11}(t_0)$	Deg	(–30, –5, 1)
	$\theta_{13}(t_0)$	Deg	(–45, 0, 1)
	$\dot{\theta}(t_0)$	Deg	(–170, 0, 10)
	$\dot{\theta}_{11}(t_0)$	Deg/s	(100, 150, 10)
	$\dot{\theta}_{13}(t_0)$	Deg/s	(100, 450, 10)
Lumped muscle parameters	k_{ij2}	Nm/deg	(1,20,1)
	k_{ij3}	Nm/deg	(1,40,1)
	r_{i32}	Nm/kg	(0.1,3,0.1)
Additional ranges for the sensitivity analysis	Variable	Unit	Values to be tested
AFO stiffness and anthropometry	k_{AFO}	Nm/deg	0, 3.6, 4.5
	Gender	-	M, F
	L_0*	m	1.51, 1.70, 1.88
	M_0	kg	51, 88, 125

*L_0 is the stature.

3.2.4. Sensitivity Analysis

A sensitivity analysis was performed to investigate the effects of the initial conditions, lumped muscle parameters, AFO stiffness, gender, stature, and body mass on gait parameters within the range listed in Table 3-2. The AFO stiffness was selected based on the measured stiffnesses of two AFOs. The stature and body mass were selected to cover the stature and body mass ranged from 5th percentile female to 95th percentile male reported by ANSUR Data [53]. To reduce the number of enumerations, only the start, stop, and mean of the start and stop values for initial conditions and lumped muscle parameters were used in the sensitivity analysis.

The contribution of each variable is listed in

Table 3-3. The unimpaired-side step length increased with increasing stature and initial shank pitch angle. This was consistent with the findings that step length should be proportional to the stature [57,62]. The impaired-side step length increased with increasing joint angular velocities. The SW time of the impaired side decreased with increasing initial angular velocities of the AFO. This implied that the initial angular velocities had more impact on the SW time than initial angles, which was consistent with the findings in Chapter 2. The time of the DS with the impaired side in front was decreased with increasing unimpaired-side ankle torque. This was because the unimpaired-side ankle torque was the main power source to activate the DS movement. The SS time of the impaired side increased with increasing AFO stiffness and with decreasing ankle torque of the unimpaired side during DS. The longer SS time with higher AFO stiffness was consistent with the hypothesis made in Chapter 2: the AFO at ankle joint prevented the inverted pendulum from swing forward. The ankle torque of the unimpaired side during DS (with the impaired side in front) determined the initial state of the SS of the impaired side. The DS time with the unimpaired side in front was not significantly (>10% contribution) affected by any input tested.

Table 3-3: Percent contribution of variations in the initial conditions, lumped muscle parameters, AFO stiffness, gender, stature, and body mass to variations in gait parameters.

Input	Variable	D_U	D_I	t_{SWP}	t_{DS1P}	t_{SSP}	t_{DS2P}
Initial conditions	$\theta(t_0)$	39(+)		1	1	1	
	$\theta_{11}(t_0)$	32(–)	1	5	2	3	
	$\theta_{13}(t_0)$	6	1	2			
	$\dot{\theta}(t_0)$		16(+)	27(–)			
	$\dot{\theta}_{11}(t_0)$		10	4	6	4	
	$\dot{\theta}_{13}(t_0)$			1			
Lumped muscle parameters	k_{113}		8		4	3	
	k_{123}		1	17(–)	4	3	
	k_{112}						6
	k_{122}						
	k_{213}	7			1	9	
	k_{223}	1					
	k_{212}						
	k_{222}				2	2	
	r_{132}	3					1
	r_{232}				22(–)	22(–)	
Anthropometry and AFO	k_{AFO}				9	13(+)	1
	Gender						
	L_0	23(+)	1		9	2	2
	M_0		6		6	4	4

* (+) represents a positive relationship between variables and (–) represents a negative relationship between variables for contribution greater than 10%. Contributions that less than 1% are not included. D_I is the step length of the impaired side, and D_U is the step length of the unimpaired side.

3.2.5. Algorithm Summary

The proposed algorithm (Figures 3-2 and 3-3) is used to estimate the initial conditions and lumped muscle parameters for each gait cycle based on the data from an IMU sensor attached to AFO. The IMU data are used to estimate the swing and stance time of the impaired side and the pitch angle and angular velocity of the impaired-side shank. This information then is used to search for the optimal initial conditions and lumped muscle parameters for the lowest energy expenditure predicted by the model for each gait cycle. The optimal initial conditions and lumped muscle parameters are used in the model to estimate gait parameters and evaluate gait.

3.3. Subjects and Methods

To test the proposed PPCLMP model, observed and predicted gait parameters were compared for one male and one female subjects with drop foot syndrome wearing AFOs. Both subjects suffered drop foot syndrome on their left side, denoted as impaired side hereafter, due to

spastic hemiparesis. The anthropometric data of the two subjects are shown in Table 3-4. The body link lengths were directly measured from the subjects. The body link masses were estimated based on the measured subjects' body masses and mass ratios reported by Drillis and Contini [16]. Each subject was prescribed with a plaster-molded AFO (AFO1) and a 3D-printed AFO (AFO2). AFO1's stiffness was 3.6 Nm/deg, and AFO2's stiffness was 4.5 Nm/deg.

Table 3-4: Anthropometry of Subjects 1 and 2 and the stiffnesses of AFOs used in the experiment.

	Subject	Subject 1		Subject 2	
	Gender	Male		Female	
	Age	62		26	
Body link length (m)	Stature, L_0	1.96		1.69	
	Upper leg length, L_1	0.47		0.33	
	Lower leg length, L_2	0.45		0.36	
	Mid-foot length, L_3	0.20		0.16	
	Ankle height, L_4	0.11		0.10	
	Heel length, L_5	0.06		0.05	
	Fore-foot length, L_6	0.05		0.04	
Body link mass* (kg)	Body mass, M_0	113		49	
	Upper leg mass, M_1	15		6.5	
	Lower leg mass, M_2	5		2.2	
	Foot mass, M_3	1.6		0.7	
	Upper body mass, M_4	70		30	
AFO stiffness (Nm/deg)		AFO1	AFO2	AFO1	AFO2
		3.4	6.9	3.4	6.9

* The mass for each segment was estimated based on the measured body mass of the subject and the link-mass ratios reported by Drillis and Contini [16].

The goal, experimental procedure, and possible risks were explained to the subjects before participation. Each subject signed the informed consent form approved by Institutional Review Boards of the University of Michigan (HUM00090458).

A five-IMU system, LEGSys^{TM} (BioSensics LLC, Newton, MA, USA), was used to measure shank and hip planar movements at a 100 Hz sampling rate and calculate step length, swing time, and stance time using the algorithm described by Chen et al. [120]. The IMU attachment is shown in Figure 3-5 with one IMU on each thigh, one on the unimpaired-side shank, one on the impaired-side shank, and one on the lower back trunk of the subject. Separately, the IMU attached to the impaired shank was used as the IMU attached to AFO to

predict the gait parameters based on the PPCLMP model for comparison with the observed gait parameters based on the five-IMU system.

Each subject was asked to perform level ground walking without AFO (NAFO), with AFO1, and with AFO2 on his/her impaired (left) ankle. Before each AFO trial, the subjects were asked to walk with the AFO for 5 minutes to practice. For each trial, the subject was asked to walk for 6 eight-meter trips with the comfortable self-selected speed in the gait room at the University of Michigan Orthotic and Prosthetic Center (UMOPC). The first and last gaits of each trip were excluded during the analysis.

To quantitatively evaluate the patients' compensatory strategies for impairment. The maximum hip abduction and knee flexion angles during SW were calculated separately based on the thigh and shank IMUs via MATLAB (MathWorks, Natick, MA, USA). The data from the IMU attached to the impaired-side shank were processed by the proposed algorithm (Figures 3-2 and 3-3) implemented in MATLAB to estimate the initial conditions and lumped muscle parameters (Table 3-2) for each gait cycle. The paired t-test was used to determine the significant differences of gait parameters among conditions and between observed and predicted gait parameters.

Figure 3-5: IMU attachment for the LEGSys™: one IMU on each thigh, one on each shank, and one on the lower back trunk.

3.4. Results

3.4.1. Observed and Estimated Initial Joint Angles and Angular Velocities

Table 3-5 shows the shank pitch angles and angular velocities at the initial TO (t_0), HS (t_1), and end TO (t_2) that were predicted from the raw accelerations, angular velocities, and headings measured by the IMU on the impaired-side shank (Figure 3-2). These data were used as constraints in the optimization problem to search for the optimal, denoted as predicted hereafter, initial conditions and lumped muscle parameters for the observed gaits. The impaired-side shank pitch angles were significantly ($p < 0.05$) greater for AFO conditions comparing with NAFO condition at t_0 (60±9° versus 49±7°), t_1 (–7±4° versus –17±4°), and t_2 (61±8° versus 51±5°).

The comparisons of observed (O) and predicted (P) initial joint angles and angular velocities are shown in Table 3-6. Significant differences ($p < 0.05$) were found between the observed and predicted values for initial ankle angle and angular velocity for both subjects under the NAFO condition. Such differences were not found for the AFO conditions. For Subject 2, the

predicted angular velocity of the hip was significantly ($p < 0.05$) less than the observed value for all conditions.

Table 3-5: Summary of the estimated swing time, stance time, and shank pitch angles and angular velocities at TOs and HS for the impaired leg based on the IMU attached to the impaired-side shank.

Type	Variables	Subject 1			Subject 2		
		NAFO	AFO1	AFO2	NAFO	AFO1	AFO2
	n	33	24	26	24	30	22
Shank pitch angle (deg)	$\theta(t_0)$	50±5	67±7↑	67±6↑	43±9	54±11↑	53±5↑
	$\theta(t_1)$	−10±5	−3±4↑	−4±2↑	−23±3	−8±4↑↑	−13±4↑
	$\theta(t_2)$	50±5	68±7↑	67±6↑	51±5	55±11↑	53±5↑
Shank pitch angular velocity (deg/s)	$\dot{\theta}(t_0)$	166±7	159±36	138±33↓	236±21	216±33	288±22↑
	$\dot{\theta}(t_1)$	129±11	117±9↓	112±9↓	37±12	84±27↑↑	64±17↑
	$\dot{\theta}(t_2)$	166±7	159±36	138±33↓	167±8	216±43↑	288±22↑↑
Swing and stance time (s)	t_{SW}	0.47±0.07	0.46±0.01	0.44±0.03	0.47±0.11	0.47±0.03	0.46±0.09
	t_{ST}	0.74±0.01	0.73±0.03	0.76±0.03	0.73±0.01	0.73±0.03	0.77±0.03↑

↑ represents the value of the AFO condition was significantly ($p < 0.05$) greater than the NAFO condition
↑↑ represents the value of the AFO condition was significantly ($p < 0.05$) greater than the NAFO condition and the other AFO condition
↓ represents the value of the AFO condition was significantly ($p < 0.05$) smaller than the NAFO condition

Table 3-6: Comparison of initial impaired-leg hip and ankle joint angles and angular velocities between observed values (O) and predicted (P) values.

				Subject 1			Subject 2		
				NAFO	AFO1	AFO2	NAFO	AFO1	AFO2
			n	33	24	26	24	30	22
Initial impaired-leg joint angle (deg)	Hip	$\theta_{11}(t_0)$	O	−20±5	−26±8	−23±6	−19±4	−25±3	−16±4
			P	−28±3	−26±1	−22±1	−27±0.4	−26±2	−12±1
	Ankle	$\theta_{13}(t_0)$	O	21±6*	17±4	16±3	19±1*	11±4	17±6
			P	44±8*	6±21	15±10	40±5*	27±12	1±1
Initial impaired-leg joint angular velocity (deg)	Hip	$\dot{\theta}_{11}(t_0)$	O	160±13	167±9	162±13	48±7*	79±27*	70±26*
			P	128±16	120±23	110±12	100±14*	120±23*	100±25*
	Ankle	$\dot{\theta}_{13}(t_0)$	O	−387±19*	−393±9	−362±13	−271±27*	−314±27	−267±26
			P	−299±19*	−333±11	−374±20	−394±22*	−320±37	−290±19

* represents that the predicted value was significantly different from observed value based on paired t-test, $p < 0.05$

3.4.2. Estimated Lumped Muscle Parameters

The statistics of estimated lumped muscle parameters are shown in Table 3-7. For the impaired side during SW, the lumped muscle parameter of the impaired-side hip joint was significantly ($p < 0.05$) increased under the AFO1 condition comparing with the NAFO condition for both subjects (23±4 Nm/deg versus 17±4 Nm/deg). The lumped muscle parameter of the impaired-side hip joint during SW was significantly ($p < 0.05$) increased under the AFO2 condition comparing with the NAFO condition for Subject 1 (26±2 Nm/deg versus 18±2 Nm/deg) but was significantly ($p < 0.05$) decreased for Subject 2 (8±1 Nm/deg versus 13±6 Nm/deg).

The rest estimated lumped muscle parameters did not significantly change under both AFO conditions comparing with the NAFO condition for Subject 1. For Subject 2, the lumped muscle parameters of the unimpaired-side hip joint during SW were significantly ($p < 0.05$) decreased under the AFO2 condition comparing with the NAFO condition (12±5 Nm/deg versus 18±4 Nm/deg). The lumped muscle parameter of the unimpaired-side hip joint during DS was significantly ($p < 0.05$) increased under the AFO1 condition comparing with the NAFO condition (22±5 Nm/deg versus 10±5 Nm/deg). The impaired-side ankle torque was significantly ($p < 0.05$) decreased under the AFO2 condition comparing with the NAFO condition (0.94±0.16 Nm/kg versus 2.08±0.22 Nm/kg). The unimpaired-side ankle torques were significantly ($p < 0.05$) increased under the AFO1 condition comparing with the NAFO condition (2.07±0.10 Nm/kg versus 1.94±0.33 Nm/kg).

Table 3-7: Statistics of lumped muscle parameters of the hip and knee joints, k_{ijp}, in Nm/deg, and ankle joints, r_{i32}, in Nm/kg summarized in Table 3-2.

		Subject 1			Subject 2		
Type	Variable	NAFO	AFO1	AFO2	NAFO	AFO1	AFO2
	n	33	24	26	24	30	22
Impaired-side SW	k_{113}	18±2	26±3 ↑	26±2 ↑	13±6	20±4 ↑	8±1 ↓
	k_{123}	9±1	8±3	10±4	9±3	10±3	6±5
Impaired-side DS	k_{112}	6±4	4±2	5±3	10±2	15±2	6±5
	k_{122}	11±3	9±5	13±8	10±1	13±5	9±2
	r_{132}	1.77±0.20	1.77±0.23	1.69±0.28	2.08±0.22	1.95±0.25	0.94±0.16 ↓
Unimpaired-side SW	k_{213}	15±2	12±3	14±2	18±4	20±3	12±5 ↓
	k_{223}	9±6	13±3	12±1	10±3	11±3	7±8
Unimpaired-side DS	k_{212}	11±3	13±2	20±3	10±5	22±5 ↑	12±5
	k_{222}	17±3	15±1	14±1	20±2	15±3	18±8
	r_{232}	1.72±0.21	1.75±0.32	1.77±0.33	1.94±0.33	2.07±0.1 ↑	2.24±2.03

↑ represents the value of the AFO condition was significantly ($p < 0.05$) greater than the NAFO condition.
↑↑ represents the value of the AFO condition was significantly ($p < 0.05$) greater than the NAFO condition and the other AFO condition.
↓ represents the value of the AFO condition was significantly ($p < 0.05$) smaller than the NAFO condition.

3.4.3. Observed and Predicted Gait Parameters

A summary of the observed and predicted gait parameters (step lengths, maximum hip abduction, maximum knee flexion, phase time, and walking speed) is shown in Table 3-8. The RMSEs between observed and predicted unimpaired-side step length were all significantly ($p < 0.05$) greater than the RMSEs for impaired-side step length (RMSEs of 0.11 m versus 0.06 m). Besides, the predicted gait parameters all had significantly ($p < 0.05$) greater variations than observed gait parameters (standard deviations of 0.10 m versus 0.03 m). The observed and predicted SW time for the impaired side were the same because they were estimated based on the same algorithm. No significant differences were found between all observed and predicted gait parameters based on the paired t-test ($p < 0.05$).

Table 3-8: Summary of the observed (O) and predicted (P) gait parameters.

		Subject 1			Subject 2		
		NAFO	AFO1	AFO2	NAFO	AFO1	AFO2
	n	33	24	26	24	30	22
Impaired-leg step length (m)	O	0.68±0.03	0.78±0.03	0.75±0.03	0.35±0.03	0.44±0.02	0.38±0.04
	P	0.66±0.13	0.81±0.12	0.74±0.16	0.31±0.07	0.40±0.14	0.36±0.07
	RMSE	0.04	0.08	0.06	0.02	0.07	0.09
Unimpaired-leg step length (m)	O	0.48±0.03	0.47±0.02	0.45±0.02	0.46±0.03	0.54±0.03	0.48±0.03
	P	0.49±0.03	0.48±0.09	0.48±0.09	0.51±0.12	0.55±0.15	0.42±0.05
	RMSE	0.05	0.09	0.09	0.09	0.20	0.13
Max impaired-leg hip abduction	O	7±3	5±4	5±4	15±8	10±2	12±3
Max impaired-leg knee flexion	O	66±3	63±3	61±2	53±7	60±4	60±5
	P	64±7	64±4	62±10	60±4	57±3	62±12
t_{SW}/T (%)	O (P)	38±6	36±10	37±2	46±5	39±4	42±2
t_{DS1}/T (%)	O	13±2	10±3	11±1	6±3	11±2	10±1
	P	15±3	10±5	11±2	7±3	12±5	11±2
t_{SS}/T (%)	O	33±5	35±9	37±1	35±2	33±1	32±1
	P	32±7	34±11	40±6	34±17	32±12	33±9
t_{DS2}/T (%)	O	16±3	19±3	15±3	13±4	17±4	16±2
	P	15±3	20±7	12±2	14±5	18±7	16±5
Walking speed (m/s)	O	0.93±0.15	0.98±0.25	1.00±0.04	0.67±0.05	0.81±0.04	0.7±0.05
	P	0.92±0.13	1.03±0.22	1.02±0.16	0.68±0.12	0.77±0.15	0.73±0.06

* t_{SW} is the duration of the SW of the impaired side, t_{DS1} is the duration of the DS with the impaired side in front, t_{SS} is the duration of the SS of the impaired side, t_{DS2} is the duration of the DS with the impaired side behind, and T is the duration of the whole gait that equal to the sum of t_{SW}, t_{DS1}, t_{SS}, and t_{DS2}.

The step length of the impaired side was significantly ($p < 0.05$) longer than the unimpaired side for Subject 1. Contrarily, the step length of the impaired side was significantly ($p < 0.05$) shorter than the unimpaired side for Subject 2. Comparing with the NAFO condition, the impaired step length was significantly ($p < 0.05$) longer under both AFO conditions for both subjects, and the unimpaired step length was significantly ($p < 0.05$) shorter under both AFO conditions for Subject 1, but longer under the AFO1 condition for Subject 2.

The observed maximum hip abduction angles were significantly ($p < 0.05$) higher for Subject 2 than Subject 1 (12±7° versus 6±4°). Comparing with the NAFO condition, the impaired-side hip abduction was significantly ($p < 0.05$) decreased under both AFO conditions

for both subjects (8±4° versus 11±5°). Both observed and predicted impaired-side maximum knee flexion was significantly ($p < 0.05$) higher for Subject 1 than for Subject 2 under NAFO condition (63±7° versus 59±6°). Comparing with the NAFO condition, the maximum impaired-side knee flexion was significantly ($p < 0.05$) decreased under both AFO conditions for Subject 1 (63±5° versus 65±7°) but significantly ($p < 0.05$) increased under both AFO conditions for Subject 2 (60±9° versus 57±5°).

The swing time of the impaired side was significantly ($p < 0.05$) shorter for Subject 1 than for Subject 2 (36% versus 43% of gait duration). Comparing with the NAFO condition, the swing time was significantly ($p < 0.05$) decreased under both AFO conditions for Subject 2 (41% versus 46% of gait duration), but not significantly changed under both AFO conditions for Subject 1.

3.4.4. Gait Symmetry and Efficiency for Evaluation

The observed and predicted SIs for step length are shown in Figure 3-6. Comparing with the NAFO condition, the SI significantly ($p < 0.05$) increased under both AFO conditions for Subject 1 (50% versus 34%) but significantly ($p < 0.05$) decreased under both AFO conditions for Subject 2 (22% versus 28%). This trend was consistent between observed and predicted values.

The SIs under both AFO conditions were not consistent between observed and predicted values. In between the AFO conditions for Subject 1, the observed SI was equal under both AFO conditions, but the predicted SI was significantly ($p < 0.05$) lower under the AFO2 condition than under the AFO1 condition (41% versus 51%). In between the AFO conditions for Subject 2, the observed SI was significantly ($p < 0.05$) less under the AFO1 condition (20% versus 24%),

but the predicted SI was significantly ($p < 0.05$) greater under the AFO1 condition (31% versus 26%).

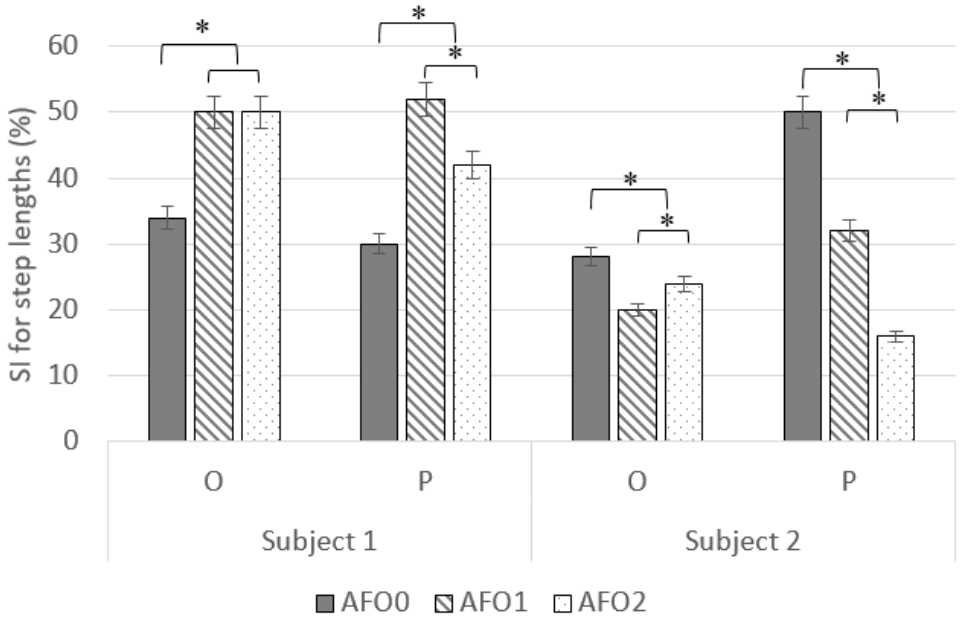

Figure 3-6: Observed and predicted SI under all conditions based on mean step lengths. Values are mean ± SE.

The observed and predicted SIs for swing time are shown in Figure 3-7. Comparing with the NAFO condition, the SI significantly ($p < 0.05$) decreased under both AFO conditions (4% versus 15%) for both subjects except that the observed SI with AFO 2 condition for Subject 2 was equal to the observed SI under the NAFO condition. This trend was overall consistent between observed and predicted values. The SI changing trend under both AFO conditions was consistent between observed and predicted for Subject 2, but was inconsistent for Subject 1. In between the AFO conditions for Subject 1, the observed SI was significantly ($p < 0.05$) greater under the AFO1 condition (3% versus 0%), but the predicted SI was significantly ($p < 0.05$) less under the AFO1 condition (6% versus 8%). In between the AFO conditions for Subject 2, the observed and predicted SI was significantly ($p < 0.05$) less under the AFO1 condition (22% versus 29%).

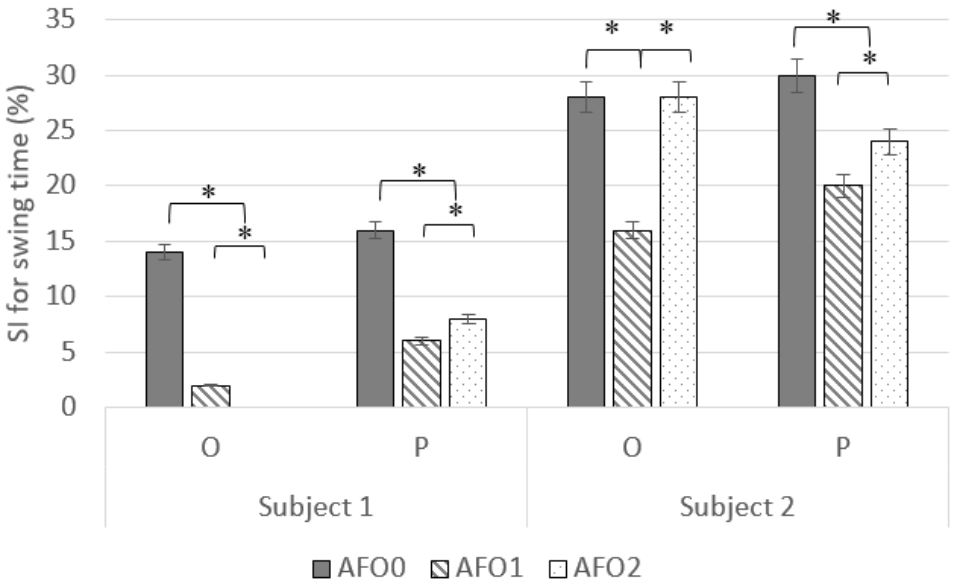

Figure 3-7: Observed and predicted SI under all conditions based on mean swing time. Values are mean ± SE.

The observed and predicted preferred walking speed are shown in Figure 3-8 and Table 3-8. The walking speed was significantly ($p < 0.05$) faster for Subject 1 than for Subject 2 (0.98± 0.19 m/s versus 0.73±0.12 m/s). Comparing with the NAFO condition, the walking speed was significantly ($p < 0.05$) increased under both AFO conditions for both subjects (0.88±0.18 m/s versus 0.80±0.11 m/s). This trend was consistent between observed and predicted values. The walking speed under both AFO conditions was consistent between observed and predicted values. The walking speed was not significantly different between the AFO conditions.

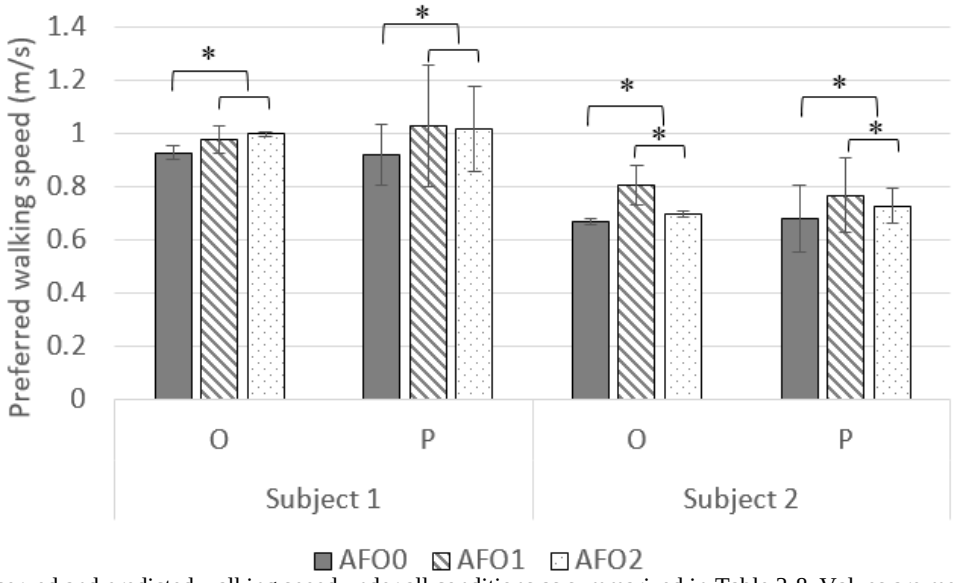

Figure 3-8: Observed and predicted walking speed under all conditions as summarized in Table 3-8. Values are mean ± SE.

The predicted energy expenditure for each condition is shown in Figure 3-9. The NAFO condition had significantly ($p < 0.05$) lower energy expenditure comparing with the AFO conditions for both subjects (89 J/gait versus 133 J/gait), while the AFO2 condition had significantly ($p < 0.05$) higher energy expenditure comparing with the other two conditions for both subjects (143 J/gait versus 105 J/gait).

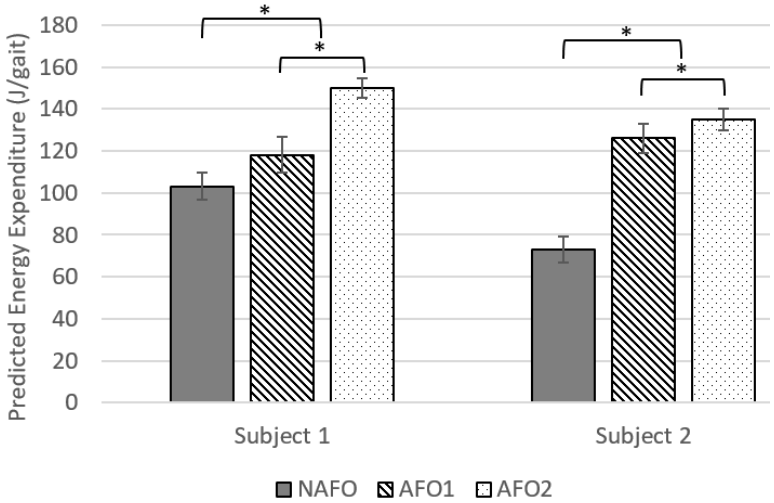

Figure 3-9: Predicted energy expenditure under all conditions. Values are mean ± SE.

3.5. Discussion

3.5.1. Initial Joint Angles and Angular Velocities Differences

Most of the observed and predicted values were within the normal range from the literature review in Table 2-4 except the observed initial hip angular velocity for Subject 2 was 30% less than the normal range (Table 3-6). This implied the slowed gait that resulted from the impairment [100–103]. The differences between observed and predicted initial ankle angles (RMSE = 17°) and angular velocities (RMSE = 52 deg/s) might due to the forefoot stiffness created by the shoe. Several studies showed that the forefoot stiffness created by the shoe affected gait performance [121,122]. While the proposed model considered the forefoot as a rigid link and resulted in a biased initial ankle angle. For both AFO conditions, the AFO footplate was more rigid than the shoe. This made gait with AFOs similar to the gait predicted by the PPCLMP model and explained that no significant differences were found for ankle angle and angular velocities between observed and predicted values under AFO conditions.

3.5.2. Estimated Lumped Muscle Parameters

The lumped muscle parameters of hip and ankle joints were significantly changed among different conditions, while the lumped muscle parameters of knee joints were not significantly changed among the AFO conditions.

The increment of impaired-side hip lumped muscle parameter with AFO1 during SW for two subjects (23±4 Nm/deg versus 17±4 Nm/deg) and the inconsistency changing trend with AFO2 during SW between two subjects (Table 3-7) can be explained by the two AFO effects during DS addressed in Chapter 2. The AFO released energy during push-off, but also constrained the ankle from performing plantar flexion during the later push-off stage, which

constrained the ability of energy generation. The AFO1 had less stiffness and released less energy for initial SW. This resulted in higher hip muscle activity to pull the leg forward during SW to compensate for less energy at the beginning. On the other hand, the AFO2 had higher stiffness and released more energy for initial SW. Depends on which effect (release energy and constrain the ankle) was dominating, the hip lumped muscle parameter could increase or decrease during SW.

The decrement of the unimpaired-side ankle torque for Subject 2 with AFO2 (Table 3-7, 0.94±0.16 Nm/kg versus 2.08±0.22 Nm/kg) was because AFO2 was stiffer and released more energy. The increment of unimpaired-side ankle torque for Subject 2 with AFO1 (2.07±0.10 Nm/kg versus 1.94±0.33 Nm/kg) was a result of compensating for the constrain-ankle effect of the AFO during SS. During the DS with unimpaired side behind, the subject might want to push-off harder to maintain higher initial velocities of the impaired side at initial SS that right after the DS to compensate the slowing effect of the AFO stiffness proposed in Chapter 2. The inconsistency trend in lumped muscle parameters changing between subjects might due to gender, anthropometry, and gait preference differences. Further investigation is needed to study how these factors could affect lumped muscle parameters and model predictions.

3.5.3. Gait Parameters

Overall, the PPCLMP model predictions of gait parameters were improved by utilizing the IMU data comparing with results in Chapter 2 (RMSE of step length: 0.07 m versus 0.15 m; RMSE of swing time: 2% versus 5% of gait duration). The RMSE of step lengths ranged from 0.02 to 0.20 m. The RMSE was resulted from the higher variations found in the predicted step length comparing with the observed step length (Table 3-8). The differences between the mean observed and predicted step lengths were all less than 0.05 m. This suggested that the model was good in predicting multiple gait cycles instead of the individual gait cycle. The higher RMSE of the unimpaired-side step length suggested that the prediction of step length on the impaired side was better than the prediction of the unimpaired side. This was because the IMU was attached to the impaired side. There was more information provided for the impaired side from the IMU.

The movement of the unimpaired side was only based on model prediction. The impaired-side step length (Table 3-8) was changing in the same direction with the impaired-side hip joint lumped muscle parameter (Table 3-7), which was consistent with the sensitivity analysis shown in

Table 3-3. For both subjects, the AFO made the impaired-side step length longer and was inconsistently affect the step length on the unimpaired side. This was consistent with the finds reported by previous investigations of AFO effects on impaired gait [123–125].

Subject 1 had a longer step length on the impaired side than on the unimpaired side (0.74 ±0.18 m versus 0.47±0.07 m), while Subject 2 had longer step length on the unimpaired side (0.49±0.03 m versus 0.39±0.03 m). This could be explained by the two compensatory strategies described by Konttink et al. [5] and Don et al. [8]. As observed, Subject 1 tended to use more knee flexion (Table 3-8, 63±7° versus 59±6°) on the impaired side to lift his foot during SW in order to avoid stubbing his toe. Because of more knee flexion, the HS occurred later and further away from the stance leg, which led to longer step length. On the other hand, Subject 2 tended to utilize more hip abduction (Table 3-8, 12±7° versus 6±4°) and perform the circumduction movement of the leg on the side of the body. This resulted in longer SW time (Table 3-8) and shorter step length. The differences in compensatory strategies between the two subjects might be due to the differences in gait patterns between males and females. Females have been found to have more hip abduction and internal rotation due to wider pelvis and less effective hip abductors during walking [126,127].

The prediction of step length was better for Subject 1 than Subject 2 (RMSE < 0.09 versus RMSE < 0.20 m). This is because the significant hip abduction performed by Subject 2 during gait was not characterized by the planar model. Possible solutions are adding one degree of freedom to the hip joint (abduction/adduction) to advance the model into a 3-D model, or compensating the 3-D movement in the planar model by changing the effective lengths of the body segments in the sagittal plane.

The walking speed was overall faster with AFO conditions comparing with the NAFO condition (0.88±0.18 m/s versus 0.80±0.11 m/s), which suggested that AFOs could improve walking speed. This was consistent with the findings reported by previous investigations of AFO effects on impaired gait [123–125].

3.5.4. Evaluation of Gait with AFOs

The IMU-attached AFO shows the possibility of evaluating gait with AFOs during the patient's daily activity. The IMU data can be stored locally or uploaded to a server via Wi-Fi for indoor or 2G-5G for outdoor connection for gait analysis and evaluation regarding gait symmetry and efficiency.

The observed SI for step length (Figure 3-6) suggested that Subject 1 had worse spatial symmetry in his gait with the AFOs (SI for step length: 50% versus 34%), and Subject 2 had better spatial symmetry in her gait with the AFOs comparing with the NAFO condition (SI for step length: 22% versus 28%). This was because that Subject 1 had longer step lengths on his impaired side, while Subject 2 had shorter step lengths on her unimpaired side under the NAFO condition. Since the AFOs increased the step lengths on the impaired side, it was reasonable to see Subject 1 got worse gait with the AFOs, and Subject 2 got better gait with the AFOs based on the SI for step length. This suggested that patients with longer impaired-side step length (compensate by flexing knee) would get even more asymmetry on step lengths, while patients with shorter impaired-side step length (compensate by circumduction) would gain more symmetry on step lengths by wearing AFO. Neither AFOs could correct the SI for step length to normal range (0~10%, [67,68]), which was consistent with the findings from Guillebastre et al. [128] and Esposito [40].

Due to the better prediction of impaired-side step length (RMSE < 0.09 m) and poor unimpaired-side step length (RMSE < 0.20 m) mentioned above, the model did not demonstrate good prediction on the SI for step length. Especially for Subject 2, the model prediction would suggest AFO2 was better than AFO1, while the observed step lengths would suggest the other way around. Also, the RMSE of step length prediction for Subject 1 was less than 0.09 m compared with 0.20 m for Subject 2. This inconsistency of the step length prediction accuracy between the two subjects might be the result of differences in stature, gender, and age of two subjects. Females were found to have a wider pelvis and more pelvic obliquity range than males during gait [129,130], while the linkage system of the PPCLMP model ignores the size and movements of the pelvis link during gait. This may contribute to the prediction errors when predicting gait for females. Further investigation is needed to evaluate the effect of these anthropometric parameters on model prediction accuracy.

Overall, the SI for swing time (Figure 3-7) suggested that drop foot patients would gain more temporal symmetry with the AFOs (4% versus 15%). For Subject 2, the model prediction was consistent with the observation results: AFO1 was better. For Subject 1, the model prediction suggested AFO1, while the observed results suggested AFO2. However, both AFOs corrected the SI for swing time of Subject 1 back to normal range (0~9%, [67,68]) and might be good options for Subject 1. Thus, the model had consistent results in evaluating the gait with AFO1 and AFO2 with the observed results on SI for swing time.

Similarly, the model had consistent results in evaluating the gait with AFO1 and AFO2 with the observed results on walking speed (Figure 3-8). Based on the walking speed, AFO1 and AFO2 were equivalent in improving Subject 1's gait, while the AFO1 showed better gait improvement on Subject 2 than the AFO2.

The predicted energy expenditure was increasing under the AFO conditions comparing with the NAFO condition (Figure 3-9, 89 J/gait versus 133 J/gait). This was inconsistent with the observed reduction in oxygen consumption with AFO use reported by many investigators [96,131–133]. Hassler [134] proposed that the possible reason for oxygen consumption reduction was stability improvement. The proposed model did not consider the stability of the movement, since the model characterized the lower limb movement of each phase with continuous dynamic systems that describe smooth movements. The lateral stability was also not considered due to the limitation of the planar analysis. Furthermore, the model estimated the energy expenditure based on the lumped muscle works at each joint. The model did not separate the passive stiffness of joints from the active muscle activities, neither the work from agonist and antagonist. For instance, the two subjects in this study suffered from drop foot due to spastic hemiparesis. This pathology resulted in the involuntary contraction of the ankle plantar flexor [135,136], whose passive work was included in the energy expenditure of this study. The model also assumed the knee was straight during SS, and the front-knee was straight during DS. The energy needed to keep the knee straight was not considered in the model.

3.5.5. Limitations

As discussed, the model was limited to predicting energy expenditure because the work of agonist and antagonist, the smoothness of movement, and lateral movements were not characterized by the model. In addition, using the minimization of energy expenditure as the objective of the optimization problem was a major limitation. The optimization strategies of subjects during walking may not be limited to minimize energy expenditure, but also comfort and movement smoothness. Also, only two subjects were recruited in this study, which limits the statistical power of the results.

3.6. Conclusions

This work demonstrated how the model could be used to quantitatively predict and evaluate gait with different ankle stiffnesses based on the data from a single IMU attached to the impaired shank. Results showed that the IMU could be utilized to estimate the initial conditions and lumped muscle parameters for each gait cycle by the inverse-dynamic mode of the PPCLMP model. The estimated initial conditions and lumped muscle parameters can be used by the forward-dynamic mode of the model to enhance the gait prediction and evaluation. The model-predicted step lengths, swing time, and walking speed were consistent with the observed gait parameters, and the prediction accuracy was improved comparing with results in Chapter 2. The model-predicted SI for swing time was consistent with the observed SI, while the model-predicted SI for step length was inconsistent with the observed SI among different conditions. The model-predicted energy expenditure was not a good quality metric for gait evaluation because the model ignored the amount of energy needed to perform stable and smooth movements.

CHAPTER 4 An Investigation of Gait Prediction Accuracy of the PPCLMP Model

Abstract

This study aims to investigate the gait prediction accuracy of the planar piecewise continuous lumped muscle parameter (PPCLMP) model. Three male (13^{th} to 96^{th} percentile stature) and three female (22^{th} to 97^{th} percentile stature) healthy subjects were recruited to walk with and without two ankle-foot orthoses (AFOs) with low and high stiffnesses (3.4 and 6.9 Nm/deg) on their left ankles to measure their step lengths and swing time during gait using the vision-based motion tracking system. The kinematic data measured from the inertial measurement unit (IMU) attached to the AFO calf were utilized by the inverse-dynamic mode of the PPCLMP model to predict the initial conditions and lumped muscle parameters that characterize joint torques. The predicted initial conditions and lumped muscle parameters were then utilized by the forward-dynamic mode of the PPCLMP model for gait prediction. Additionally, the electrical activities of muscles related to hip joint torques were measured by four surface electromyogram (SEMG) units: one on the biceps femoris and one on the rectus femoris of each thigh. The model-predicted initial conditions and lumped muscle parameters were compared with the experimentally measured initial conditions and SEMG profiles, respectively. The model-predicted step lengths and swing time were also compared with the experimental observations. Results demonstrated that the increasing stature significantly ($p < 0.05$) improved the model prediction accuracy regarding the initial conditions and lumped muscle parameters while body mass and gender had no significant effect. Consequently, the increasing stature was found to significantly

($p < 0.05$) improve the model prediction accuracy of step lengths, as well as the walking speed and symmetry index for step length.

4.1. Introduction

Gait-related biomechanical models utilize anthropometric parameters (stature, body mass, and gender) to characterize the linkage system of the human body and investigate movements during gait phases [137–140]. The inverted pendulum model for the single stance phase (SS) demonstrated that the stature and body mass distribution determined the energy transfer during the SS [141]. The inverted pendulum model for the SS [141] and the double pendulum model for the swing phase (SW) [142] revealed that the stature (particularly the lower limb lengths) but not body mass affected the swing time and stance time ratio for walking gait. Further, various stature, body mass, and gender affected the prediction of joint forces and movements from the kinematic chain model [140,143] which was used to characterize the lower limb movements during the double stance phase (DS) of walking.

Anthropometric parameters also affect the gait prediction of the planar piecewise continuous lumped muscle parameter (PPCLMP) model (Chapters 2 and 3), which combines the SS (inverted pendulum model), SW (double pendulum model), and DS (kinematic chain model) to predict the walking gait with an ankle-foot orthosis (AFO) that increases the ankle joint stiffness. The data from an inertial measurement unit (IMU) attached to the AFO are utilized by the inverse-dynamic mode of the PPCLMP model to predict the initial conditions (joint angles and angular velocities at the start of gait) and lumped muscle parameters that characterize joint torques for each gait cycle (Chapter 3). The predicted initial conditions and lumped muscle parameters are then utilized by the forward-dynamic mode of the PPCLMP model to predict gait parameters (step lengths and swing time) for gait evaluation. Anthropometry of subjects affects the model prediction accuracy. The PPCLMP model prediction accuracy of step lengths was better for a tall male subject than for a short female subject (root mean square error (RMSE) <

0.09 m versus RMSE < 0.20 m) in Chapter 3. The goal of this study is to investigate the PPCLMP model prediction accuracy among subjects with various anthropometry.

Human subject tests of various anthropometry are required to evaluate the prediction accuracy of biomechanical models [144–146]. Muscle electrical activity measured from surface electromyogram (SEMG) units can be used to estimate the muscle force [64,147–149] which is characterized as spring force by the lumped muscle parameters in the PPCLMP model. As biceps femoris (BF) acting as the knee flexor and hip extensor and rectus femoris (RF) acting as the knee extensor and hip flexor, SEMG signals of the BF and RF are commonly used to estimate the hip extension and flexion torques, since they determine the lower limb movements during each gait phase. The root mean square (RMS) of the SEMG profile for the BF mostly peaked during the SW [150,151], while the RF of the back-leg was found to significantly active during the DS [152–154].

To examine the prediction accuracy of the PPCLMP model, subjects of various stature, body mass, and gender were recruited in this study to compare the SEMG measured muscle activities and the model-predicted lumped muscle parameters as well as the observed and model-predicted: 1) initial conditions of each gait cycle, 2) step lengths, 3) swing time, 4) symmetry index (SI) for step length, 5) SI for swing time, and 6) walking speed.

This study investigates the PPCLMP model prediction accuracy among various anthropometry. The hypothesis is that the anthropometric inputs affect the model prediction accuracy. Section 4.2 outlines the subject recruitment, experiment procedure, data collection and processing, and statistical analysis. Section 4.3 compares the model prediction accuracy among subjects of various anthropometry. Section 4.4 discusses the effect of anthropometry on model

prediction accuracy and explains the effect of subject variables on PPCLMP model prediction accuracy.

4.2. Methods

The subjects, the procedure of the human subject test, experimental settings, data processing, and the statistical analysis that examines the effect of anthropometry on model prediction accuracy are summarized.

4.2.1. Subjects

Three male and three female healthy subjects were recruited to measure their muscle activities, joint angles, step lengths, and swing time during walking gait. The gender, stature, percentile of stature, body mass, and body mass index (BMI) of six subjects are listed in Table 4-1. The stature of female subjects ranged from 22^{th} to 97^{th} percentile of the female population, and the stature of male subjects ranged from 13^{th} to 96^{th} percentile of the male population reported in the ANSUR Data [53].

Table 4-1: Anthropometry of six subjects

Subject	1	2	3	4	5	6
Gender*	F	F	F	M	M	M
Stature (m)	1.55	1.61	1.74	1.65	1.75	1.88
Percentile of stature	22^{th}	55^{th}	97^{th}	13^{th}	55^{th}	96^{th}
Body mass (kg)	50	56	56	68	85	95
BMI	21	22	18	25	28	27

*F represents the female and M represents the male.

4.2.2. Procedure

Three experimental conditions were carried out. In the first condition, the subjects walked without any AFO, denoted as NAFO. In the second and third conditions, the subjects wore an AFO with low (3.4 Nm/deg, as tested in Appendix C) or high stiffnesses (6.9 Nm/deg, as tested in Appendix C) on their left ankle and denoted as AFO1 and AFO2, respectively. To gain data of

40 gait cycles from each subject under each condition (NAFO, AFO1, and AFO2), the subject was asked to walk with comfortable self-selected speed for 20 trips under each condition with at least two complete gait cycles recorded (exclude the first and last gait cycles) for each trip. For AFO1 and AFO2 conditions, each subject was asked to walk with the AFO for 5 minutes before the experiment trial to adapt to the increased stiffness at the ankle joint. Before participation, the goal, experimental procedure, and possible risks were explained to each subject. An informed consent form approved by Institutional Review Boards (IRB) of the University of Michigan (HUM00090458) was signed by each subject before participation.

4.2.3. Data Collection

Three measurement devices were applied simultaneously to record the lower limb movement and muscle activity data: 1) vision-based motion tracking system, 2) IMU attached to the left shank or AFO, and 3) SEMG on BF and RF muscles.

The vision-based motion tracking system with two sensor units (three cameras each) by NDI Optotrak Certus (NDI Waterloo, Ontario, Canada) was used to measure the movements of lower limbs at a sampling rate of 100 Hz. As shown in Figure 4-1(a), six marker clusters were placed on the upper leg, lower leg, and foot of both legs to track the movement of lower limb segments in the sagittal plane. Additional markers were placed on the hip and ankle joints for calibration purposes.

An IMU (Model BNO055, Bosch Sensortec, Mount Prospect, Illinois, USA) was attached to the back of the left lower shank for the NAFO condition and the AFO for AFO1 and AFO2 conditions as shown in Figure 4-1(b), to measure the shank movement at a sampling rate of 100 Hz.

Custom SEMG units with RMS filter (University of Michigan Center for Ergonomics, Ann Arbor, Michigan, USA) were utilized to predict the muscle activities to compare to the model prediction of the lumped muscle parameters. As shown in Figure 4-1(c), four SEMG units were instrumented on: 1) left biceps femoris (lBF), 2) left rectus femoris (lRF), 3) right biceps femoris (rBF), and 4) right rectus femoris (rRF) [150–154] to measure the electrical activities of the hip extensors and flexors. Recorded SEMG signals were processed by the RMS filter with the gain set to 10,000 and the delay set to 250 ms. The SEMG RMS data were synchronized with the vision-based motion tracking system using the NDI data acquisition unit (NDI Waterloo, Ontario, Canada).

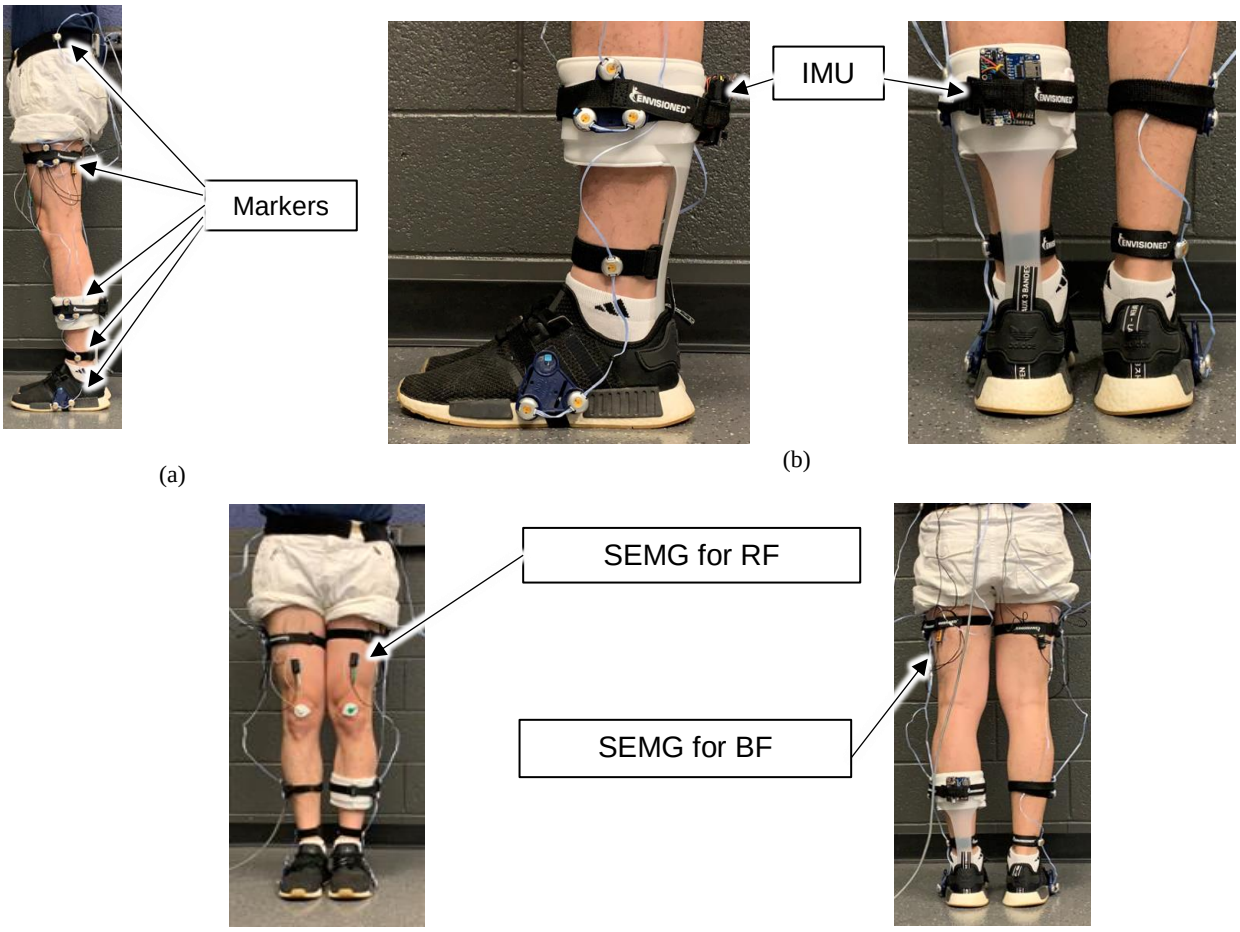

(a) (b) (c)

Figure 4-1: Equipment for measuring movements and muscle activities of the BF and RF: (a) the placement of vision-based motion tracking markers from the side view, (b) the IMU attached to the back of the AFO calf, and (c) the placement of four SEMG units on lBF, lRF, rBF, and rRF.

4.2.4. Data Processing

The data measured from the vision-based motion tracking system were utilized to calculate the initial conditions, step lengths, swing time, and walking speed of each gait cycle using MATLAB 2017 (MathWorks, Natick, MA, USA). The amplified SEMG RMS data of each muscle during one sample gait cycle is shown in Figure 4-2. Because each lumped muscle parameter has only one value for each phase, the mean SEMG RMS of each phase was calculated to compare with the hip joint lumped muscle parameters regarding changing trends. The three-axis accelerations, angular velocities, and headings measured from the IMU were

analyzed by the inverse-dynamic mode of the PPCLMP model to predict the initial conditions and lumped muscle parameters (Figures 3-2 and 3-3). The predicted initial conditions and lumped muscle parameters were then used in the forward-dynamics mode of the PPCLMP model to predict the step lengths, swing time, and walking speed of the gait to compare with experimental observations.

Differences between the observed and PPCLMP model-predicted initial conditions were calculated to study the model prediction accuracy of the initial conditions. Correlations between the mean of SEMG RMS and PPCLMP model-predicted hip joint lumped muscle parameters for the swing leg during the SW and the back-leg during the DS were used to investigate the model prediction accuracy of the lumped muscle parameters. Differences between the observed and predicted step lengths and swing time were used to examine the model prediction accuracy of gait parameters.

Phase		Associated lumped muscle parameter	Left SW	DS1 (right leg behind)	Right SW	DS2 (left leg behind)
Mean SEMG RMS (mV)	lBF	Left hip	34±12	16±2	14±11	63±9
	lRF	Left hip	19±5	18±6	11±10	35±3
	rBF	Right hip	14±10	47±5	28±6	18±3
	rRF	Right hip	3±3	52±20	36±10	6±1

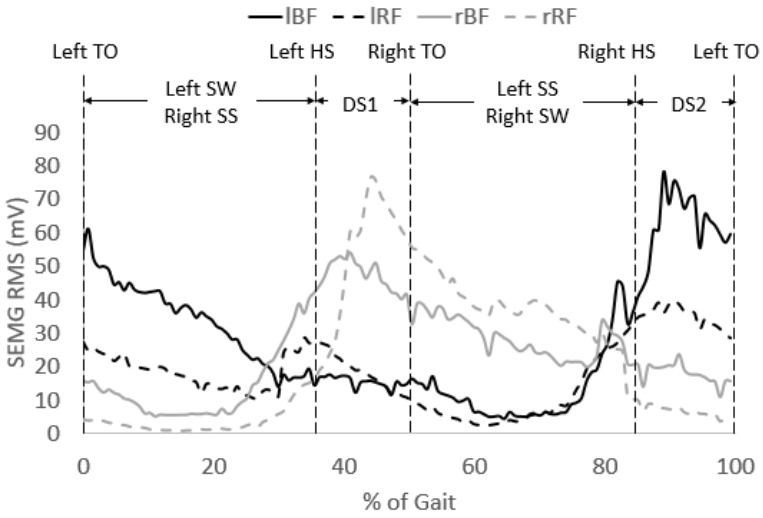

Figure 4-2: Amplified SEMG RMS during a sample gait of Subject 3 under the NAFO condition. TO represents the toe-off, HS represents the heel strike, SW represents the swing phase, SS represents the single stance phase, DS1 represents the doubles stance phase with right leg behind, and DS2 represents the double stance phase with left leg behind, lBF represents the left biceps femoris, lRF represents the left rectus femoris, rBF represents the right biceps femoris, and rRF represents the right rectus femoris. The top table shows the mean and standard deviation of the SEMG RMS during each phase that are used to compare with the associated lumped muscle parameters.

To further examine the effect of anthropometry, the walking speed and SIs (Eq. 3-1, [66]) for step length and swing time were calculated for each subject for NAFO, AFO1, and AFO2 conditions based on observed and predicted gait parameters. Differences between the observed and predicted walking speed and SIs were also used to determine the prediction accuracy of the PPCLMP model.

4.2.5. Statistical Analysis

Seven dependent variables were used in this study to evaluate the model prediction accuracy: 1) the correlation (denoted as r_{EMG}) between the mean SEMG RMS and predicted lumped muscle parameters of the SW and DS, as well as the error of predicted: 2) initial conditions (denoted as ε_{IC}) including initial joint angles (initial shank pitch angle $\theta(t_0)$, back-hip

angle $\theta_{11}(t_0)$, and back-ankle angle $\theta_{13}(t_0)$) and angular velocities (initial shank pitch angular velocity $\dot{\theta}(t_0)$, back-hip angular velocity $\dot{\theta}_{11}(t_0)$, and back-ankle angular velocity $\dot{\theta}_{13}(t_0)$), 3) step lengths (denoted as ε_{SL}), 4) swing time (denoted as ε_{TSW}), 5) walking speed (denoted as ε_{SP}), 6) SI for step length (denoted as ε_{ISL}), and 7) predicted SI for swing time (denoted as ε_{SITSW}).

These errors were defined as the absolute differences between the observed and predicted values. The independent variables of this study were stature, body mass, gender, and AFO stiffness.

Repeated measures analysis of variance (ANOVA) was performed using Minitab 18 (Minitab LLC, Chicago, IL, USA) to evaluate the effects of four independent variables (stature, body mass, gender, and AFO stiffness) and their interaction terms on the dependent variables. Subjects' stature and body mass were used as covariates. Additional correlation analysis was performed to further test the relations between the independent variables and the ANOVA-significant ($p < 0.05$) affected dependent variables. As suggested by Evans [155], for the absolute value of *r*:

- 0.00 – 0.19, "very weak"
- 0.20 – 0.39, "weak"
- 0.40 – 0.59, "moderate"
- 0.60 – 0.79, "strong"
- 0.80 – 1.00, "very strong"

4.3. Results

The model prediction accuracy of initial conditions, lumped muscle parameters, step lengths, swing time, gait symmetry, and walking speed are presented.

4.3.1. RMSE between Observed and Predicted Results

Results of observed and predicted initial joint angles and angular velocities (Appendix D), measured SEMG RMS, the model-predicted hip and knee lumped muscle parameters during the SW and DS (Appendix E), and observed and predicted step lengths, swing time, and walking speeds (Appendix F) for 40 normal self-paced gait cycles are presented. The RMSE in predicted initial joint angles and angular velocities ranged from 0 to 18° and 2 to 58 °/s, respectively. The RMSE in predicted step lengths and swing time ranged from 0.01 to 0.16 m and 0.01 to 0.04 seconds, respectively. The model prediction accuracy was good for swing time and fair for step length.

4.3.2. ANOVA

As the ANOVA results shown in Table 4-2, the stature and gender have significant effects on the model prediction accuracy. The stature had significant effects ($p < 0.05$) on all the dependent variables except the ε_{IC} of the initial back-ankle angle, the ε_{TSW} of both sides, and ε_{SITSW}. Gender showed significant effects on the r_{EMG} of lBF ($r = 0.79$ for male versus $r = 0.40$ for female) and rRF ($r = 0.63$ for male versus $r = 0.32$ for female) during SW and rBF ($r = 0.73$ for male versus $r = 0.44$ for female), lRF ($r = 0.81$ for male versus $r = 0.33$ for female), and rRF ($r = 0.87$ for male versus $r = 0.61$ for female) during DS.

The body mass, AFO stiffness, and the interaction terms between the independent variables did not have significant effects on any of the dependent variables.

Table 4-2: ANOVA table for independent variables with significant effects ($p < 0.05$). L represents the left side, R represents the right side, M represents the male, and F represents the female. The significant effect of gender is shown as pooled value comparisons between males and females. The significant effect of stature is shown as the first-order coefficient and the intercept from ANOVA. The body mass and the interaction terms had no significant effect on the dependent variables.

	ε_{IC}						r_{EMG}								ε_{SL} (m)		ε_{TSW} (s)		ε_{SP}	ε_{SISL}	ε_{SITSW}
							SW				DS										
	$\theta(t_0)$ (°)	$\theta_{11}(t_0)$ (°)	$\theta_{13}(t_0)$ (°)	$\dot{\theta}(t_0)$ (°/s)	$\dot{\theta}_{11}(t_0)$ (°/s)	$\dot{\theta}_{13}(t_0)$ (°/s)	lBF	lRF	rBF	rRF	lBF	lRF	rBF	rRF	L (AFO)	R	L (AFO)	R	(m/s)	(%)	(%)
Gender (M vs. F)							0.79±0.08 vs. 0.40±0.04			0.63±0.06 vs. 0.32±0.14		0.81±0.06 vs. 0.33±0.01	0.73±0.12 vs. 0.44±0.10	0.87±0.02 vs. 0.61±0.21							
Stature (m) coefficient (intercept)	–26 (54)	–16 (34)		–65 (129)	–66 (136)	–51 (105)	1.3 (–1.6)	0.9 (–1.1)	0.5 (–0.3)	1.1 (–1.4)	0.9 (–1.1)	1.4 (–1.8)	1.3 (–1.7)	1.4 (–1.6)	–0.24 (0.49)	–0.33 (0.66)			–0.24 (0.52)	–37 (72)	

4.3.3. Accuracy of Initial Conditions

The model prediction accuracy of initial conditions (ε_{IC}) was correlated with stature as shown in Table 4-3. Weak to strong negative correlations (r = –0.61 to –0.21) were found between stature and the ε_{IC} of all initial angles and angular velocities.

Table 4-3: The correlation coefficients between the stature and ε_{IC} of initial angles and angular velocities. The ε_{IC} of all initial angles and angular velocities were ANOVA-significant ($p < 0.05$) affected by stature except the ε_{IC} of the initial back-ankle angle ($\theta_{13}(t_0)$).

		Correlation between stature and ε_{IC}
Shank pitch angle	$\theta(t_0)$	–0.81
Back-hip angle	$\theta_{11}(t_0)$	–0.60
Back-ankle angle	$\theta_{13}(t_0)$	–0.51
Shank pitch angular velocity	$\dot{\theta}(t_0)$	–0.37
Back-hip angular velocity	$\dot{\theta}_{11}(t_0)$	–0.35
Back-ankle angular velocity	$\dot{\theta}_{13}(t_0)$	–0.38

4.3.4. Accuracy of Lumped Muscle Parameters

The model prediction accuracy of lumped muscle parameters (r_{EMG}) was correlated with stature and gender as shown in Table 4-4. The r_{EMG} of BFs was generally close to that of RFs during the SW among all subjects (r = 0.59 versus r = 0.50), while the r_{EMG} of RFs were greater than that of BFs during DS (r = 0.66 versus r = 0.48). The model prediction accuracy of the lumped muscle parameters was better for males than for females (r = 0.68 versus r = 0.43).

Table 4-4: The r_{EMG} during the SW and DS for six subjects. The L and R for r_{EMG} during DS represent the side of the back-leg.

				Subject	1	2	3	4	5	6	
				Gender	F	F	F	M	M	M	Mean
				Stature (cm)	155	161	174	165	174.5	187.5	
r_{EMG}	SW	L (AFO)	BF		0.40	0.45	0.36	0.70	0.79	0.89	0.60
			RF		0.34	0.36	0.47	0.59	0.54	0.67	0.50
		R	BF		0.52	0.54	0.64	0.43	0.69	0.63	0.58
			RF		0.13	0.37	0.47	0.67	0.68	0.55	0.49
	DS	L (AFO)	BF		0.25	0.40	0.44	0.32	0.28	0.61	0.38
			RF		0.35	0.32	0.33	0.73	0.87	0.82	0.57
		R	BF		0.30	0.55	0.46	0.70	0.60	0.89	0.58
			RF		0.38	0.56	0.88	0.89	0.88	0.85	0.74

4.3.5. Accuracy of Step Lengths and Swing Time

As shown in Figures 4-3 and 4-4, the model prediction accuracy of step lengths (ε_{SL}) was correlated with stature, and the model prediction accuracy of swing time (ε_{TSW}) was not

correlated with any anthropometric parameter. Strong and moderate negative correlations were found between the stature and ε_{SL} of both legs (r = –0.64 for the left side and –0.44 for the right side), and no correlation was found between the stature and ε_{TSW} (r = –0.07 for the left side and –0.06 for the right side).

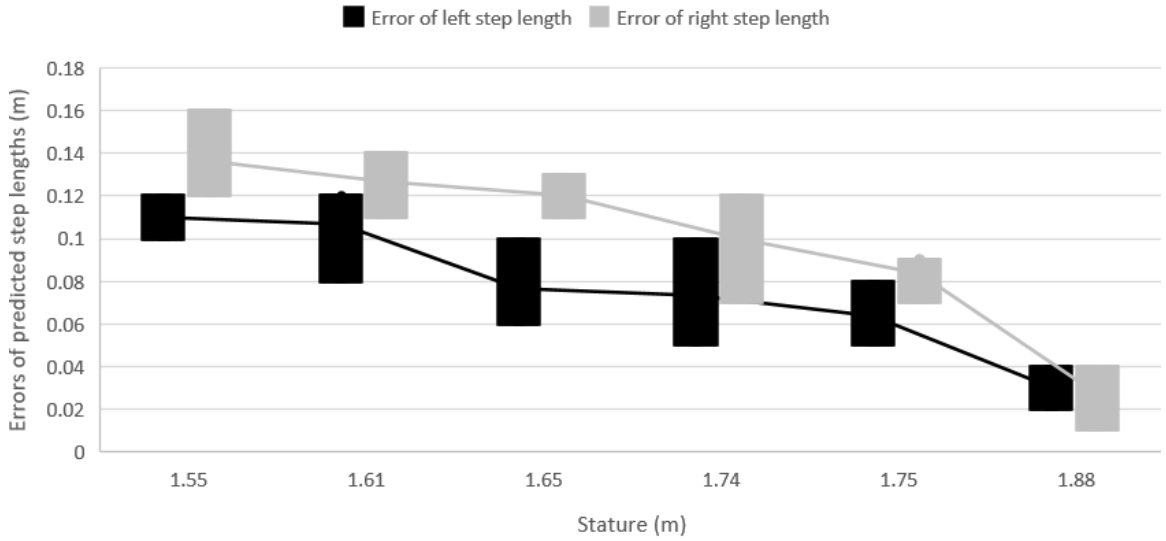

Figure 4-3: The range of errors of predicted step lengths for subjects with different statures (all conditions pooled).

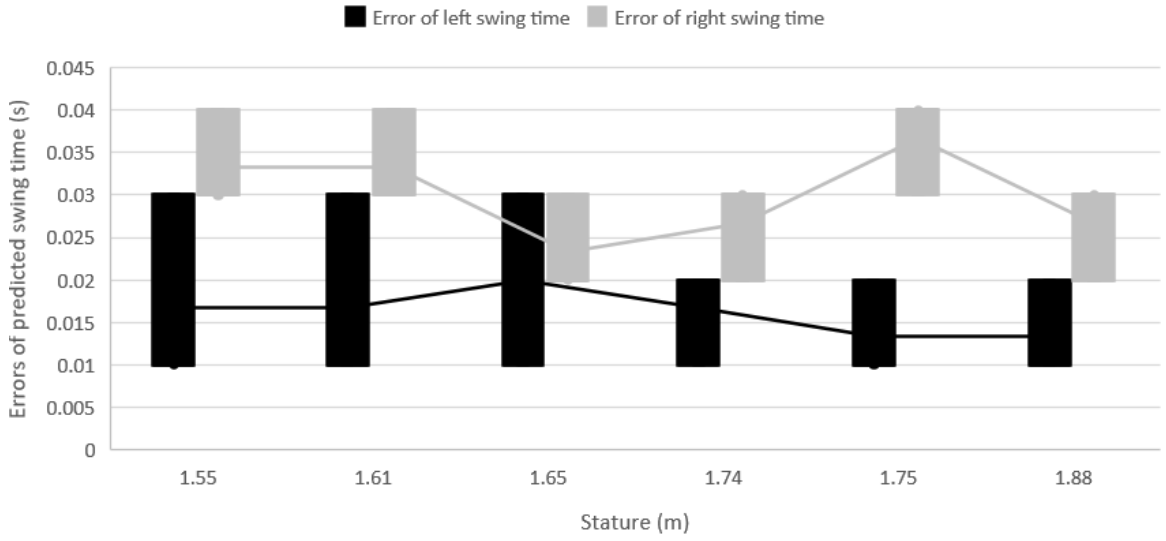

Figure 4-4: The range of errors of predicted swing time for subjects with different statures (all conditions pooled).

4.3.6. Accuracy of Gait Symmetry Index (SI)

The observed and predicted SIs for step lengths and swing time of all six subjects are summarized in Table 4-5. Consistency was found between the observed and predicted SIs for swing time. Inconsistency was found between the observed and predicted SIs for step length.

The errors in observed and predicted SIs for step length and swing time are shown in Figure 4-5. A weak negative correlation (r = –0.30) was found between the stature and errors of predicted SI for step length, and the error of predicted SI for swing time was not correlated with stature (r = 0.09).

Table 4-5: Calculated gait symmetry indices (SIs) for observed (O) and predicted (P) step lengths and swing time of six subjects.

Subject		1		2		3		4		5		6	
Gender		F		F		F		M		M		M	
Stature (cm)		155		161		174		165		174.5		187.5	
O vs. P		O	P	O	P	O	P	O	P	O	P	O	P
SI for step length (%)	NAFO	6±0.9	10±1.6	7±1.1	8±1.4	4±0.5	1±0.1	5±0.8	1±0.2	9±1.6	2±0.2	7±1	3±0.4
	AFO1	12±2.2	7±1.2	8±1.3	16±2.4	29±3.1	11±1.8	3±0.4	9±1.8	14±1.7	4±0.4	3±0.5	3±0.6
	AFO2	58±11.3	10±1.3	42±5.1	24±3.4	49±5.5	18±3.4	30±4	6±0.8	40±4.9	19±3.4	8±1.3	6±0.9
SI for swing time (%)	NAFO	1±0.2	1±0.2	11±1.2	11±1.1	1±0.2	3±0.4	5±1	3±0.6	7±0.8	20±3.8	6±0.8	8±0.8
	AFO1	10±1.1	13±2	23±3.5	22±3.1	6±1.2	6±1.1	6±1.2	15±2.7	6±0.7	3±0.3	10±1.6	10±1.7
	AFO2	6±0.9	11±1.7	23±3.6	24±4.2	6±0.9	12±1.7	23±2.6	23±4.3	23±2.9	21±3.3	17±2.9	22±4.3

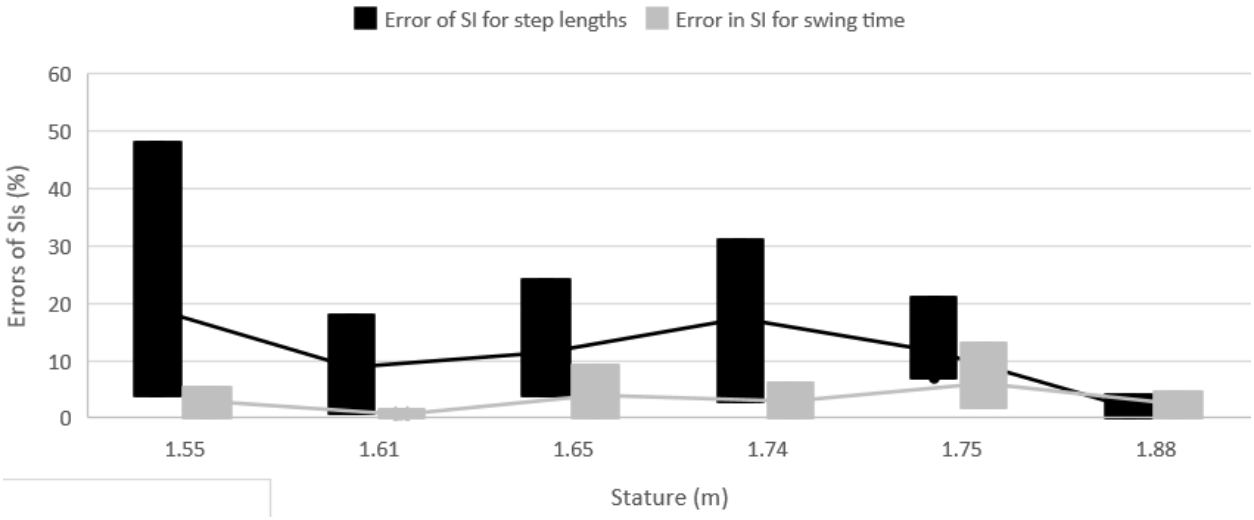

Figure 4-5: The range of errors of predicted SIs for step length and swing time of subjects with different statures (all conditions pooled).

4.3.7. Accuracy of Walking Speed

The error of the predicted walking speed (ε_{SP}) is shown in Figure 4-6. A moderate negative correlation (r = –0.55) was found between the stature and error of predicted walking speed.

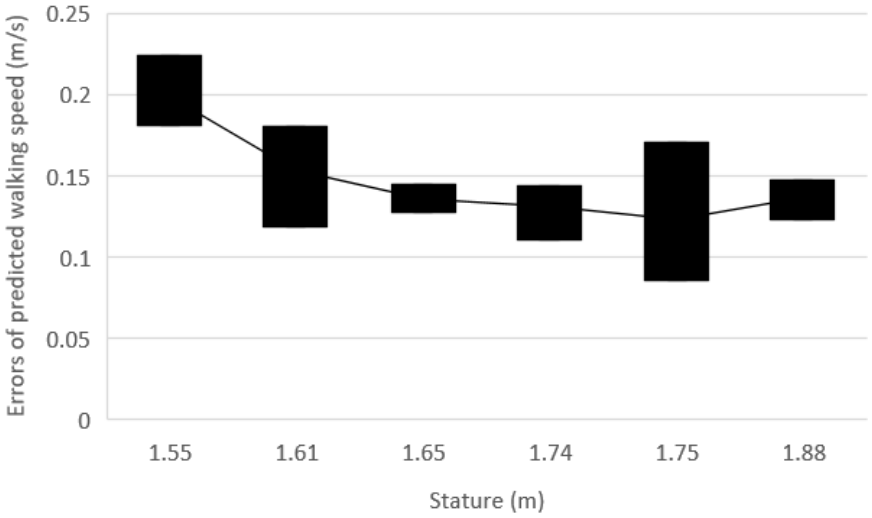

Figure 4-6: The range of errors of predicted walking speed for subjects with different statures (all conditions pooled).

4.4. Discussion

The model prediction accuracy among subjects with various anthropometry and other potential subject variables that may affect model prediction accuracy are discussed.

4.4.1. Accuracy of the Initial Conditions and Lumped Muscle Parameters

The prediction accuracy of the initial conditions and lumped muscle parameters from the inverse-dynamic mode of the PPCLMP model determines the model prediction accuracy of gait parameters from the forward-dynamic mode of the PPCLMP model. The predicted initial conditions were compared with observed initial conditions to quantitatively examine the prediction accuracy of initial conditions among subjects. The predicted lumped muscle parameters were compared with measured SEMG RMS regarding changing trends by utilizing

correlations to qualitatively examine the prediction accuracy of lumped muscle parameters among subjects.

The model prediction accuracy of the initial conditions (ε_{IC}) was significantly ($p < 0.05$) better with increasing stature (Table 4-2 and Table 4-3, the coefficients (ε_{IC} to stature) were –26°/m, –16°/m, –65°/m·s, –66°/m·s, –51°/m·s for the initial shank pitch angle $\theta(t_0)$, back-hip angle $\theta_{11}(t_0)$, shank pitch angular velocity $\dot{\theta}(t_0)$, back-hip angular velocity $\dot{\theta}_{11}(t_0)$, and back-ankle angular velocity $\dot{\theta}_{13}(t_0)$, respectively), but not affected by body mass or AFO stiffness. The variability of inter-subject prediction accuracy among various subjects was also reported by Findlow et al. [156] and Goulermas et al. [157] when utilizing shank-mounted and foot-mounted IMUs. One possible explanation is that taller subjects tend to walk faster which causes greater magnitudes of the signals measured by the IMU sensors while the magnitudes of noises remain the same, which resulted in better noise reduction performance of the Kalman filter [158] in framework shown in Figure 3-2. On the other hand, males are generally taller and walking faster than females [159,160] while females naturally have more hip abduction and pelvic obliquity than males during walking gait [126,127]. As the gender and stature were correlated in this study ($r = 0.59$), another explanation is that the prediction accuracy of initial conditions was better for males than females because of the gait pattern differences between genders instead of stature. The prediction accuracy of the initial conditions based on planar inverse dynamics is better for males because males have less lateral movements during gait. As discussed in Section 3.5.3, the PPCLMP model is limited to planar movement analysis. Efforts are needed to further develop the PPCLMP model to compensate for the 3-D movement or advance the model to a 3-D model.

The measured SEMG RMS patterns of BFs and RFs are consistent with the patterns reported in previous studies [150,151]. The correlations between the lumped muscle parameters and the mean SEMG RMS, r_{EMG}, were increased for taller subjects (Table 4-2 and Table 4-4, the coefficients (r_{EMG} to stature) were 1.3 m^{-1}, 0.9 m^{-1}, 0.5 m^{-1}, 1.1 m^{-1}, 0.9 m^{-1}, 1.4 m^{-1}, 1.3 m^{-1}, 1.4 m^{-1} for the lBF, lRF, rBF, and rRF during SW and DS, respectively). The r_{EMG} was greater for the RF than for the BF during the DS. This is because the RFs are the agonists that mainly contribute to the torque of the back-hip during DS while the BFs are acting mainly as the antagonists that kept the hip torque stable. The significant increments in the SEMG RMS of RFs during DS were consistently observed in this study (Figure 4-2) and previous studies [152–154].

The lumped muscle parameter prediction accuracy of hip joints was significantly better for males than females (Table 4-2) regarding the lBF (0.79±0.08 versus 0.40±0.04) and rRF (0.63±0.06 versus 0.32±0.14) during SW and the lRF (0.81±0.06 versus 0.33±0.01), rBF (0.73± 0.12 versus 0.44±0.10), and rRF (0.87±0.02 versus 0.61±0.21) during DS. Female was found to have more complex recruitment of the lower limb muscles than male during walking gait as the SEMG RMSs of VL and GM were significantly greater for female than male [127,161]. The lumped muscle parameters for hip joints were only compared with the SEMG signals of the BF and RF, while hip joint flexion and extension torques are generated by the work of a group of related muscles including BF, RF, vastus lateralis (VL), vastus intermedius (VI), vastus medialis (VM), hamstrings, gluteus maximus (GM), etc. The method of using the correlation between lumped muscle parameters and only BF or RF tends to be less effective for females than males, which may explain the better prediction accuracy for males than females.

The correlation between the SEMG of the BF and RF and the lumped muscle parameters of the knee joint was not investigated in this study. Though the BF and RF also contribute to the knee joint flexion and extension torques, the knee lumped muscle parameters were not significantly changed in this study (Appendix E) and Chapter 3 (Table 3-7).

4.4.2. Accuracy of the Step Lengths, Swing Time, Gait Symmetry, and Walking Speed

The model prediction accuracy of step lengths (ε_{SL}) was found to be better for taller subjects (Table 4-2 and Figure 4-3, coefficients of ε_{SL} to stature were −0.04 and −0.08 for left and right sides, respectively). This can be explained by better prediction accuracy of the initial conditions and lumped muscle parameters for taller subjects as explained in Section 4.1. Consequently, the model prediction accuracy of SI for step length (Figure 4-5 and Table 4-2, the coefficient of ε_{SISL} to stature was −30%/m) and walking speed (Figure 4-6 and Table 4-2, the coefficient of ε_{SP} to stature was −0.12/s) was better for taller subjects. The model prediction accuracy of swing time was not significantly affected by any anthropometric parameter because the swing time was estimated based on the three-axis accelerations measured by the IMU without being processed by the Kalman filter or the inverse-dynamic mode of the PPCLMP model. Results suggest that the model can be used to perform gait evaluations based on SI for step length and walking speed for tall subjects, while gait evaluations based on SI for swing time can be performed for subjects with a wide range of stature.

4.4.3. Other Subject Variables

Besides stature, body mass, and gender, other subject variables could also affect the model prediction accuracy. The model characterizes lower limb segments as rods with masses and negligible thickness, which ignores the body thickness. For subjects with higher BMI, this assumption tends to be invalid. This study recruited subjects with a small range of BMI (18 to

28). Larger sample size with a wider range of BMI is needed to further investigate how the BMI could affect the model prediction accuracy.

Besides, researchers found that age was another factor that could affect gait performance [162,163]. Elder people were found to have shorter step lengths, and the effect of stature on step lengths was fading with increasing age [162]. The PPCLMP model was assuming the hip and knee joint torques to be linearly related to joint angles based on the torques of young adults reported by Winter [13]. However, people with advanced age were found to have more variation and less stability on their joint torques [164,165]. Though the model showed good prediction accuracy for six young adults in this study, the use of lumped muscle parameters might become less effective while predicting gait for the elder populations. Further investigations are needed to evaluate the model for predicting the gait of elder people.

4.4.4. Limitations and Future Work

The major limitations of this study were the number of SEMG units used and the sample size. Only four SEMG units were used in this study that measured the activities of BFs and RFs in order to validate hip lumped muscle parameters. Other muscles that contribute to hip joint torques and other joint torques should be studied to thoroughly examine the prediction accuracy of the lumped muscle parameters. Though anthropometric inputs were various in this study, there were only six subjects recruited. More subjects should be studied to improve the statistical power of the results.

4.5. Conclusions

This study investigated the model accuracy of the initial conditions, lumped muscle parameters, step lengths, swing time, and walking speed among various anthropometry (stature,

body mass, and gender). The model prediction accuracy of initial conditions, lumped muscle parameters, step lengths, and walking speed was significantly better for taller subjects, while the accuracy of swing time was not significantly affected by stature, body mass, gender, or AFO condition. The prediction accuracy of lumped muscle parameters was better for males than females. Other subject variables including BMI and age may affect model prediction accuracy and need further investigation.

CHAPTER 5 Discussion

The proposed planar piecewise-continuous lumped muscle parameter (PPCLMP) model shows its capability in the investigation of joint stiffness change on gait performance. This dissertation uses ankle stiffness that increased by ankle-foot orthosis (AFO) as an example to demonstrate and examine the model. The broader applications and suggested future work for the PPCLMP model are summarized in this chapter.

5.1. Broader Applications

5.1.1. Developing a Decision Support System of AFO Design

As discussed in Chapter 2, the model used in the forward-dynamic mode forms the basis of a decision support system for AFO design. Though the current model could not determine the optimal AFO stiffness for the user like artificial intelligence, it could help the users of this system, clinicians and patients, investigate how different AFO designs could result in different gait patterns without the time-consuming fabrication, fitting, and testing process. A webpage listed in Appendix G is developed to demonstrate using this model as an investigation tool. As shown in Figure 5-1, the user could input the patient's height, weight, default or estimated lumped muscle parameters, and an AFO stiffness to get the predicted gait parameters (joint kinematics, swing time, step length) and quality metrics (walking speed and SI for swing time and step length) from the model based on phase continuity and forward dynamics. If the

predicted gait performance is not acceptable or below expectations, the user could change the input AFO stiffness to repeat this process until the user accepts the predicted gait.

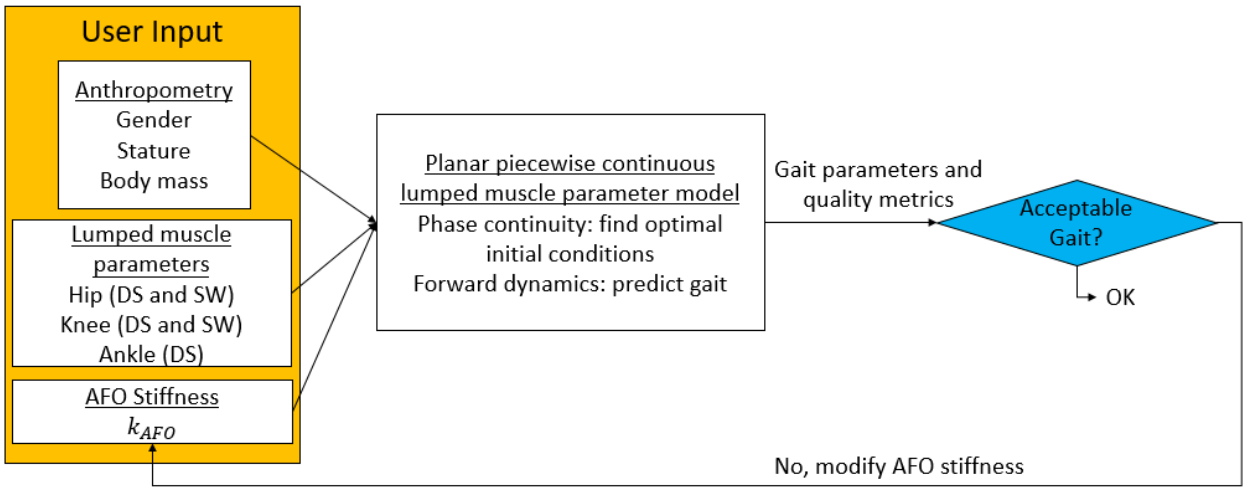

Figure 5-1: Workflow for predicting AFO stiffness effect on gait and searching for optimal AFO stiffness.

The ideal decision support system should be able to give the optimal AFO stiffness for a given patient based on the patient's information (anthropometry, impairment, etc.) collected at the clinic. The gaps between the proposed model and an ideal decision support system are:

- The efforts needed to achieve the optimal AFO stiffness.
- The qualitative prediction is not sufficient.

To achieve the optimal AFO stiffness, the user may need to explore through all possible AFO stiffness to compare among the predicted gait performances using the model. This could be tedious and time-consuming. More efforts are needed to directly link the optimal AFO stiffness with patients' information to simplify this decision support process.

In addition, Chapter 2 only qualitatively predicts how AFO stiffness could affect gait as a result of ignorance of the variability among gaits for the same person and among people under different walking scenarios [79,168,169]. Therefore, the predicted gait may not be quantitatively aligned with the actual gait of the person wearing the AFO. There are still many challenges to quantitatively predict the patient's gait with given AFO stiffness only based on their information

collected at the clinic. These challenges include how a patient would adapt to the AFO stiffness in both short and long term and how patients walking preference under different walking scenarios.

5.1.2. Developing a Cyber-based System for AFO Evaluation

As Chapters 3 and 4 demonstrated the model's capability in quantitatively predicting gait parameters, SI for swing time, and walking speed based on kinematic data measured by the inertial measurement unit (IMU) attached to AFO, a cyber-based AFO evaluation system can be built, as shown in Figure 5-2. Patients could wear an AFO with IMU that collects their gait information both in and out of the clinic or other point-of-care site. This information will be uploaded to a data center and utilized to estimate initial conditions and lumped muscle parameters by the inverse-dynamic mode of the model. Based on the estimated initial conditions and lumped muscle parameters, the model will provide the gait prediction and evaluation concerning the quality metrics, such as SI for swing time, SI for step length, and walking speed. The clinicians could have quantified feedback on the gait with the current AFO stiffness based on these metrics. This information could help the clinicians determine if the current AFO stiffness needs adjustment to better fit the patient, as well as give insights on future AFO design that should be used for a specific patient in the future. The advantage of this system is not only giving objective and quantitative feedback but also evaluating gaits with the AFO under different walking scenarios and environments that the specific patient is engaging with during the patient's daily living. Furthermore, 3-D scanning, computer-aided design (CAD), and 3-D printing technologies are now available to design and fabricate an AFO with a specific bending stiffness in a day. The proposed evaluation system could integrate these technologies to improve

the whole design and fabrication process of AFO from handmade to cyber-based to increase fabrication quality and reduce processing time and cost [170].

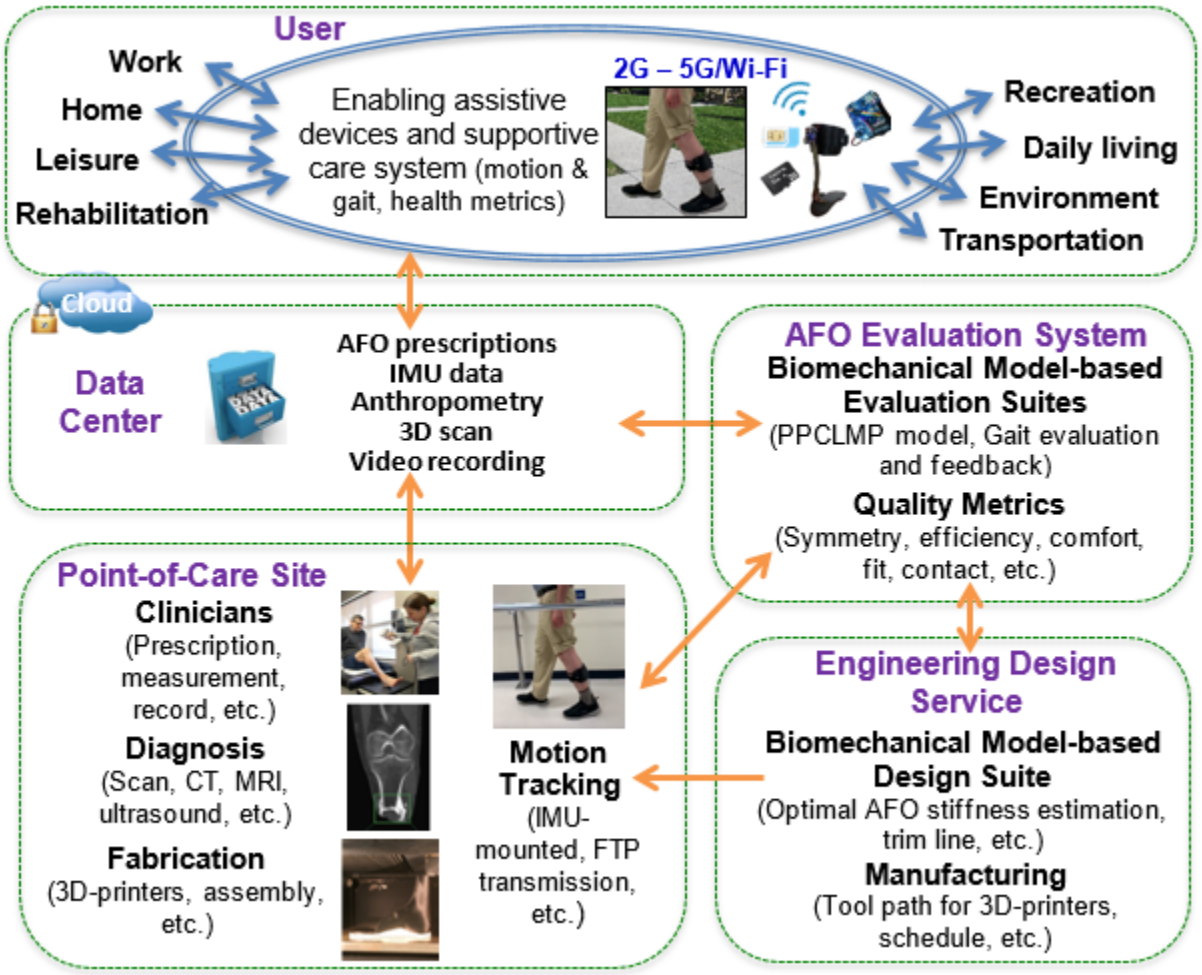

Figure 5-2: Overview of a cyber-based AFO design and evaluation system

5.1.3. Investigating of Joint Stiffness

Though the dissertation uses different AFOs, specifically different AFO bending stiffnesses, as examples to develop and examine the proposed PPCLMP model on investigating gait with different ankle joint stiffnesses, the PPCLMP model can be modified and implemented in a wider range of gait investigations on:

- Different ball (of foot) stiffnesses due to wearing different shoes or different AFO footplate stiffnesses.

- Different knee and hip joint stiffnesses due to impairment or wearing passive-dynamic assistive devices.
- More complicated joint toque patterns – active assistive devices, exoskeletons, etc.

The AFO footplate stiffness was found to be affecting the rotation of the ball of the foot [171]. Further, ball of foot rotation during the stance phase was found to be the determinant of ground reaction force pattern and energy transition between the swing (SW) and stance phases [172,173]. The model has the capability of evaluating different AFO footplate stiffnesses by adding a stiffness parameter to the ball of the foot.

The knee and hip stiffnesses during gait can be changed due to aging, different walking tasks, wearing passive assistive devices (lower limbs orthotics or prosthetic devices), osteoarthritis, joint replacement, etc. [174–179]. The effect of the knee and hip joint stiffness changes can be evaluated and predicted by the model via changing the joint torque equations at the hip and knee joints in the model. Similar to Eq. (2-4), the knee and hip joint torques can be estimated by adding a stiffness term as shown below:

$$T_{ijp}(t) = S_{ijp}(\theta_{ij}) + k_{ijp}\theta_{ij}(t) \quad (5\text{-}1)$$

where i represents the joint (1 for hip and 2 for knee), j represents the side (1 for left and 2 for right), p represents the phase (1 for single stance phase (SS), 2 for double stance phase (DS), and 3 for SW), T_{ijp} represents the torque for joint i on j side during the p phase, S_{ijp} represents the joint stiffness, k_{ijp} represents the lumped muscle parameter, and θ_{ij} represents the joint angle. The joint stiffness term might be a function of joint angle or a constant that could be different between phases depending on the pattern of joint stiffness to be simulated. With this modification, the model could give insights on how these changes would result in different gait parameters and different gait performance regarding the SI and walking speed.

As mentioned in Chapter 2, the muscle model was simplified as a rotational spring from the classic Hill's muscle model [166]. This does not mean that the model is limited to using rotation spring representations for muscle activities or joint torque patterns. For gait with an assistive device that has known torque patterns during each phase, the model can estimate and predict the gait performance by modifying one or more of the joint torques into pre-determined torque patterns during gait. For example, the active AFO is designed to provide a plantar-flexion torque at the ankle to assist the push-off [180]. The equation for ankle torque during DS (Eq. 2-4) could be modified into the following form to simulate the active AFO effect to the ankle torque:

$$T_{i32}(t) = T_{AFO}(\theta_{i3}, t) + rM_0 + k_{AFO}\theta_{i3}(t) \tag{5-2}$$

where r represents the active torque normalized by body mass at the ankle joint generated by the muscle, M_0 represents the body mass, and T_{AFO} represents the active torque provided by the active AFO. Such torque patterns may be a function of ankle joint angle, time during the push-off, or both [181].

5.2. Suggestions for Future Work

The PPCLMP model proposed in this dissertation shows a lot of potentials in estimating and predicting the effect of changing joint stiffness in lower limbs on gait using the AFO as an example. Further work is needed to thoroughly examine the model and develop the actual system that utilizes the model for practical applications.

The study presented in Chapter 2 gives the qualitative prediction of gait that can be used as a tool for investigating different AFO designs. However, there are still gaps between the model and an intelligent system that gives the optimal stiffness of the AFO for a given patient.

More efforts are needed to simplify the process and reduce the efforts needed to achieve optimal AFO stiffness and improve the model prediction.

The study presented in Chapter 3 shows the possibilities of longer-term quantitative gait evaluation by attaching the IMU to AFO. However, there are still many practical issues including IMU data transmission, battery charging, providing technical support, and improving system robustness to be solved and examined before the implementation.

Both approaches in Chapters 2 and 3 find the optimal solution by utilizing the enumeration searching method, which is slow and inefficient. There are other advanced non-linear algorithms available to find the optimal solutions for non-convex optimization problems [182–184]. Besides, machine learning could link the output with the input to simplify the prediction process by training the system with a large amount of data [185,186]. Also, because the possible input combinations are finite, if we limited the precision of the input, a lookup table could be used for finding the optimal solutions by generating a multi-dimensional table for all possible inputs and associated outputs [187,188]. Further investigations are needed to develop and evaluate the means of applying these options in reducing the time and efforts needed for gait prediction using the model.

The study presented in Chapter 4 shows the effect of different stature on model prediction. There are other anthropometry or personal factors that could affect model prediction, including age, gender, and BMI. Further studies with larger sample sizes are needed to systematically examine these factors. In addition, investigations are needed to examine the hypothesis of better IMU noise reduction for taller people (faster walking) in Chapter 4.

The model assumes the knee is straight during the inverted pendulum movement, and the front-knee is straight during the kinematic chain movement. Though the observed knee angle

during these phases was less than 10 degrees, these assumptions need to be examined for patients who may have quite different joint kinematics than the subjects recruited in this dissertation. Further, the effect of the flexed knee during DS and SS on model prediction should be investigated.

The model was developed to only describe movement in the sagittal plane. However, lateral movement of legs during gait was observed in Chapters 3 and 4, and also reported by other studies [5,8]. Possible ways to resolve this issue should be proposed and evaluated. For example, the model can be developed into a quasi-3-D model by adding one degree of freedom (abduction/adduction) to the hip joint. This could improve the model prediction of the SW by changing the planar double pendulum model to a more realistic conical double pendulum model. Another possible way is to compensate for the lateral movement by changing the effective lengths of the body segments in the model. These methods may help with estimating and compensating the lower limb movements out of the sagittal plane.

The model was developed based on the dynamic models that describe walking on a level surface. Walking on incline and decline surfaces, such as ramps, can have a quite different mechanism due to the change of whole-body angular momentum [189,190]. Efforts are needed to modify the model accordingly, such as change the direction of gravitational force, to predict walking on a sloped surface.

Though the model utilizes spring representations for muscles to reduce the dimensions of variables in the model, it ignores the viscoelasticity of muscles [166]. Classic Hill's muscle model may be implemented in the PPCLMP model to improve model prediction accuracy. The trade-off between prediction accuracy and complexity of the model should be considered.

The model was developed and evaluated by using the ankle with different AFOs as an example of changing stiffness that affects gait. As discussed in Section 5.2.3, there are possible applications of the model regarding investigating the effect of different joint stiffness on task performance. Extra efforts are needed to examine the usability and values of the proposed model in other applications.

The model shows the possibility of predicting human movement by using dynamic systems to characterize the movements of body segments during different phases of walking gait. Similar ideas might be able to work on the upper limbs to evaluate the effect of joint stiffness in the upper limbs on task performance. The application includes but not limited to simulate the effect of upper limbs industrial exoskeletons, prosthetic devices, clothing (space suit), and impairments.

CHAPTER 6 Conclusions

This dissertation describes the development of a planar piecewise continuous lumped muscle parameter (PPCLMP) model for predicting gait and evaluating the effect of joint stiffness on gait. This was achieved through the following aims:

- Develop a PPCLMP model that predicts how joint stiffness affects gait based on forward dynamics.
- Utilize data from a single inertial measurement unit (IMU) attached to the lower shank to estimate the initial conditions and lumped muscle parameters for each gait cycle based on inverse dynamics to improve the model prediction of gait.
- Evaluate the model prediction accuracy for various anthropometric inputs by comparing predicted gait parameters with measurements.

The proposed PPCLMP model connects three existing biomechanical models (the inverted pendulum model for SS, the double pendulum model for SW, and the kinematic chain model for DS) to predict leg movement across the whole gait cycle for investigation of joint stiffness in walking on a level surface. By using the ankle with ankle-foot-orthosis (AFO) as an example of changing joint stiffness, the PPCLMP model shows its capacity on investigating joint stiffness in walking gait. The model also forms the basis of an AFO design and evaluation system by predicting and evaluating gait with AFO based on the anthropometry, lumped muscle parameters, initial conditions, and AFO stiffness, as shown in Figure 6-1.

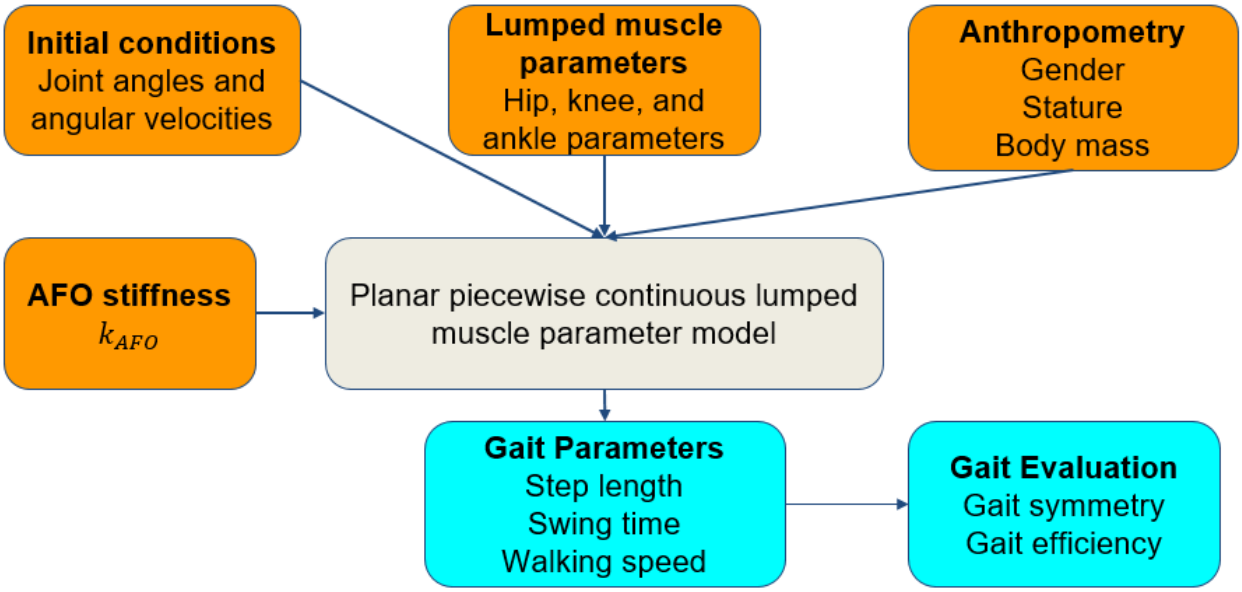

Figure 6-1: Overview of the model inputs (orange) and model outputs (blue).

Chapter 2 describes the development of the PPCLMP model. The model contains three continuous dynamic systems: the inverted pendulum to simulate the single stance phase (SS) movement, the double pendulum to simulate the swing phase (SW) movement, and the kinematic chain to simulate the double stance phase (DS) movement. Within each dynamic system, the joint torques are determined by the inputted lumped muscle parameters. With given initial conditions of the gait, the model could calculate the end conditions of the gait based on the equations of motion of each dynamic system based on forward dynamics. By assuming phase continuity, the model utilizes the forward-dynamic mode to search for the initial conditions that minimize the differences between the end conditions and the initial conditions based on the lumped muscle parameters estimated from the join torques reported by Winter [13]. Comparing with the experimental measurements, the model showed the capability of qualitatively predict how increased ankle stiffness affects gait in terms of swing time and step length.

The model reveals the two major effects of the ankle stiffness increased by AFO on walking gait. During the SS, the AFO slows down the inverted pendulum movement and stores

energy. During the DS with the AFO on the back-leg, the AFO releases energy when the ankle is in dorsiflexion but prevents the ankle from generating more energy when the ankle is in plantar flexion. These findings explain how increased ankle stiffness affects gait from the energy perspective.

To compensate for the gait variability among different people and different scenarios, Chapter 3 focuses on utilizing the kinematic data measured by an IMU attached to the AFO to estimate the initial conditions and lumped muscle parameters to enhance the model prediction based on inverse dynamics. A framework was developed to estimate the swing time, stance time, and shank pitch angles and angular velocities based on IMU data. These estimated values are then used in an optimization problem to search for the optimal initial conditions and lumped muscle parameters based on the commonly used minimizing energy expenditure assumption [115–117]. Comparing with results in Chapter 2, the gait parameter prediction was improved by utilizing the IMU: the RMSE of step length and swing time were 0.07 m and 2% of gait duration, respectively, by utilizing IMU in Chapter 3 comparing with 0.15 m and 5% of gait duration in Chapter 2.

Based on the process of finding the initial conditions and lumped muscle parameters proposed in Chapter 3, the model showed the capability of quantitative prediction on swing time, impaired side step length, and walking speed for two drop foot patients. However, the model showed limited capability in predicting unimpaired side step length. The prediction of the step length was better for the impaired side than the unimpaired side because more information about the impaired side is provided by the IMU attached to the AFO.

To evaluate gait based on the predicted gait parameters, gait symmetry index (SI) [66], and walking speed (gait efficiency) are used as criteria for gait evaluation. The model shows

good prediction in walking speed and SI for swing time but not in the SI for step length due to the better prediction of the impaired-side step length than the unimpaired step length.

Chapter 4 is a data-based focusing on the effect of different anthropometric inputs on model prediction accuracy. Results showed that the model prediction accuracy of gait parameters was better for taller people than for shorter people, regardless of gender or body mass. A possible explanation was that the IMU noise reduction, or the Kalman Filter performance, was better for taller people because taller people walk faster, and have a greater magnitude of the signal compared with the noise.

The PPCLMP model is limited by its assumption of the straight knee during SS and DS (front knee) and the planar representation of leg movements during gait. The front knee was found to be not exactly straight during SS and DS (Table 2-8**Error! Reference source not found.**). The effect of a flexed knee on model prediction accuracy should be investigated. On the other hand, leg movements during gait were found to be 3-D instead of planar, especially for female [126,127]. Efforts are needed to further develop the model to accommodate the lateral movements of legs during gait.

This dissertation builds into a broader set of research related to the biomechanical model of human gait. This dissertation is using wearing different AFOs or changing ankle stiffness as an example to show how different joint stiffnesses could affect gait performance. The three studies gradually developed the model from a conceptual model to a practical model that could utilize wearable technologies for gait prediction and evaluation and investigated each input type of the model, as shown in Figure 6-2.

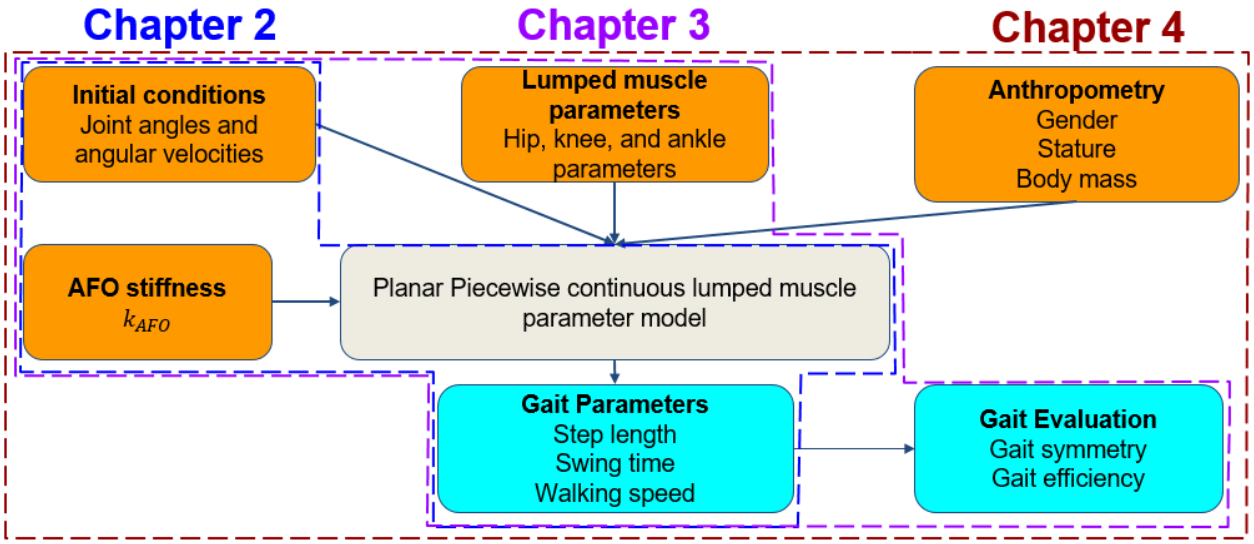

Figure 6-2: The scope of investigations on model inputs and outputs in Chapters 2, 3, and 4.

The limitations of the model are not including viscous resistance of body tissues to joint motion, not knowing the optimization strategy of subjects during gait, not looking at different gait speeds, not looking at step over an obstacle or on a rough surface, not including the axial movement of the pelvis, not including the lengthening versus shortening behavior of the agonists, not including more EMGs, and not have enough subjects to give much statistical power. Nonetheless, the hypotheses of each study were tested and the approaches in this dissertation had promising results. Chapter 2 showed the model capacity in qualitatively predicting gait parameter changes of gait with different AFOs while no motion tracking data are available. Chapter 3 showed the model capacity in quantitatively predicting gait parameters while utilizing IMU data. Chapter 4 showed the significant improvement of model prediction accuracy for taller subjects.

APPENDICES

Appendix A: Modeling of the Kinematic Chain during DS

The DS starts with HS and ends with TO. The DS is characterized as a kinematic chain that consists of links and joints. During this phase, the front-foot and toe of the back-foot are constrained on the ground. Thus, there is a series of geometry equations, force balance equations, and torque equations need to be satisfied.

A1. Geometry

All the equations in this Appendix are based on DS with the right leg in front. The kinematic chain during DS is constrained with the back-toe and front-heel on the ground. Thus, the vertical location of the back-toe should be equal to the vertical location of the front heel (Figure A1):

$$(L_1 + L_2)\cos\theta_{21} + L_4 = L_4\cos\theta_{10} + L_3\sin\theta_{10} + L_2\cos(\theta_{10} + \theta_{13}) - L_1\cos\theta_{11}$$

where L_1 is the upper leg length, L_2 is the lower leg length, L_3 is the foot length, θ_{21} is the front-hip (right) angle, θ_{10} is the angle between the left foot and ground, θ_{13} is the left ankle angle, and θ_{11} is the left hip angle.

The hip flexion angle is defined as the angle between the upper leg and the gravitational direction. Thus, the relationship between angles is:

$$-\theta_{11} = \theta_{10} + \theta_{13} - \theta_{12}$$

where θ_{12} is the back-knee (left) flexion angle.

The joint angles and angular velocities satisfy:

$$\frac{d\theta_{ij}}{dt} = \dot{\theta}_{ij}$$

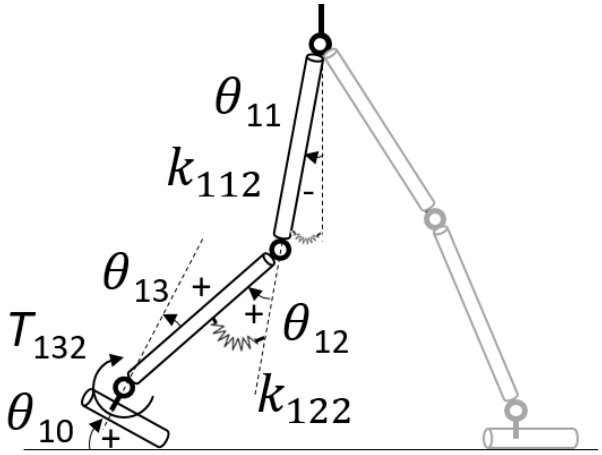

Figure A1: Diagram of DS posture with the right leg in front.

A2. Free Body Diagram – Back-Foot (Left)

As shown in Figure A2, the left foot angular acceleration satisfies the torque balance equation:

$$\frac{d^2\theta_{10}}{dt^2} = \dot{\omega}_{Foot} = \frac{-F_{ax}L_3\cos\theta_{13} + F_{ay}L_3\sin\theta_{13} + T_{13DS} - 0.5M_3L_3g\cos\theta_{10}}{\frac{1}{3}(M_3L_3^2)}$$

where F_{ax} is the ankle axial force, F_{ay} is the ankle shear force, M_3 is the foot mass, ω_{foot} is the foot angular velocity.

The foot center of mass (COM) horizontal acceleration is:

$$\dot{v}_{3cx} = -0.5\dot{\omega}_{foot}L_3\sin\theta_{10} - 0.5\omega_{foot}^2L_3\cos\theta_{10}$$
$$= \frac{-F_h + F_{ay}\cos(\theta_{10}+\theta_{13}) + F_{ax}\sin(\theta_{10}+\theta_{13})}{M_3}$$

where F_h is the horizontal ground reaction force.

Similarly, the foot COM vertical acceleration is:

$$\dot{v}_{3cy} = 0.5\dot{\omega}_{foot}L_3\cos\theta_{10} - 0.5\omega_{foot}^2L_3\sin\theta_{10}$$
$$= \frac{F_v + F_{ay}\sin(\theta_{10}+\theta_{13}) - F_{ax}\cos(\theta_{10}+\theta_{13}) - M_3g}{M_3}$$

where F_v is the vertical ground reaction force.

Further, the toe was fixed to the ground, and the ankle was rotating about the toe. Thus, the ankle joint horizontal and vertical accelerations are:

$$\dot{v}_{3x} = -\dot{\omega}_{foot}L_3\sin\theta_{10}$$

$$\dot{v}_{3y} = \dot{\omega}_{foot}L_3\cos\theta_{10}$$

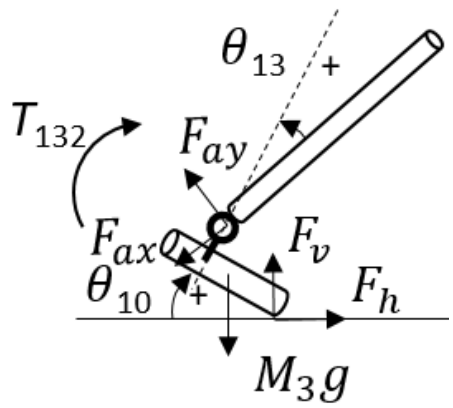

Figure A2: Diagram of forces and torque that applied to the left foot.

A3. Free Body Diagram – Back-Lower-Leg (Left)

As shown in Figure A3, the left lower leg angular acceleration satisfies the torque balance equation:

$$\dot{\omega}_{lowerleg} = \frac{d^2\theta_{13}}{dt^2} + \dot{\omega}_{foot}$$

$$= \frac{F_{kx}L_2 \sin\theta_{12} - F_{ky}L_2 \cos\theta_{12} - T_{13DS} - k_{12DS}\theta_{12} + 0.5M_2 g L_2 \sin(\theta_{10} + \theta_{13})}{\frac{1}{3}(M_2 L_2^2)}$$

where F_{kx} is the knee axial force, F_{ky} is the knee shear force, M_2 is the lower leg mass, and $\omega_{lowerleg}$ is the lower leg angular velocity.

The lower leg COM horizontal acceleration is:

$$\dot{v}_{2cx} = \dot{v}_{3x} - 0.5\dot{\omega}_{lowerleg}L_2 \cos(\theta_{10} + \theta_{13}) + 0.5\omega_{lowerleg}^2 L_2 \sin(\theta_{10} + \theta_{13}))$$

$$= \frac{F_{kx}\sin\theta_{13} + F_{ky}\cos\theta_{13} - F_{ay}\cos(\theta_{10} + \theta_{13}) - F_{ax}\sin(\theta_{10} + \theta_{13})}{M_2}$$

Similarly, the lower leg COM vertical acceleration is:

$$\dot{v}_{2cy} = \dot{v}_{3y} - 0.5\dot{\omega}_{lowerleg}L_2 \sin(\theta_{10} + \theta_{13}) - 0.5\omega_{lowerleg}^2 L_2 \cos(\theta_{10} + \theta_{13})$$

$$= \frac{-F_{kx}\cos\theta_{13} + F_{ky}\sin\theta_{13} - F_{ay}\sin(\theta_{10} + \theta_{13}) + F_{ax}\cos(\theta_{10} + \theta_{13}) - M_2 g}{M_2}$$

Further, the knee joint horizontal and vertical accelerations are:

$$\dot{v}_{2x} = \dot{v}_{3x} - \dot{\omega}_{lowerleg}L_2 \cos(\theta_{10} + \theta_{13}) + \omega_{lowerleg}^2 L_2 \sin(\theta_{10} + \theta_{13})$$

$$\dot{v}_{2y} = \dot{v}_{3y} - \dot{\omega}_{lowerleg}L_2 \sin(\theta_{10} + \theta_{13}) - \omega_{lowerleg}^2 L_2 \cos(\theta_{10} + \theta_{13})$$

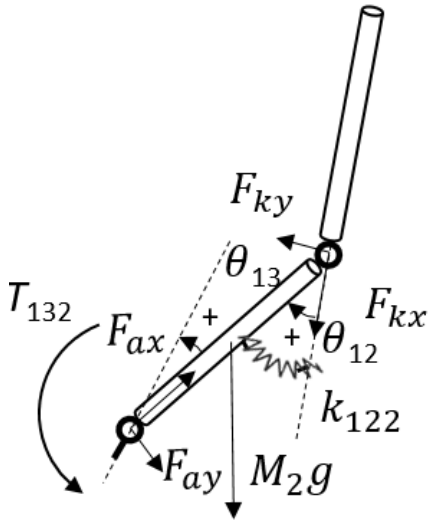

Figure A3: Diagram of forces and torque that applied to the left lower leg.

A4. Free Body Diagram – Back-Upper-Leg (Left)

As shown in Figure A4, the left upper leg angular acceleration satisfied the torque balance equation:

$$\dot{\omega}_{upperleg} = \dot{\omega}_{lowerleg} - \frac{d^2\theta_{12}}{dt^2} = \frac{d^2\theta_{11}}{dt^2}$$

$$= \frac{F_{hx}L_1 \sin(\theta_{11} + \theta_{21}) - F_{hy}L_1 \cos(\theta_{11} + \theta_{21}) - k_{13DS}\theta_{13} + k_{12DS}\theta_{12} + (0.5M_1 + M_4)gL_1 \sin\theta_{13}}{\frac{1}{3}(M_1L_1^2)}$$

where F_{hx} is the back-hip axial force, F_{hy} is the back-hip shear force, M_1 is the upper leg mass, $\omega_{upperleg}$ is the upper leg angular velocity.

The upper leg COM horizontal acceleration is:

$$\dot{v}_{1cx} = \dot{v}_{2x} - 0.5\dot{\omega}_{upperleg}L_1 \cos\theta_{11} + 0.5\omega_{upperleg}^2 L_1 \sin\theta_{11}$$

$$= \frac{-F_{kx}\sin\theta_{11} - F_{ky}\cos\theta_{11} + F_{hy}\cos\theta_{21} - F_{hx}\sin\theta_{21}}{M_1}$$

Similarly, the upper leg COM vertical acceleration is:

$$\dot{v}_{1cy} = \dot{v}_{2y} - 0.5\dot{\omega}_{upperleg}L_1 \sin\theta_{11} - 0.5\omega_{upperleg}^2 L_1 \cos\theta_{11}$$

$$= \frac{F_{kx}\,cos\,\theta_{11} - F_{ky}\sin\theta_{11} - F_{hy}\sin\theta_{21} - F_{hx}\cos\theta_{21} - M_1g - M_4g}{M_1}$$

Further, the hip joint horizontal and vertical accelerations are:

$$\dot{v}_{1x} = \dot{v}_{2x} - \dot{\omega}_{upperleg}L_1 \cos\theta_{11} + \omega_{upperleg}^2 L_1 \sin\theta_{11}$$

$$\dot{v}_{1y} = \dot{v}_{2y} - \dot{\omega}_{upperleg}L_1 \sin\theta_{11} - \omega_{upperleg}^2 L_1 \cos\theta_{11}$$

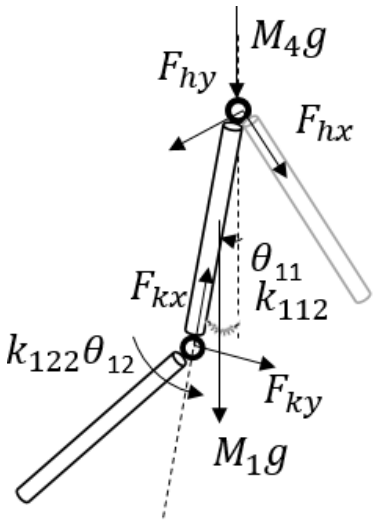

Figure A4: Diagram of forces and torque that applied to the left upper leg.

A5. Free Body Diagram – Front-Leg (Right)

As shown in Figure A5, the right front-leg angular acceleration satisfied the torque balance equation:

$$\dot{\omega}_{frontleg} = \frac{d^2\theta_{21}}{dt^2}$$

$$= \frac{F_{hy}(L_1 + L_2) - M_4 g(L_1 + L_2)\sin\theta_{21} - 0.5(M_1 + M_2)g(L_1 + L_2)\sin\theta_{21} + k_{DS3}\theta_{11}}{\frac{1}{3}(M_1 + M_2)(L_1 + L_2)^2}$$

where $\omega_{frontleg}$ is the front-leg angular velocity.

The front-leg center of mass (COM) horizontal acceleration is:

$$\dot{v}_{fcx} = 0.5\dot{v}_{1x} = 0.5(L_1 + L_2)\dot{\omega}_{frontleg}\cos\theta_{21} - 0.5\omega^2_{frontleg}(L_1 + L_2)\sin\theta_{21}$$

Similarly, the front-leg center of mass (COM) vertical acceleration is:

$$\dot{v}_{fcy} = 0.5\dot{v}_{1y} = 0.5(L_1 + L_2)\dot{\omega}_{frontleg}\sin\theta_{21} - 0.5\omega^2_{frontleg}(L_1 + L_2)\cos\theta_{21}$$

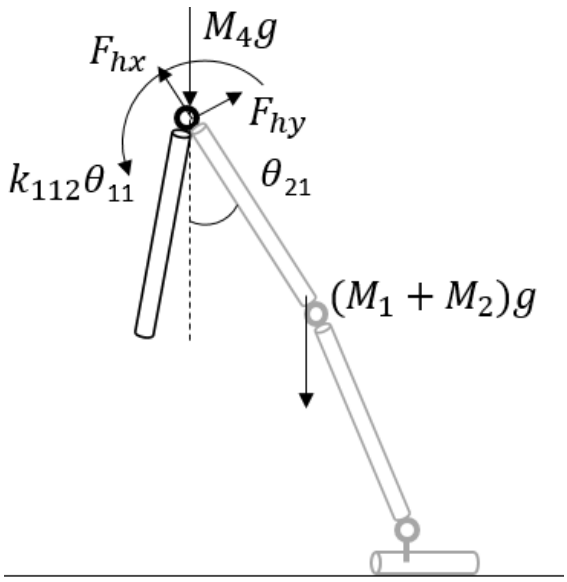

Figure A5: Diagram of forces and torque that applied to front-leg (right).

A6. Summary

There were in total of 31 equations and 34 variables. Thus, these equations can be solved implicitly to find the equations of motion that will be presented for angular accelerations: $\ddot{\theta}_{11}(t), \ddot{\theta}_{12}(t),$ and $\ddot{\theta}_{13}(t)$.

Appendix B: List of Combinations for Sensitivity Analysis in Chapter 2

The combinations for joint angles are shown in Tables B1, B2, B3, B4, B5, and B6. The combinations for joint angular velocities are separately listed in Table B7. For each joint angle combination, all combinations of joint angular velocities were examined.

Table B1: Combinations of joint angles (θ_{22}= 20 deg).

θ_{11}(deg)	θ_{12}(=0 deg)	θ_{13}(= -θ_{11})	θ_{21} (deg)	θ_{22} (deg)	θ_{23}*
5	0	-5	-5	20	-
10	0	-10	-5	20	-
15	0	-15	-5	20	-
			⋮		
30	0	-30	-5	20	-
5	0	-5	-10	20	-
10	0	-10	-10	20	-
			⋮		
30	0	-30	-10	20	-
5	0	-5	-15	20	-
10	0	-10	-15	20	-
			⋮		
30	0	-30	-15	20	-
5	0	-5	-20	20	-
10	0	-10	-20	20	-
			⋮		
30	0	-30	-20	20	-
5	0	-5	-25	20	-
10	0	-10	-25	20	-
			⋮		
30	0	-30	-25	20	-
5	0	-5	-30	20	-
10	0	-10	-30	20	-
			⋮		
30	0	-30	-30	20	-

*θ_{23} is calculated based on Eq. (2-16)

Table B2: Combinations of joint angles (θ_{22}= 25 deg).

θ_{11}(deg)	θ_{12}(=0 deg)	θ_{13}(= -θ_{11})	θ_{21} (deg)	θ_{22} (deg)	θ_{23}*
5	0	-5	-5	25	-
10	0	-10	-5	25	-
15	0	-15	-5	25	-
			⋮		
30	0	-30	-5	25	-
5	0	-5	-10	25	-
10	0	-10	-10	25	-
			⋮		
30	0	-30	-10	25	-
5	0	-5	-15	25	-
10	0	-10	-15	25	-
			⋮		
30	0	-30	-15	25	-
5	0	-5	-20	25	-
10	0	-10	-20	25	-
			⋮		
30	0	-30	-20	25	-
5	0	-5	-25	25	-
10	0	-10	-25	25	-
			⋮		
30	0	-30	-25	25	-
5	0	-5	-30	25	-
10	0	-10	-30	25	-
			⋮		
30	0	-30	-30	25	-

*θ_{23} is calculated based on Eq. (2-16)

Table B3: Combinations of joint angles (θ_{22}= 30 deg).

θ_{11}(deg)	θ_{12}(=0 deg)	θ_{13}(= -θ_{11})	θ_{21} (deg)	θ_{22} (deg)	θ_{23}*
5	0	-5	-5	30	-
10	0	-10	-5	30	-
15	0	-15	-5	30	-
			⋮		
30	0	-30	-5	30	-
5	0	-5	-10	30	-
10	0	-10	-10	30	-
			⋮		
30	0	-30	-10	30	-
5	0	-5	-15	30	-
10	0	-10	-15	30	-
			⋮		
30	0	-30	-15	30	-
5	0	-5	-20	30	-
10	0	-10	-20	30	-
			⋮		
30	0	-30	-20	30	-
5	0	-5	-25	30	-
10	0	-10	-25	30	-
			⋮		
30	0	-30	-25	30	-
5	0	-5	-30	30	-
10	0	-10	-30	30	-
			⋮		
30	0	-30	-30	30	-

*θ_{23} is calculated based on Eq. (2-16)

Table B4: Combinations of joint angles (θ_{22}= 35 deg).

θ_{11}(deg)	θ_{12}(=0 deg)	θ_{13}(= -θ_{11})	θ_{21} (deg)	θ_{22} (deg)	θ_{23}*
5	0	-5	-5	35	-
10	0	-10	-5	35	-
15	0	-15	-5	35	-
			⋮		
30	0	-30	-5	35	-
5	0	-5	-10	35	-
10	0	-10	-10	35	-
			⋮		
30	0	-30	-10	35	-
5	0	-5	-15	35	-
10	0	-10	-15	35	-
			⋮		
30	0	-30	-15	35	-
5	0	-5	-20	35	-
10	0	-10	-20	35	-
			⋮		
30	0	-30	-20	35	-
5	0	-5	-25	35	-
10	0	-10	-25	35	-
			⋮		
30	0	-30	-25	35	-
5	0	-5	-30	35	-
10	0	-10	-30	35	-
			⋮		
30	0	-30	-30	35	-

*θ_{23} is calculated based on Eq. (2-16)

Table B5: Combinations of joint angles (θ_{22}= 40 deg).

θ_{11}(deg)	θ_{12}(=0 deg)	θ_{13}(= -θ_{11})	θ_{21} (deg)	θ_{22} (deg)	θ_{23}*
5	0	-5	-5	40	-
10	0	-10	-5	40	-
15	0	-15	-5	40	-
			⋮		
30	0	-30	-5	40	-
5	0	-5	-10	40	-
10	0	-10	-10	40	-
			⋮		
30	0	-30	-10	40	-
5	0	-5	-15	40	-
10	0	-10	-15	40	-
			⋮		
30	0	-30	-15	40	-
5	0	-5	-20	40	-
10	0	-10	-20	40	-
			⋮		
30	0	-30	-20	40	-
5	0	-5	-25	40	-
10	0	-10	-25	40	-
			⋮		
30	0	-30	-25	40	-
5	0	-5	-30	40	-
10	0	-10	-30	40	-
			⋮		
30	0	-30	-30	40	-

*θ_{23} is calculated based on Eq. (2-16)

Table B6: Combinations of joint angles (θ_{22}= 45 deg).

θ_{11}(deg)	θ_{12}(=0 deg)	θ_{13}(= -θ_{11})	θ_{21} (deg)	θ_{22} (deg)	θ_{23}*
5	0	-5	-5	45	-
10	0	-10	-5	45	-
15	0	-15	-5	45	-
			⋮		
30	0	-30	-5	45	-
5	0	-5	-10	45	-
10	0	-10	-10	45	-
			⋮		
30	0	-30	-10	45	-
5	0	-5	-15	45	-
10	0	-10	-15	45	-
			⋮		
30	0	-30	-15	45	-
5	0	-5	-20	45	-
10	0	-10	-20	45	-
			⋮		
30	0	-30	-20	45	-
5	0	-5	-25	45	-
10	0	-10	-25	45	-
			⋮		
30	0	-30	-25	45	-
5	0	-5	-30	45	-
10	0	-10	-30	45	-
			⋮		
30	0	-30	-30	45	-

*θ_{23} is calculated based on Eq. (2-16)

Table B7: Combinations of joint angular velocities

$\dot{\theta}_{11}$(deg/s)	$\dot{\theta}_{12}$(=0 deg/s)	$\dot{\theta}_{13}$(= -$\dot{\theta}_{11}$)	$\dot{\theta}_{21}$ (deg/s)	$\dot{\theta}_{22}$ (deg/s)	$\dot{\theta}_{23}$*
-200	0	200	100	100	-
-150	0	150	100	100	-
-100	0	100	100	100	-
-200	0	200	150	100	-
-150	0	150	150	100	-
-100	0	100	150	100	-
-200	0	200	100	150	-
-150	0	150	100	150	-
-100	0	100	100	150	-
-200	0	200	150	150	-
-150	0	150	150	150	-
-100	0	100	150	150	-
-200	0	200	100	200	-
-150	0	150	100	200	-
-100	0	100	100	200	-
-200	0	200	150	200	-
-150	0	150	150	200	-
-100	0	100	150	200	-
-200	0	200	100	250	-
-150	0	150	100	250	-
-100	0	100	100	250	-
-200	0	200	150	250	-
-150	0	150	150	250	-
-100	0	100	150	250	-
-200	0	200	100	300	-
-150	0	150	100	300	-
-100	0	100	100	300	-
-200	0	200	150	300	-
-150	0	150	150	300	-
-100	0	100	150	300	-

*$\dot{\theta}_{23}$ is calculated based on Eq. (2-16)

Appendix C: AFO Stiffness Test.

As shown in Figure C1, the Stiffness Measurement Apparatus (Courtesy: Barton Research Group) was used to test the stiffnesses of the AFOs used in this dissertation. The stiffness of AFOs used in Chapter 4 was tested before (12/14/2019) and after (2/15/2020) the six subjects' trials to validate that the AFO stiffness was not changed significantly after used. Each AFO was tested for 5 cycles (from neutral to dorsiflexion, then to plantar flexion, and back to neutral) for before and after the trials.

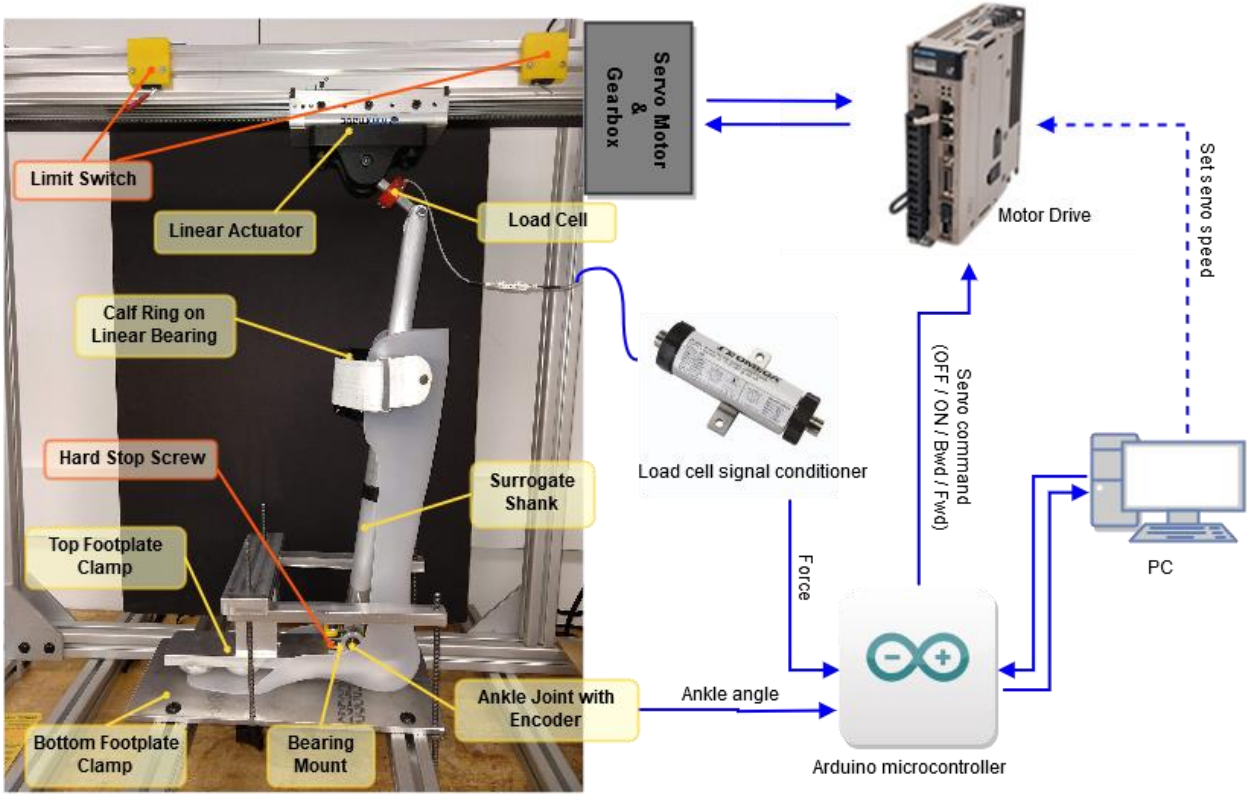

Figure C1: Component of the SMApp machine developed by Barton Research Group at the University of Michigan

The tested stiffness curves with AFO reaction torques versus bending angles are shown in Figure C2. Linear regressions were performed to test the linear relationship between the reaction torque and bending angles, as well as the changes in AFO stiffness before and after the trials. The linear regression slope (stiffness), intercept, and goodness of fitting are shown in Table C1. The differences in the slope, or stiffness of the AFOs between before trials and after trials were less than 2%, which was considered insignificant changes in AFO stiffness.

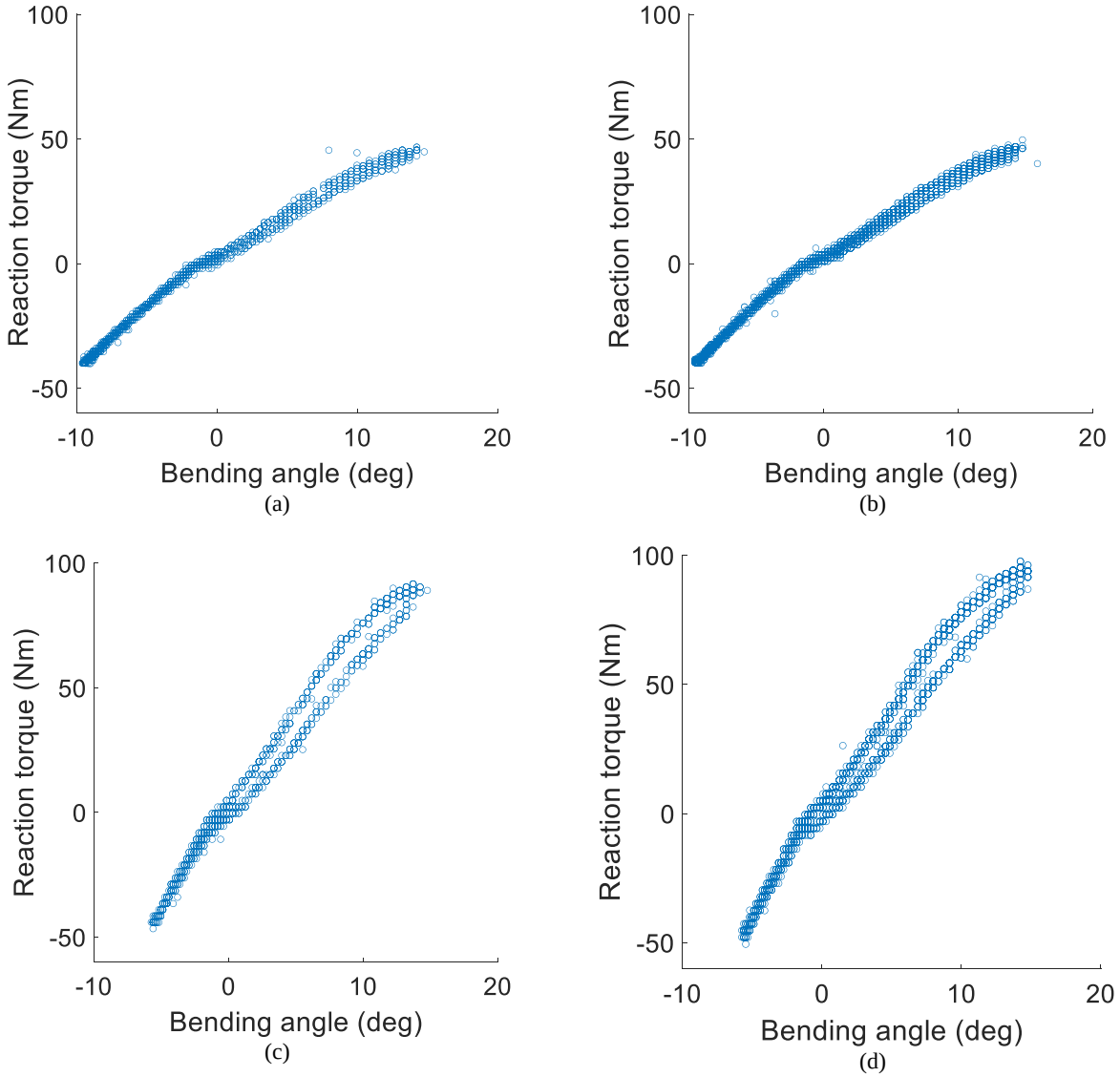

Figure C2: The stiffness plots for (a) AFO1 before the trials, (b) AFO1 after the trials, (c) AFO2 before the trials, and (d) AFO2 after the trials.

Table C1: The slope, intercept, and goodness of fitting of the linear regression between reaction torque and bending angle

		Slope	Intercept	Goodness of Fitting
AFO1	Before trials	3.64	0.009	0.98
	After trials	3.60	0.086	0.99
	Error in Slope (%)	1.1	-	-
AFO2	Before trials	6.87	0.074	0.98
	After trials	6.96	−0.020	0.98
	Error in Slope (%)	1.3	-	-

Appendix D: Observed and Predicted Initial Angles and Angular Velocities in Chapter 4

The initial angles and angular velocities for six subjects are presented in Table D1.

Table D1. Observed (O) and predicted (P) initial angles (initial shank pitch angle $\theta(t_0)$, back-hip angle $\theta_{11}(t_0)$, and back-ankle angle $\theta_{13}(t_0)$) and angular velocities (shank pitch angular velocity $\dot{\theta}(t_0)$, back-hip angular velocity $\dot{\theta}_{11}(t_0)$, and back-ankle angular velocity $\dot{\theta}_{13}(t_0)$) for 40 gait cycles (n = 40) for each subjects under each condition.

Subject		1			2			3		
Condition		NAFO	AFO1	AFO2	NAFO	AFO1	AFO2	NAFO	AFO1	AFO2
$\theta(t_0)$	O	65±4	69±2	53±9	42±16	36±15	43±5	57±7	50±13	47±5
	P	77±14	77±9	65±13	32±17	28±16	53±7	48±7	38±13	37±5
	RMSE	18	8	13	14	10	11	14	15	13
$\dot{\theta}(t_0)$	O	112±22	118±19	153±19	110±25	157±24	104±14	141±17	119±15	100±13
	P	125±14	162±14	113±26	117±28	168±27	104±13	145±15	123±17	80±21
	RMSE	18	58	52	9	16	5	5	4	28
$\theta_{11}(t_0)$	O	−11±2	−30±12	−16±2	−28±4	−11±1	−9±4	−11±5	−19±1	−19±4
	P	−21±5	−20±3	−25±6	−29±5	−11±1	−21±5	−20±4	−15±5	−31±5
	RMSE	14	13	12	1	2	15	11	5	15
$\dot{\theta}_{11}(t_0)$	O	179±24	147±24	80±19	94±29	106±29	72±8	126±27	199±23	134±14
	P	138±8	116±19	105±15	110±23	121±13	72±8	130±13	150±10	134±13
	RMSE	50	38	25	38	19	10	5	59	5
$\theta_{13}(t_0)$	O	−14±1	−19±2	−16±2	−31±5	−20±2	−12±6	−38±7	−29±2	−27±6
	P	−24±6	−30±9	−18±4	−31±6	−22±3	−22±8	−38±8	−28±3	−17±5
	RMSE	13	11	2	4	3	18	2	1	12
$\dot{\theta}_{13}(t_0)$	O	154±27	118±26	103±21	129±26	165±22	147±16	160±12	145±20	54±6
	P	131±46	119±13	126±23	125±32	183±42	147±16	163±9	150±22	54±6
	RMSE	39	1	33	5	26	2	4	7	3
Subject		4			5			6		
Condition		NAFO	AFO1	AFO2	NAFO	AFO1	AFO2	NAFO	AFO1	AFO2
$\theta(t_0)$	O	49±6	67±10	53±17	54±6	44±7	38±4	49±12	68±9	76±13
	P	56±7	65±10	43±17	51±7	45±5	44±4	53±11	65±10	74±14
	RMSE	9	7	12	4	1	9	6	3	2
$\dot{\theta}(t_0)$	O	139±12	159±25	163±22	131±17	121±5	129±10	146±17	161±26	154±24
	P	123±11	141±6	156±23	143±27	160±41	160±13	145±21	163±12	161±8
	RMSE	19	2	3	16	45	31	1	3	9
$\theta_{11}(t_0)$	O	−23±3	−22±6	−22±4	−8±3	−21±4	−23±3	−29±6	−11±1	−16±7
	P	−21±3	−27±6	−24±4	−14±4	−17±10	−16±5	−29±7	−15±1	−21±8
	RMSE	2	10	4	7	4	9	2	4	7
$\dot{\theta}_{11}(t_0)$	O	113±12	133±23	246±28	250±15	156±15	184±17	275±14	320±28	201±13
	P	136±15	154±25	226±8	280±25	166±28	196±23	287±30	316±19	210±27
	RMSE	25	26	26	33	15	17	14	6	11
$\theta_{13}(t_0)$	O	−34±7	−18±9	−14±5	−39±3	−36±6	−20±3	−32±12	−26±8	−17±2
	P	−37±7	−26±9	−14±3	−40±17	−33±4	−23±3	−35±12	−24±8	−25±3
	RMSE	3	9	0	1	4	4	4	3	11
$\dot{\theta}_{13}(t_0)$	O	162±17	103±13	60±22	123±22	160±14	97±13	191±23	262±14	141±12
	P	133±14	147±19	91±24	116±23	184±16	120±28	193±10	269±23	131±19
	RMSE	36	50	32	10	25	28	2	8	14

Appendix E: Surface Electromyography (SEMG) Signals and the Hip and Knee Lumped Muscle Parameters of the Swing Phase (SW) and Double Stance Phase (DS) in Chapter 4

There are SEMG RMS of BFs and RFs and hip and knee lumped muscle parameters during SW and DS for six subjects under three conditions presented in Table E1.

Table E1. The measured SEMG root mean square (RMS) for left biceps femoris (lBF), left rectus femoris (lRF), right biceps femoris (rBF), and right rectus femoris (rRF), and the predicted hip and knee lumped muscle parameters during the SW and DS. n = 40 for each subject under each condition.

	Subject		1			2			3		
Phase	Condition		NAFO	AFO1	AFO2	NAFO	AFO1	AFO2	NAFO	AFO1	AFO2
SW	SEMG RMS (mV)	lBF	65±4	69±2	53±19	42±16	36±15	43±5	57±7	50±13	47±5
		lRF	87±14	77±9	75±13	32±17	28±16	63±7	38±7	38±13	37±5
		rBF	66±22	69±19	87±19	65±25	89±24	64±14	31±7	70±25	60±13
		rRF	73±14	116±24	67±16	69±8	94±27	62±13	33±5	72±17	100±21
	Left hip parameter (Nm/deg)		21±2	30±12	26±2	28±4	11±4	29±4	21±5	39±10	29±4
	Right hip parameter (Nm/deg)		21±11	20±3	25±6	29±5	11±5	41±5	20±4	35±5	41±5
	Left knee parameter (Nm/deg)		9±3	9±2	12±4	9±3	12±5	8±3	11±4	8±3	9±1
	Right knee parameter (Nm/deg)		11±2	9±2	11±2	9±3	12±3	8±2	10±1	10±2	9±1
DS	SEMG RMS (mV)	lBF	23±14	19±7	15±3	46±2	46±4	44±3	68±9	76±17	28±10
		lRF	17±4	26±4	25±12	49±6	46±3	44±5	46±11	51±18	21±4
		rBF	32±12	28±13	32±12	54±5	55±4	56±2	57±1	56±1	57±2
		rRF	45±24	21±9	36±12	52±12	53±11	57±10	57±1	55±1	55±1
	Left hip parameter (Nm/deg)		16±3	18±2	15±2	22±7	17±4	18±3	24±9	19±9	17±3
	Right hip parameter (Nm/deg)		15±5	18±5	15±5	20±5	13±15	4±2	13±15	19±9	2±2
	Left knee parameter (Nm/deg)		13±3	15±4	13±4	15±2	17±5	17±3	15±3	16±1	18±1
	Right knee parameter (Nm/deg)		15±1	16±6	17±2	16±4	21±7	16±3	20±4	20±3	22±2
	Subject		4			5			6		
	Condition		NAFO	AFO1	AFO2	NAFO	AFO1	AFO2	NAFO	AFO1	AFO2
SW	SEMG RMS (mV)	lBF	49±6	67±20	53±7	54±6	44±7	38±4	49±22	68±19	76±23
		lRF	56±7	85±20	43±7	51±7	45±5	44±4	53±21	65±10	74±24
		rBF	60±12	90±15	92±12	56±17	76±25	50±20	85±17	71±6	92±14
		rRF	52±11	91±16	93±13	62±17	95±11	65±13	87±11	72±12	96±28
	Left hip parameter (Nm/deg)		23±3	32±6	22±4	18±3	21±4	23±3	29±6	11±5	16±7
	Right hip parameter (Nm/deg)		21±3	47±6	34±4	14±4	17±4	16±5	29±7	15±4	31±8
	Left knee parameter (Nm/deg)		12±3	10±4	9±1	9±4	8±3	12±4	11±2	13±1	10±4
	Right knee parameter (Nm/deg)		9±2	9±5	11±3	12±4	10±3	13±3	13±1	13±4	12±2
DS	SEMG RMS (mV)	lBF	13±4	19±4	23±8	16±8	18±3	11±2	28±3	45±4	47±3
		lRF	20±5	20±6	27±10	21±12	29±4	11±5	25±5	47±8	48±13
		rBF	23±1	37±1	19±2	18±1	19±1	19±6	17±1	37±1	48±3
		rRF	15±10	38±3	18±3	17±6	20±2	13±5	20±3	37±1	47±5
	Left hip parameter (Nm/deg)		31±2	32±6	24±1	25±4	36±6	18±3	28±4	22±4	26±12
	Right hip parameter (Nm/deg)		38±4	37±5	32±3	32±5	27±5	23±3	35±5	32±6	35±4
	Left knee parameter (Nm/deg)		16±1	14±3	13±8	21±2	23±3	24±4	25±5	25±7	29±5
	Right knee parameter (Nm/deg)		22±5	25±3	25±9	22±5	22±6	24±1	27±4	24±2	22±7

Appendix F: Observed and Predicted Step Lengths, Swing Time, and Walking Speeds

There are observed and predicted step lengths, swing time, and walking speeds for six subjects under three conditions presented in Table F1.

Table F1. Observed (O) and predicted (P) step lengths, swing time, and walking speed for six subjects with 40 gait cycles (n = 40) for each subject under each condition.

	Subject		1			2			3		
	Condition		NAFO	AFO1	AFO2	NAFO	AFO1	AFO2	NAFO	AFO1	AFO2
Step Length (m)	L	O	0.34±0.04	0.27±0.02	0.38±0.02	0.43±0.06	0.37±0.03	0.46±0.05	0.46±0.06	0.51±0.05	0.61±0.05
		P	0.40±0.07	0.23±0.08	0.36±0.06	0.42±0.07	0.44±0.08	0.44±0.08	0.45±0.07	0.51±0.11	0.65±0.06
		RMSE	0.11	0.12	0.10	0.12	0.12	0.08	0.07	0.05	0.10
	R	O	0.32±0.03	0.24±0.05	0.21±0.03	0.46±0.06	0.34±0.04	0.30±0.03	0.48±0.07	0.38±0.04	0.37±0.03
		P	0.33±0.05	0.20±0.05	0.30±0.10	0.49±0.04	0.32±0.16	0.27±0.13	0.46±0.13	0.41±0.15	0.37±0.11
		RMSE	0.13	0.12	0.16	0.11	0.14	0.13	0.11	0.12	0.07
Swing Time (s)	L	O	0.35±0.03	0.42±0.06	0.34±0.06	0.33±0.07	0.39±0.02	0.31±0.06	0.35±0.1	0.36±0.02	0.36±0.01
		P	0.36±0.01	0.40±0.07	0.34±0.04	0.33±0.01	0.40±0.03	0.29±0.01	0.35±0.02	0.37±0.01	0.36±0.05
		RMSE	0.01	0.03	0.01	0.01	0.01	0.03	0.02	0.02	0.02
	R	O	0.35±0.05	0.38±0.05	0.36±0.02	0.37±0.08	0.31±0.09	0.39±0.07	0.35±0.07	0.34±0.08	0.34±0.09
		P	0.36±0.03	0.35±0.03	0.38±0.03	0.37±0.04	0.32±0.01	0.37±0.06	0.36±0.05	0.35±0.07	0.32±0.1
		RMSE	0.03	0.04	0.03	0.03	0.03	0.04	0.02	0.03	0.03
Speed (m/s)		O	0.61±0.07	0.55±0.07	0.65±0.05	0.63±0.12	0.59±0.07	0.51±0.08	0.73±0.13	0.64±0.09	0.73±0.08
		P	0.68±0.09	0.46±0.11	0.73±0.13	0.65±0.14	0.63±0.14	0.48±0.11	0.71±0.05	0.66±0.16	0.76±0.17
		RMSE	0.16	0.12	0.14	0.12	0.16	0.15	0.13	0.13	0.14
	Subject		4			5			6		
	Condition		NAFO	AFO1	AFO2	NAFO	AFO1	AFO2	NAFO	AFO1	AFO2
Step Length (m)	L	O	0.37±0.05	0.35±0.01	0.38±0.06	0.56±0.06	0.54±0.05	0.66±0.07	0.54±0.03	0.62±0.03	0.62±0.03
		P	0.36±0.07	0.38±0.19	0.33±0.05	0.50±0.10	0.47±0.05	0.66±0.07	0.53±0.11	0.65±0.13	0.64±0.19
		RMSE	0.07	0.10	0.06	0.06	0.08	0.05	0.02	0.04	0.03
	R	O	0.39±0.06	0.36±0.05	0.28±0.04	0.51±0.04	0.47±0.05	0.44±0.02	0.58±0.05	0.60±0.06	0.57±0.05
		P	0.37±0.13	0.32±0.32	0.29±0.04	0.48±0.08	0.43±0.02	0.45±0.08	0.56±0.18	0.61±0.19	0.57±0.15
		RMSE	0.11	0.13	0.12	0.09	0.07	0.09	0.03	0.04	0.01
Swing Time (s)	L	O	0.41±0.13	0.36±0.08	0.31±0.04	0.31±0.04	0.34±0.05	0.31±0.01	0.34±0.04	0.33±0.01	0.38±0.06
		P	0.40±0.09	0.36±0.08	0.31±0.06	0.32±0.06	0.36±0.12	0.30±0.02	0.34±0.03	0.33±0.04	0.36±0.09
		RMSE	0.01	0.01	0.01	0.01	0.02	0.01	0.01	0.01	0.02
	R	O	0.39±0.05	0.34±0.07	0.39±0.11	0.39±0.05	0.36±0.03	0.39±0.02	0.36±0.01	0.30±0.08	0.32±0.09
		P	0.39±0.08	0.31±0.05	0.39±0.07	0.39±0.05	0.37±0.04	0.37±0.03	0.37±0.03	0.30±0.06	0.29±0.02
		RMSE	0.02	0.03	0.02	0.04	0.03	0.04	0.02	0.03	0.03
Speed (m/s)		O	0.75±0.11	0.65±0.06	0.46±0.1	1.05±0.1	1±0.1	1.16±0.09	1±0.08	1.12±0.09	1.23±0.08
		P	0.72±0.12	0.64±0.11	0.43±0.09	0.96±0.18	0.89±0.07	1.17±0.11	0.97±0.19	1.16±0.12	1.25±0.14
		RMSE	0.04	0.03	0.04	0.11	0.12	0.05	0.04	0.05	0.02

Appendix G: Webpage for Demonstration of Model Application

The webpage link is http://www-personal.umich.edu/~qifu/pendulum/flexPend.html. A screenshot of the webpage is shown in Figure G1.

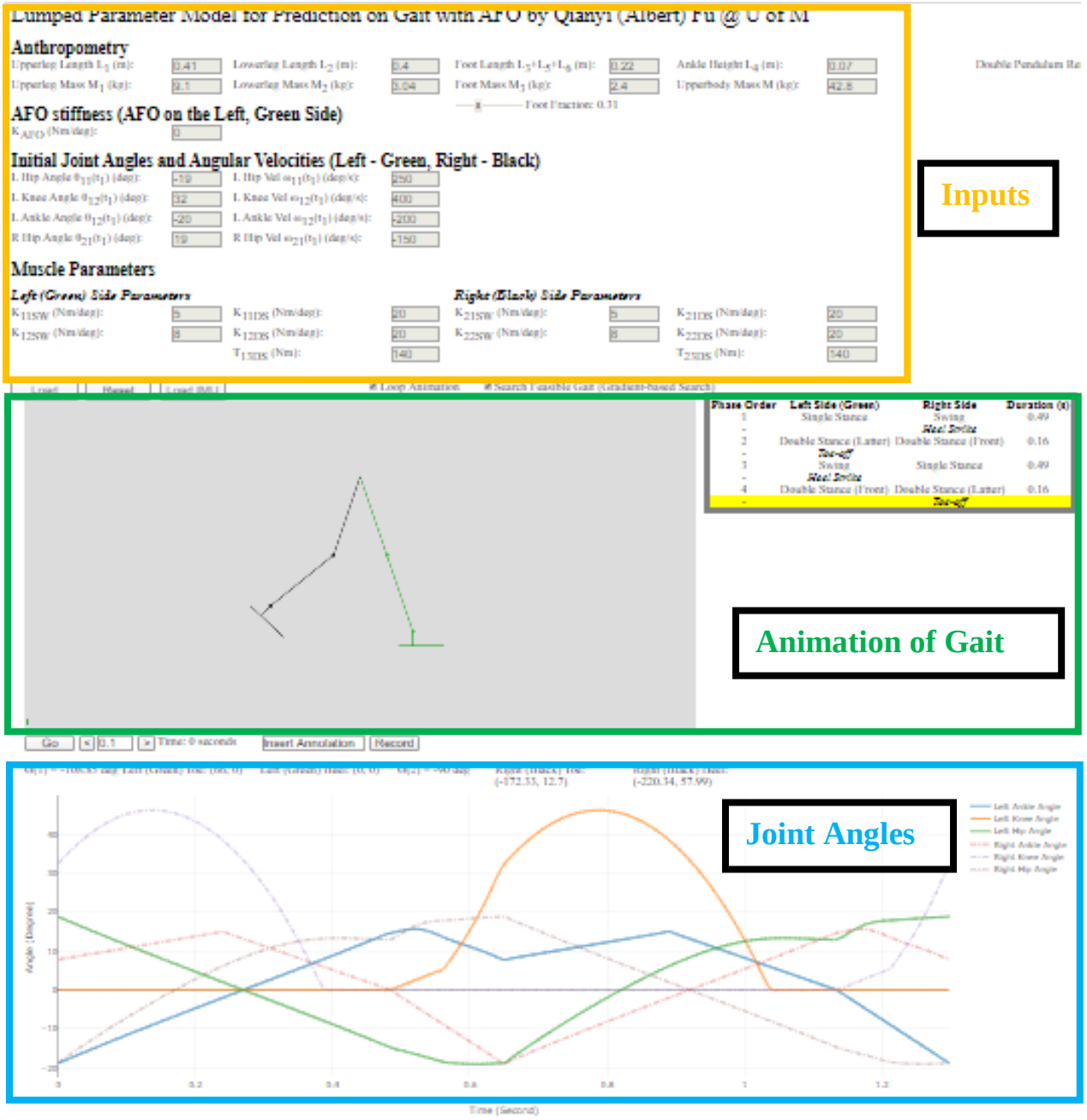

Figure G1. The webpage with input predicted animation of gait and joint angles for demonstration of model application.

REFERENCES

[1] S.J. Dixon, R.S. Hinman, M.W. Creaby, G. Kemp, K.M. Crossley, Knee joint stiffness during walking in knee osteoarthritis, Arthritis Care Res. (2010). https://doi.org/10.1002/acr.20012.

[2] S. Kuitunen, P. V. Komi, H. Kyröläinen, Knee and ankle joint stiffness in sprint running, Med. Sci. Sports Exerc. (2002). https://doi.org/10.1097/00005768-200201000-00025.

[3] R.B. Davis, P.A. DeLuca, Gait characterization via dynamic joint stiffness, Gait Posture. (1996). https://doi.org/10.1016/0966-6362(95)01045-9.

[4] K. Kubo, M. Morimoto, T. Komuro, N. Tsunoda, H. Kanehisa, T. Fukunaga, Influences of tendon stiffness, joint stiffness, and electromyographic activity on jump performances using single joint, Eur. J. Appl. Physiol. (2007). https://doi.org/10.1007/s00421-006-0338-y.

[5] A.I.R. Kottink, L.J.M. Oostendorp, J.H. Buurke, A. V. Nene, H.J. Hermens, M.J. IJzerman, The orthotic effect of functional electrical stimulation on the improvement of walking in stroke patients with a dropped foot: A systematic review, Artif. Organs. (2004). https://doi.org/10.1111/j.1525-1594.2004.07310.x.

[6] C. Hodt-Billington, J.L. Helbostad, W. Vervaat, T. Rognsvåg, R. Moe-Nilssen, Criteria of gait asymmetry in patients with hip osteoarthritis, Physiother. Theory Pract. (2012). https://doi.org/10.3109/09593985.2011.574783.

[7] L. Wafai, A. Zayegh, J. Woulfe, S. Mahfuzul, R. Begg, Identification of foot pathologies based on plantar pressure asymmetry, Sensors (Switzerland). (2015). https://doi.org/10.3390/s150820392.

[8] R. Don, M. Serrao, P. Vinci, A. Ranavolo, A. Cacchio, F. Ioppolo, M. Paoloni, R. Procaccianti, F. Frascarelli, F. De Santis, F. Pierelli, M. Frascarelli, V. Santilli, Foot drop and plantar flexion failure determine different gait strategies in Charcot-Marie-Tooth patients, Clin. Biomech. (2007). https://doi.org/10.1016/j.clinbiomech.2007.06.002.

[9] J. Hughes, N. Jacobs, Normal human locomotion, Prosthet. Orthot. Int. (1979). https://doi.org/10.3109/03093647909164693.

[10] D.A. Winter, Overall principle of lower limb support during stance phase of gait, J. Biomech. (1980). https://doi.org/10.1016/0021-9290(80)90162-1.

[11] B.C.C. Khoo, J.C.H. Goh, K. Bose, A biomechanical model to determine lumbosacral loads during single stance phase in normal gait, Med. Eng. Phys. (1995). https://doi.org/10.1016/1350-4533(95)90374-K.

[12] B.R. Umberger, Stance and swing phase costs in human walking, J. R. Soc. Interface. (2010). https://doi.org/10.1098/rsif.2010.0084.

[13] D.A. Winter, Kinematic and kinetic patterns in human gait: Variability and compensating effects, Hum. Mov. Sci. (1984). https://doi.org/10.1016/0167-9457(84)90005-8.

[14] S.A. Gard, D.S. Childress, The influence of stance-phase knee flexion on the vertical displacement of the trunk during normal walking, Arch. Phys. Med. Rehabil. (1999). https://doi.org/10.1016/S0003-9993(99)90303-9.

[15] M.A. Moosabhoy, S.A. Gard, Methodology for determining the sensitivity of swing leg toe clearance and leg length to swing leg joint angles during gait, Gait Posture. (2006). https://doi.org/10.1016/j.gaitpost.2005.12.004.

[16] R. Drillis, R. Contini, Segment length expressed as ratio of body height, New York Off. Vocat. Rehabil. (1966).

[17] S. Mochon, T.A. McMahon, Ballistic walking: an improved model, Math. Biosci. (1980). https://doi.org/10.1016/0025-5564(80)90070-X.

[18] W.T. Dempster, Space requirements of the seated operator: geometrical, kinematic, and mechanical aspects other body with special reference to the limbs, 1955.

[19] D.W. Grieve, R.J. Gear, The relationships between length of stride, step frequency, time of swing and speed of walking for children and adults, Ergonomics. (1966). https://doi.org/10.1080/00140136608964399.

[20] A. Agrawal, S.K. Banala, S.K. Agrawal, S.A. Binder-Macleod, Design of a two degree-of-freedom ankle-foot orthosis for robotic rehabilitation, in: Proc. 2005 IEEE 9th Int. Conf. Rehabil. Robot., 2005. https://doi.org/10.1109/ICORR.2005.1501047.

[21] B.S. Borotikar, R. Newcomer, R. Koppes, S.G. McLean, Combined effects of fatigue and decision making on female lower limb landing postures: Central and peripheral contributions to ACL injury risk, Clin. Biomech. (2008). https://doi.org/10.1016/j.clinbiomech.2007.08.008.

[22] B. Mariani, S. Rochat, C.J. Büla, K. Aminian, Heel and toe clearance estimation for gait analysis using wireless inertial sensors, IEEE Trans. Biomed. Eng. (2012). https://doi.org/10.1109/TBME.2012.2216263.

[23] J.B. Saunders, V.T. Inman, H.D. Eberhart, The major determinants in normal and pathological gait., J. Bone Joint Surg. Am. (1953). https://doi.org/10.2106/00004623-195335030-00003.

[24] R.W. Selles, S. Korteland, A.J. Van Soest, J.B. Bussmann, H.J. Stam, Lower-leg inertial properties in transtibial amputees and control subjects and their influence on the swing phase during gait, Arch. Phys. Med. Rehabil. (2003). https://doi.org/10.1053/apmr.2003.50037.

[25] T. Orhanli, A. Yilmaz, Analysis of gait dynamics with the double pendulum model, in: 27th Signal Process. Commun. Appl. Conf. SIU 2019, 2019. https://doi.org/10.1109/SIU.2019.8806587.

[26] V. Carbone, M.M. van der Krogt, H.F.J.M. Koopman, N. Verdonschot, Sensitivity of subject-specific models to Hill muscle-tendon model parameters in simulations of gait, J. Biomech. (2016). https://doi.org/10.1016/j.jbiomech.2016.04.008.

[27] A.H. Hansen, D.S. Childress, S.C. Miff, S.A. Gard, K.P. Mesplay, The human ankle during walking: Implications for design of biomimetic ankle prostheses, J. Biomech. (2004). https://doi.org/10.1016/j.jbiomech.2004.01.017.

[28] S.M. Nacy, S.S. Hassan, M.Y. Hanna, A modified dynamic model of the human lower limb during complete gait cycle, Int. J. Od Mech. Eng. Robot. Res. (2013).

[29] M. Garcia, A. Chatterjee, A. Ruina, M. Coleman, The simplest walking model: stability, complexity, and scaling, J. Biomech. Eng. (1998). https://doi.org/10.1115/1.2798313.

[30] A.D. Kuo, J.M. Donelan, A. Ruina, Energetic consequences of walking like an inverted pendulum: Step-to-step transitions, Exerc. Sport Sci. Rev. (2005). https://doi.org/10.1097/00003677-200504000-00006.

[31] M. Srinivasan, A. Ruina, Computer optimization of a minimal biped model discovers walking and running, Nature. (2006). https://doi.org/10.1038/nature04113.

[32] P. Malcolm, W. Derave, S. Galle, D. De Clercq, A simple exoskeleton that assists plantarflexion can reduce the metabolic cost of human walking, PLoS One. (2013). https://doi.org/10.1371/journal.pone.0056137.

[33] K. Okusa, T. Kamakura, Fast gait parameter estimation for frontal view gait video data based on the model selection and parameter optimization approach, IAENG Int. J. Appl. Math. (2013).

[34] M.Y. Zarrugh, C.W. Radcliffe, Computer generation of human gait kinematics, J. Biomech. (1979). https://doi.org/10.1016/0021-9290(79)90149-0.

[35] Z. Svoboda, M. Janura, P. Kutilek, E. Janurova, Relationships between movements of the lower limb joints and the pelvis in open and closed kinematic chains during a gait cycle, J. Hum. Kinet. (2016). https://doi.org/10.1515/hukin-2015-0168.

[36] E.J. Benjamin, M.J. Blaha, S.E. Chiuve, M. Cushman, S.R. Das, R. Deo, S.D. De Ferranti, J. Floyd, M. Fornage, C. Gillespie, C.R. Isasi, M.C. Jim'nez, L.C. Jordan, S.E. Judd, D. Lackland, J.H. Lichtman, L. Lisabeth, S. Liu, C.T. Longenecker, R.H. MacKey, K. Matsushita, D. Mozaffarian, M.E. Mussolino, K. Nasir, R.W. Neumar, L. Palaniappan, D.K. Pandey, R.R. Thiagarajan, M.J. Reeves, M. Ritchey, C.J. Rodriguez, G.A. Roth, W.D. Rosamond, C. Sasson, A. Towfghi, C.W. Tsao, M.B. Turner, S.S. Virani, J.H. Voeks, J.Z. Willey, J.T. Wilkins, J.H.Y. Wu, H.M. Alger, S.S. Wong, P. Muntner, Heart disease and stroke statistics'2017 update: A report from the American Heart Association, Circulation. 135 (2017) e146–e603. https://doi.org/10.1161/CIR.0000000000000485.

[37] J.H. Burridge, D.E. Wood, P.N. Taylor, D.L. McLellan, Indices to describe different muscle activation patterns, identified during treadmill walking, in people with spastic drop-foot, Med. Eng. Phys. (2001). https://doi.org/10.1016/S1350-4533(01)00061-3.

[38] T.F. Novacheck, C. Beattie, A. Rozumalski, G. Gent, G. Kroll, Quantifying the spring-like properties of ankle-foot orthoses (AFOs), J. Prosthetics Orthot. (2007). https://doi.org/10.1097/JPO.0b013e31812e555e.

[39] D.J.J. Bregman, J. Harlaar, C.G.M. Meskers, V. de Groot, Spring-like ankle foot orthoses reduce the energy cost of walking by taking over ankle work, Gait Posture. (2012). https://doi.org/10.1016/j.gaitpost.2011.08.026.

[40] E. Russell Esposito, R. V. Blanck, N.G. Harper, J.R. Hsu, J.M. Wilken, How does ankle-foot orthosis stiffness affect gait in patients with lower limb salvage?, Clin. Orthop. Relat. Res. (2014). https://doi.org/10.1007/s11999-014-3661-3.

[41] Y.L. Kerkum, A.I. Buizer, J.C. Van Den Noort, J.G. Becher, J. Harlaar, M.A. Brehm, The effects of varying ankle foot orthosis stiffness on gait in children with spastic cerebral palsy who walk with excessive knee flexion, PLoS One. (2015). https://doi.org/10.1371/journal.pone.0142878.

[42] Q. Fu, T.J. Armstrong, A. Shih, Development of a decision support system for ankle-foot orthosis (AFO) design based on lumped parameter models for human locomotion prediction, Proc. Hum. Factors Ergon. Soc. Annu. Meet. (2019). https://doi.org/10.1177/1071181319631194.

[43] J.H. Yoo, M.S. Nixon, C.J. Harris, Extracting human gait signatures by body segment properties, in: Proc. IEEE Southwest Symp. Image Anal. Interpret., 2002. https://doi.org/10.1109/IAI.2002.999885.

[44] A.I. Mahyuddin, S. Mihradi, T. Dirgantara, A. Sukmajaya, N. Juliyad, U. Purba, Development of an affordable system for 2D kinematics and dynamics analysis of human gait, in: Fourth Int. Conf. Exp. Mech., 2009. https://doi.org/10.1117/12.851654.

[45] A.R. Pangesti, E. Utami, A. Sunyoto, Analysis of inverse kinematics method for human movement in 2D animation, in: 2019 1st Int. Conf. Cybern. Intell. Syst. ICORIS 2019, 2019. https://doi.org/10.1109/ICORIS.2019.8874870.

[46] M.S. Ju, J.M. Mansour, Simulation of the double limb support phase of human gait, J. Biomech. Eng. (1988). https://doi.org/10.1115/1.3108435.

[47] B. Koopman, H.J. Grootenboer, H.J. de Jongh, An inverse dynamics model for the analysis, reconstruction and prediction of bipedal walking, J. Biomech. (1995). https://doi.org/10.1016/0021-9290(94)00185-7.

[48] A.H. Hansen, D.S. Childress, E.H. Knox, Roll-over shapes of human locomotor systems: Effects of walking speed, Clin. Biomech. (2004). https://doi.org/10.1016/j.clinbiomech.2003.12.001.

[49] A.P. Dempster, Upper and lower probability inferences based on a sample from a finite univariate population., Biometrika. (1967). https://doi.org/10.1093/biomet/54.3-4.515.

[50] S. Xiong, R. Goonetilleke, C. Witana, E. Lee Au, Modelling foot height and foot shape-related dimensions, Ergonomics. (2008). https://doi.org/10.1080/00140130801996147.

[51] C. Price, C. Nester, Foot dimensions and morphology in healthy weight, overweight and obese males, Clin. Biomech. (2016). https://doi.org/10.1016/j.clinbiomech.2016.07.003.

[52] M.M. Roberts, Common Conditions of the Foot and Ankle : An Overview, HSS. (2017). https://www.hss.edu/conditions_common-conditions-foot-ankle-overview.asp (accessed February 2, 2020).

[53] C.C. Gordon, T. Churchill, C.E. Clauser, J.T. Mcconville, I. Tebbetts, R.A. Walker, 1988 anthropometric survey of U . S . Army personnel : Methods and summary statistics, Security. (2012) 640.

[54] V.I. Arnold, V. V. Kozlov, A.I. Neishtadt, Variational Principles and Methods, in: 2006. https://doi.org/10.1007/978-3-540-48926-9_4.

[55] F.L. Buczek, M.J. Rainbow, K.M. Cooney, M.R. Walker, J.O. Sanders, Implications of using hierarchical and six degree-of-freedom models for normal gait analyses, Gait Posture. (2010). https://doi.org/10.1016/j.gaitpost.2009.08.245.

[56] T.D. Collins, S.N. Ghoussayni, D.J. Ewins, J.A. Kent, A six degrees-of-freedom marker set for gait analysis: Repeatability and comparison with a modified Helen Hayes set, Gait Posture. (2009). https://doi.org/10.1016/j.gaitpost.2009.04.004.

[57] M. Eltoukhy, J. Oh, C. Kuenze, J. Signorile, Improved kinect-based spatiotemporal and kinematic treadmill gait assessment, Gait Posture. (2017). https://doi.org/10.1016/j.gaitpost.2016.10.001.

[58] H.K. Ramakrishnan, M.P. Kadaba, On the estimation of joint kinematics during gait, J. Biomech. (1991). https://doi.org/10.1016/0021-9290(91)90175-M.

[59] S. Tadano, R. Takeda, H. Miyagawa, Three dimensional gait analysis using wearable acceleration and gyro sensors based on quaternion calculations, Sensors (Switzerland). (2013). https://doi.org/10.3390/s130709321.

[60] K. Tong, M.H. Granat, A practical gait analysis system using gyroscopes, Med. Eng. Phys. (1999). https://doi.org/10.1016/S1350-4533(99)00030-2.

[61] T. Seel, J. Raisch, T. Schauer, IMU-based joint angle measurement for gait analysis, Sensors (Switzerland). (2014). https://doi.org/10.3390/s140406891.

[62] R.K. Begg, W.A. Sparrow, Ageing effects on knee and ankle joint angles at key events and phases of the gait cycle, J. Med. Eng. Technol. (2006). https://doi.org/10.1080/03091900500445353.

[63] R.M. Kiss, L. Kocsis, Z. Knoll, Joint kinematics and spatial-temporal parameters of gait measured by an ultrasound-based system, Med. Eng. Phys. (2004). https://doi.org/10.1016/j.medengphy.2004.04.002.

[64] P.M. Mills, S. Morrison, D.G. Lloyd, R.S. Barrett, Repeatability of 3D gait kinematics obtained from an electromagnetic tracking system during treadmill locomotion, J. Biomech. (2007). https://doi.org/10.1016/j.jbiomech.2006.06.017.

[65] D. Totah, M. Menon, C. Jones-Hershinow, K. Barton, D.H. Gates, The impact of ankle-foot orthosis stiffness on gait: A systematic literature review, Gait Posture. (2019). https://doi.org/10.1016/j.gaitpost.2019.01.020.

[66] R.O. Robinson, W. Herzog, B.M. Nigg, Use of force platform variables to quantify the effects of chiropractic manipulation on gait symmetry., J. Manipulative Physiol. Ther. (1987).

[67] M. Błazkiewicz, I. Wiszomirska, A. Wit, Comparison of four methods of calculating the symmetry of spatial-temporal parameters of gait, Acta Bioeng. Biomech. (2014). https://doi.org/10.5277/abb140104.

[68] E. Kodesh, M. Kafri, G. Dar, R. Dickstein, Walking speed, unilateral leg loading, and step symmetry in young adults, Gait Posture. (2012). https://doi.org/10.1016/j.gaitpost.2011.08.008.

[69] C.L. Lewis, D.P. Ferris, Walking with increased ankle pushoff decreases hip muscle moments, J. Biomech. (2008). https://doi.org/10.1016/j.jbiomech.2008.05.013.

[70] P. Malcolm, P. Fiers, V. Segers, I. Van Caekenberghe, M. Lenoir, D. De Clercq, Experimental study on the role of the ankle push off in the walk-to-run transition by means of a powered ankle-foot-exoskeleton, Gait Posture. (2009). https://doi.org/10.1016/j.gaitpost.2009.06.002.

[71] Q. Fu, T. Armstrong, A. Shih, The effects of passive ankle-foot orthotic devices' stiffness – application and limitation of 2D inverted pendulum gait model, in: Adv. Intell. Syst. Comput., 2019. https://doi.org/10.1007/978-3-319-96071-5_115.

[72] S. Rethlefsen, R. Kay, S. Dennis, M. Forstein, V. Tolo, The effects of fixed and articulated ankle-foot orthoses on gait patterns in subjects with cerebral palsy, J. Pediatr. Orthop. (1999). https://doi.org/10.1097/01241398-199907000-00009.

[73] Å. Bartonek, M. Eriksson, E.M. Gutierrez-Farewik, A new carbon fibre spring orthosis for children with plantarflexor weakness, Gait Posture. (2007). https://doi.org/10.1016/j.gaitpost.2006.07.013.

[74] A. Esquenazi, D. Ofluoglu, B. Hirai, S. Kim, The effect of an ankle-foot orthosis on temporal spatial parameters and asymmetry of gait in hemiparetic patients, PM R. (2009). https://doi.org/10.1016/j.pmrj.2009.09.012.

[75] F. Danion, M. Bonnard, J. Pailhous, Intentional on-line control of propulsive forces in human gait, Exp. Brain Res. (1997). https://doi.org/10.1007/PL00005781.

[76] J.M. Font-Llagunes, J. Kovecses, Efficient dynamic walking: Design strategies to reduce energetic losses of a compass walker at heel strike, Mech. Based Des. Struct. Mach. (2009). https://doi.org/10.1080/15397730902810234.

[77] M.L. Kaplan, J.H. Heegaard, Energy-conserving impact algorithm for the heel-strike phase of gait, J. Biomech. (2000). https://doi.org/10.1016/S0021-9290(00)00006-3.

[78] H.W. Park, S. Park, Increase of push-off propulsion to compensate heel strike loss during step-to-step transition is limited at faster gait speeds, Int. J. Precis. Eng. Manuf. (2013). https://doi.org/10.1007/s12541-013-0108-9.

[79] H.G. Kang, J.B. Dingwell, Separating the effects of age and walking speed on gait variability, Gait Posture. (2008). https://doi.org/10.1016/j.gaitpost.2007.07.009.

[80] O. Beauchet, G. Allali, C. Annweiler, S. Bridenbaugh, F. Assal, R.W. Kressig, F.R. Herrmann, Gait variability among healthy adults: Low and high stride-to-stride variability are both a reflection of gait stability, Gerontology. (2009). https://doi.org/10.1159/000235905.

[81] S. Shin, R.J. Valentine, E.M. Evans, J.J. Sosnoff, Lower extremity muscle quality and gait variability in older adults, Age Ageing. (2012). https://doi.org/10.1093/ageing/afs032.

[82] H.D. Lyons GM, Wilcox DJ, Lyons DJ, Evaluation of a drop foot stimulator FES intensity envelope matched to tibialis anterior muscle activity during walking, 5th Annu. Conf. Int. Funct. Electr. Stimul. Soc. (2000).

[83] J.F. Geboers, M.R. Drost, F. Spaans, H. Kuipers, H.A. Seelen, Immediate and long-term effects of ankle-foot orthosis on muscle activity during walking: A randomized study of patients with unilateral foot drop, Arch. Phys. Med. Rehabil. (2002). https://doi.org/10.1053/apmr.2002.27462.

[84] J. Romkes, A.K. Hell, R. Brunner, Changes in muscle activity in children with hemiplegic cerebral palsy while walking with and without ankle-foot orthoses, Gait Posture. (2006). https://doi.org/10.1016/j.gaitpost.2005.12.001.

[85] S. Zhu, H. Anderson, Y. Wang, A real-time on-chip algorithm for IMU-based gait measurement, in: Lect. Notes Comput. Sci. (Including Subser. Lect. Notes Artif. Intell. Lect. Notes Bioinformatics), 2012. https://doi.org/10.1007/978-3-642-34778-8_9.

[86] W. Kong, S. Sessa, S. Cosentino, M. Zecca, K. Saito, C. Wang, U. Imtiaz, Z. Lin, L. Bartolomeo, H. Ishii, T. Ikai, A. Takanishi, Development of a real-time IMU-based motion capture system for gait rehabilitation, in: 2013 IEEE Int. Conf. Robot. Biomimetics, ROBIO 2013, 2013. https://doi.org/10.1109/ROBIO.2013.6739779.

[87] J.R. Rebula, L. V. Ojeda, P.G. Adamczyk, A.D. Kuo, Measurement of foot placement and its variability with inertial sensors, Gait Posture. (2013). https://doi.org/10.1016/j.gaitpost.2013.05.012.

[88] S.J. Pittock, W.T. Mayr, R.L. McClelland, N.W. Jorgensen, S.D. Weigand, J.H. Noseworthy, B.G. Weinshenker, M. Rodriguez, Change in MS-related disability in a population-based cohort: A 10-year follow-up study, Neurology. (2004). https://doi.org/10.1212/01.WNL.0000101724.93433.00.

[89] C. Bulley, T.H. Mercer, J.E. Hooper, P. Cowan, S. Scott, M.L. Van Der Linden, Experiences of functional electrical stimulation (FES) and ankle foot orthoses (AFOs) for foot-drop in people with multiple sclerosis, Disabil. Rehabil. Assist. Technol. (2015). https://doi.org/10.3109/17483107.2014.913713.

[90] E.J. Benjamin, M.J. Blaha, S.E. Chiuve, M. Cushman, S.R. Das, R. Deo, S.D. De Ferranti, J. Floyd, M. Fornage, C. Gillespie, C.R. Isasi, M.C. Jim'nez, L.C. Jordan, S.E. Judd, D. Lackland, J.H. Lichtman, L. Lisabeth, S. Liu, C.T. Longenecker, R.H. MacKey, K. Matsushita, D. Mozaffarian, M.E. Mussolino, K. Nasir, R.W. Neumar, L. Palaniappan, D.K. Pandey, R.R. Thiagarajan, M.J. Reeves, M. Ritchey, C.J. Rodriguez, G.A. Roth, W.D. Rosamond, C. Sasson, A. Towfghi, C.W. Tsao, M.B. Turner, S.S. Virani, J.H. Voeks, J.Z. Willey, J.T. Wilkins, J.H.Y. Wu, H.M. Alger, S.S. Wong, P. Muntner, Heart disease and stroke statistics'2017 update: A report from the American Heart Association, Circulation. (2017). https://doi.org/10.1161/CIR.0000000000000485.

[91] S.I. Wolf, M. Alimusaj, O. Rettig, L. Döderlein, Dynamic assist by carbon fiber spring AFOs for patients with myelomeningocele, Gait Posture. (2008). https://doi.org/10.1016/j.gaitpost.2007.11.012.

[92] D. Cattaneo, F. Marazzini, A. Crippa, R. Cardini, Do static or dynamic AFOs improve balance?, Clin. Rehabil. (2002). https://doi.org/10.1191/0269215502cr547oa.

[93] L.R. Sheffler, M.T. Hennessey, J.S. Knutson, G.G. Naples, J. Chae, Functional effect of an ankle foot orthosis on gait in multiple sclerosis: A pilot study, Am. J. Phys. Med. Rehabil. (2008). https://doi.org/10.1097/PHM.0b013e31815b5325.

[94] S.A. Radtka, S.R. Skinner, M.E. Johanson, A comparison of gait with solid and hinged ankle-foot orthoses in children with spastic diplegic cerebral palsy, Gait Posture. (2005). https://doi.org/10.1016/j.gaitpost.2004.03.004.

[95] S. Õunpuu, K.J. Bell, R.B. Davis, P.A. DeLuca, An evaluation of the posterior leaf spring orthosis using joint kinematics and kinetics, J. Pediatr. Orthop. (1996). https://doi.org/10.1097/01241398-199605000-00017.

[96] D.J.J. Bregman, J. Harlaar, C.G.M. Meskers, V. de Groot, Spring-like Ankle Foot Orthoses reduce the energy cost of walking by taking over ankle work, Gait Posture. (2012). https://doi.org/10.1016/j.gaitpost.2011.08.026.

[97] J. Hendrickson, K.K. Patterson, E.L. Inness, W.E. McIlroy, A. Mansfield, Relationship between asymmetry of quiet standing balance control and walking post-stroke, Gait Posture. (2014). https://doi.org/10.1016/j.gaitpost.2013.06.022.

[98] K.K. Patterson, W.H. Gage, D. Brooks, S.E. Black, W.E. McIlroy, Evaluation of gait symmetry after stroke: A comparison of current methods and recommendations for standardization, Gait Posture. (2010). https://doi.org/10.1016/j.gaitpost.2009.10.014.

[99] M. Roerdink, P.J. Beek, Understanding inconsistent step-length asymmetries across hemiplegic stroke patients: Impairments and compensatory gait, Neurorehabil. Neural Repair. (2011). https://doi.org/10.1177/1545968310380687.

[100] J. Brincks, L.E. Christensen, M.V. Rehnquist, J. Petersen, H. Sorensen, U. Dalgas, Mildly disabled persons with multiple sclerosis use similar net joint power strategies as healthy controls when walking speed increases, NeuroRehabilitation. (2018). https://doi.org/10.3233/NRE-172225.

[101] J.L. Robinson, G.L. Smidt, Quantitative gait evaluation in the clinic, Phys. Ther. (1981). https://doi.org/10.1093/ptj/61.3.351.

[102] K.E. Webster, J.E. Wittwer, J.A. Feller, Quantitative gait analysis after medial unicompartmental knee arthroplasty for osteoarthritis, J. Arthroplasty. (2003). https://doi.org/10.1016/S0883-5403(03)00152-9.

[103] H. White, J. Jenkins, W.P. Neace, C. Tylkowski, J. Walker, Clinically prescribed orthoses demonstrate an increase in velocity of gait in children with cerebral palsy: A retrospective study, Dev. Med. Child Neurol. (2002). https://doi.org/10.1017.S0012162201001992.

[104] S.R. Simon, Quantification of human motion: Gait analysis - Benefits and limitations to its application to clinical problems, J. Biomech. (2004). https://doi.org/10.1016/j.jbiomech.2004.02.047.

[105] J.C. Hobart, S.J. Cano, J.P. Zajicek, A.J. Thompson, Rating scales as outcome measures for clinical trials in neurology: problems, solutions, and recommendations, Lancet Neurol. (2007). https://doi.org/10.1016/S1474-4422(07)70290-9.

[106] B. Bonnechère, B. Jansen, P. Salvia, H. Bouzahouene, L. Omelina, F. Moiseev, V. Sholukha, J. Cornelis, M. Rooze, S. Van Sint Jan, Validity and reliability of the Kinect within functional assessment activities: Comparison with standard stereophotogrammetry, Gait Posture. (2014). https://doi.org/10.1016/j.gaitpost.2013.09.018.

[107] A. Schmitz, M. Ye, R. Shapiro, R. Yang, B. Noehren, Accuracy and repeatability of joint angles measured using a single camera markerless motion capture system, J. Biomech. (2014). https://doi.org/10.1016/j.jbiomech.2013.11.031.

[108] C. Morrison, P. Culmer, H. Mentis, T. Pincus, Vision-based body tracking: turning Kinect into a clinical tool, Disabil. Rehabil. Assist. Technol. (2016). https://doi.org/10.3109/17483107.2014.989419.

[109] W. Li, J. Wang, Effective adaptive kalman filter for MEMS-IMU/magnetometers integrated attitude and heading reference systems, J. Navig. (2013). https://doi.org/10.1017/S0373463312000331.

[110] B.K. Santhiranayagam, D.T.H. Lai, W.A. Sparrow, R.K. Begg, A machine learning approach to estimate Minimum Toe Clearance using Inertial Measurement Units, J. Biomech. (2015). https://doi.org/10.1016/j.jbiomech.2015.10.040.

[111] C. Xu, J. He, X. Zhang, X. Zhou, S. Duan, Towards human motion tracking: Multi-sensory IMU/TOA fusion method and fundamental limits, Electron. (2019). https://doi.org/10.3390/electronics8020142.

[112] Q. Li, M. Young, V. Naing, J.M. Donelan, Walking speed estimation using a shank-mounted inertial measurement unit, J. Biomech. (2010). https://doi.org/10.1016/j.jbiomech.2010.01.031.

[113] B. Sijobert, J. Denys, C.A. Coste, C. Geny, IMU based detection of freezing of gait and festination in Parkinson's disease, in: 2014 IEEE 19th Int. Funct. Electr. Stimul. Soc. Annu. Conf. IFESS 2014 - Conf. Proc., 2014. https://doi.org/10.1109/IFESS.2014.7036751.

[114] A.T.M. Willemsen, F. Bloemhof, H.B.K. Boom, Automatic stance-swing phase detection from accelerometer data for peroneal nerve stimulation - Biomedical Engineering, IEEE Transactions on, IEEE Trans. Biomed. Eng. (1990).

[115] M. Millard, J. McPhee, E. Kubica, Multi-step forward dynamic gait simulation, in: Comput. Methods Appl. Sci., 2009. https://doi.org/10.1007/978-1-4020-8829-2_2.

[116] L. Ren, R.K. Jones, D. Howard, Predictive modelling of human walking over a complete gait cycle, J. Biomech. (2007). https://doi.org/10.1016/j.jbiomech.2006.07.017.

[117] S.S. Roy, D.K. Pratihar, Effects of turning gait parameters on energy consumption and stability of a six-legged walking robot, Rob. Auton. Syst. (2012). https://doi.org/10.1016/j.robot.2011.08.013.

[118] J.S. Arora, M.W. Huang, C.C. Hsieh, Methods for optimization of nonlinear problems with discrete variables: A review, Struct. Optim. (1994). https://doi.org/10.1007/BF01743302.

[119] S. Ermon, C.P. Gomes, A. Sabharwal, B. Selman, Embed and project: Discrete sampling with universal hashing, in: Adv. Neural Inf. Process. Syst., 2013.

[120] B.R. Chen, LEGSys: Wireless gait evaluation system using wearable sensors, in: Proc. - Wirel. Heal. 2011, WH'11, 2011. https://doi.org/10.1145/2077546.2077569.

[121] D. Stefanyshyn, C. Fusco, Athletics: Increased shoe bending stiffness increases sprint performance, Sport. Biomech. (2004). https://doi.org/10.1080/14763140408522830.

[122] M. Oleson, D. Adler, P. Goldsmith, A comparison of forefoot stiffness in running and running shoe bending stiffness, J. Biomech. (2005). https://doi.org/10.1016/j.jbiomech.2004.08.014.

[123] R. Brunner, G. Meier, T. Ruepp, Comparison of a stiff and a spring-type ankle-foot orthosis to improve gait in spastic hemiplegic children, J. Pediatr. Orthop. (1998). https://doi.org/10.1097/00004694-199811000-00005.

[124] H. Gök, A. Küçükdeveci, H. Altinkaynak, G. Yavuzer, S. Ergin, Effects of ankle-foot orthoses on hemiparetic gait, Clin. Rehabil. (2003). https://doi.org/10.1191/0269215503cr605oa.

[125] A.J. Ries, T.F. Novacheck, M.H. Schwartz, The efficacy of ankle-foot orthoses on improving the gait of children with diplegic cerebral palsy: A multiple outcome analysis, PM R. (2015). https://doi.org/10.1016/j.pmrj.2015.03.005.

[126] S.H. Cho, J.M. Park, O.Y. Kwon, Gender differences in three dimensional gait analysis data from 98 healthy Korean adults, Clin. Biomech. (2004). https://doi.org/10.1016/j.clinbiomech.2003.10.003.

[127] E.S. Chumanov, C. Wall-Scheffler, B.C. Heiderscheit, Gender differences in walking and running on level and inclined surfaces, Clin. Biomech. (2008). https://doi.org/10.1016/j.clinbiomech.2008.07.011.

[128] B. Guillebastre, P. Calmels, P. Rougier, Effects of rigid and dynamic Ankle-foot orthoses on normal gait, Foot Ankle Int. (2009). https://doi.org/10.3113/FAI.2009.0051.

[129] L.K. Smith, J.L. Lelas, D.C. Kerrigan, Gender differences in pelvic motions and center of mass displacement during walking: Stereotypes quantified, J. Women's Heal. (2002). https://doi.org/10.1089/15246090260137626.

[130] B. Stansfield, K. Hawkins, S. Adams, H. Bhatt, A mixed linear modelling characterisation of gender and speed related changes in spatiotemporal and kinematic characteristics of gait across a wide speed range in healthy adults, Med. Eng. Phys. (2018). https://doi.org/10.1016/j.medengphy.2018.07.015.

[131] P.J. Corcoran, R.H. Jebsen, G.L. Brengelmann, B.C. Simons, Effects of plastic and metal leg braces on speed and energy cost of hemiparetic ambulation., Arch. Phys. Med. Rehabil. (1970).

[132] A. Danielsson, K.S. Sunnerhagen, Energy expenditure in stroke subjects walking with a carbon composite ankle foot orthosis, J. Rehabil. Med. (2004). https://doi.org/10.1080/16501970410025126.

[133] M. Franceschini, M. Massucci, L. Ferrari, M. Agosti, C. Paroli, Effects of an ankle-foot orthosis on spatiotemporal parameters and energy cost of hemiparetic gait, Clin. Rehabil. (2003). https://doi.org/10.1191/0269215503cr622oa.

[134] J. Hassler, The Influence of Ankle-Foot Orthoses on Gait and Energy Expenditure in Spina Bifida, Pediatr. Phys. Ther. (2001). https://doi.org/10.1097/00001577-200113030-00009.

[135] J. Harlaar, J.G. Becher, C.J. Snijders, G.J. Lankhorst, Passive stiffness characteristics of ankle plantar flexors in hemiplegia, Clin. Biomech. (2000). https://doi.org/10.1016/S0268-0033(99)00069-8.

[136] H. Kerr Graham, J.A. Fixsen, Lengthening of the calcaneal tendon in spastic hemiplegia by the white slide technique. A long-term review, J. Bone Jt. Surg. - Ser. B. (1988). https://doi.org/10.1302/0301-620x.70b3.3372574.

[137] X. Zhou, L.F. Draganich, F. Amirouche, A dynamic model for simulating a trip and fall during gait, Med. Eng. Phys. (2002). https://doi.org/10.1016/S1350-4533(01)00125-4.

[138] M.P. Dillon, T.M. Barker, G. Pettet, Effect of inaccuracies in anthropometric data and linked-segment inverse dynamic modeling on kinetics of gait in persons with partial foot amputation, J. Rehabil. Res. Dev. (2008). https://doi.org/10.1682/JRRD.2007.11.0190.

[139] X.H. Duan, R.H. Allen, J.Q. Sun, A stiffness-varying model of human gait, Med. Eng. Phys. (1997). https://doi.org/10.1016/S1350-4533(97)00022-2.

[140] C. Vimieiro, E. Andrada, H. Witte, M. Pinotti, A computational model for dynamic analysis of the human gait, Comput. Methods Biomech. Biomed. Engin. (2015). https://doi.org/10.1080/10255842.2013.848859.

[141] A.D. Kuo, The six determinants of gait and the inverted pendulum analogy: A dynamic walking perspective, Hum. Mov. Sci. (2007). https://doi.org/10.1016/j.humov.2007.04.003.

[142] M. Iosa, G. Morone, F. Bini, A. Fusco, S. Paolucci, F. Marinozzi, The connection between anthropometry and gait harmony unveiled through the lens of the golden ratio, Neurosci. Lett. (2016). https://doi.org/10.1016/j.neulet.2015.12.023.

[143] M.P.T. Silva, J.A.C. Ambrósio, Sensitivity of the results produced by the inverse dynamic analysis of a human stride to perturbed input data, Gait Posture. (2004). https://doi.org/10.1016/S0966-6362(03)00013-4.

[144] T.A. Correa, R. Baker, H. Kerr Graham, M.G. Pandy, Accuracy of generic musculoskeletal models in predicting the functional roles of muscles in human gait, J. Biomech. (2011). https://doi.org/10.1016/j.jbiomech.2011.05.023.

[145] K.A. Myers, M. Wang, R.M. Marks, G.F. Harris, Validation of a multisegment foot and ankle kinematic model for pediatric gait, IEEE Trans. Neural Syst. Rehabil. Eng. (2004). https://doi.org/10.1109/TNSRE.2003.822758.

[146] P. Vergallo, A. Lay-Ekuakille, F. Angelillo, I. Gallo, A. Trabacca, Accuracy improvement in gait analysis measurements: Kinematic modeling, in: Conf. Rec. - IEEE Instrum. Meas. Technol. Conf., 2015. https://doi.org/10.1109/I2MTC.2015.7151587.

[147] R.A. Bogey, J. Perry, A.J. Gitter, An EMG-to-force processing approach for determining ankle muscle forces during normal human gait, IEEE Trans. Neural Syst. Rehabil. Eng. (2005). https://doi.org/10.1109/TNSRE.2005.851768.

[148] S. Õunpuu, D.A. Winter, Bilateral electromyographical analysis of the lower limbs during walking in normal adults, Electroencephalogr. Clin. Neurophysiol. (1989). https://doi.org/10.1016/0013-4694(89)90048-5.

[149] V. Leinonen, M. Kankaanpää, O. Airaksinen, O. Hänninen, Back and hip extensor activities during trunk flexion/extension: Effects of low back pain and rehabilitation, Arch. Phys. Med. Rehabil. (2000). https://doi.org/10.1053/apmr.2000.0810032.

[150] A.B. Arsenault, D.A. Winter, R.G. Marteniuk, Is there a “normal” profile of EMG activity in gait?, Med. Biol. Eng. Comput. (1986). https://doi.org/10.1007/BF02442685.

[151] E. Kellis, N. Galanis, N. Kofotolis, A. Hatzi, Effects of hip flexion angle on surface electromyographic activity of the biceps femoris and semitendinosus during isokinetic knee flexion, Muscles. Ligaments Tendons J. (2017). https://doi.org/10.11138/mltj/2017.7.2.286.

[152] A. Nene, C. Byrne, H. Hermens, Is rectus femoris really a part of quadriceps? Assessment of rectus femoris function during gait in able-bodied adults, Gait Posture. (2004). https://doi.org/10.1016/S0966-6362(03)00074-2.

[153] D.A. Winter, H.J. Yack, EMG profiles during normal human walking: stride-to-stride and inter-subject variability, Electroencephalogr. Clin. Neurophysiol. (1987). https://doi.org/10.1016/0013-4694(87)90003-4.

[154] P. Lawrenson, P. Hodges, K. Crossley, B. Vicenzino, M. McGorm, A. Semciw, The effect of altered stride length on iliocapsularis and pericapsular muscles of the anterior hip: An electromyography investigation during asymptomatic gait, Gait Posture. (2019). https://doi.org/10.1016/j.gaitpost.2019.04.003.

[155] J.D. Evans, Straightforward statistics for the behavioral sciences, Thomson Brooks/Cole Publishing Co., 1996.

[156] A. Findlow, J.Y. Goulermas, C. Nester, D. Howard, L.P.J. Kenney, Predicting lower limb joint kinematics using wearable motion sensors, Gait Posture. (2008). https://doi.org/10.1016/j.gaitpost.2007.11.001.

[157] J.Y. Goulermas, A.H. Findlow, C.J. Nester, P. Liatsis, X.J. Zeng, L.P.J. Kenney, P. Tresadern, S.B. Thies, D. Howard, An instance-based algorithm with auxiliary similarity information for the estimation of gait kinematics from wearable sensors, IEEE Trans. Neural Networks. (2008). https://doi.org/10.1109/TNN.2008.2000808.

[158] M.L. Psiaki, F. Martel, P.K. Pal, Three-axis attitude determination via kalman filtering of magnetometer data, J. Guid. Control. Dyn. (1990). https://doi.org/10.2514/3.25364.

[159] R. Richard, J. Weber, O. Mejjad, D. Polin, F. Dujardin, P. Pasquis, X. Le Loet, Spatiotemporal gait parameters measured using the bessou gait analyzer in 79 healthy subjects. Influence of age, stature, and gender, Rev. Du Rhum. (English Ed. (1995).

[160] R. Rastogi, I. Thaniarasu, S. Chandra, Design implications of walking speed for pedestrian facilities, J. Transp. Eng. (2011). https://doi.org/10.1061/(ASCE)TE.1943-5436.0000251.

[161] F. Di Nardo, A. Mengarelli, E. Maranesi, L. Burattini, S. Fioretti, Influence of gender on the myoelectric signal of shank muscles, in: MESA 2014 - 10th IEEE/ASME Int. Conf. Mechatron. Embed. Syst. Appl. Conf. Proc., 2014. https://doi.org/10.1109/MESA.2014.6935537.

[162] A. Elbaz, F. Artaud, A. Dugravot, C. Tzourio, A. Singh-Manoux, The gait speed advantage of taller stature is lost with age, Sci. Rep. (2018). https://doi.org/10.1038/s41598-018-19882-1.

[163] T. Oberg, A. Karsznia, K. Oberg, Basic gait parameters: Reference data for normal subjects, 10-79 years of age, J. Rehabil. Res. Dev. (1993).

[164] J.R. Franz, R. Kram, How does age affect leg muscle activity/coactivity during uphill and downhill walking?, Gait Posture. (2013). https://doi.org/10.1016/j.gaitpost.2012.08.004.

[165] T.E. Lockhart, J.M. Spaulding, S.H. Park, Age-related slip avoidance strategy while walking over a known slippery floor surface, Gait Posture. (2007). https://doi.org/10.1016/j.gaitpost.2006.08.009.

[166] A. Hill, The heat of shortening and the dynamic constants of muscle, Proc. R. Soc. London. Ser. B - Biol. Sci. (1938). https://doi.org/10.1098/rspb.1938.0050.

[167] F. Wikipedia, Hill's muscle model, (2014) 3–5. https://en.wikipedia.org/wiki/Hill%27s_muscle_model (accessed March 25, 2020).

[168] S.J. Crenshaw, T.D. Royer, J.G. Richards, D.J. Hudson, Gait variability in people with multiple sclerosis, Mult. Scler. (2006). https://doi.org/10.1177/1352458505070609.

[169] J.M. Huisinga, M. Mancini, R.J. St. George, F.B. Horak, Accelerometry reveals differences in gait variability between patients with multiple sclerosis and healthy controls, Ann. Biomed. Eng. (2013). https://doi.org/10.1007/s10439-012-0697-y.

[170] A. Shih, D.W. Park, Y.Y. Yang, R. Chisena, D. Wu, Cloud-based design and additive manufacturing of custom orthoses, in: Procedia CIRP, 2017. https://doi.org/10.1016/j.procir.2017.03.355.

[171] A. Domeika, V. Grigas, D. Satkunskiene, D. Satikas, I. Aleknaite-Dambrauskiene, Investigation of the ankle foot orthoses footplates stiffness, Mechanika. (2017). https://doi.org/10.5755/j01.mech.23.6.16901.

[172] T.W. Dorn, Y.C. Lin, M.G. Pandy, Estimates of muscle function in human gait depend on how foot-ground contact is modelled, Comput. Methods Biomech. Biomed. Engin. (2012). https://doi.org/10.1080/10255842.2011.554413.

[173] L.A. Gilchrist, D.A. Winter, A two-part, viscoelastic foot model for use in gait simulations, J. Biomech. (1996). https://doi.org/10.1016/0021-9290(95)00141-7.

[174] US Department of Health and Human Services, Bone health and osteoporosis: a report of the Surgeon General, US Heal. Hum. Serv. (2004). https://doi.org/10.2165/00002018-200932030-00004.

[175] J. Manrique, M.M. Gomez, J. Parvizi, Stiffness after total knee arthroplasty, J. Knee Surg. (2015). https://doi.org/10.1055/s-0034-1396079.

[176] M.F. Sowers, C.A. Karvonen-Gutierrez, M. Yosef, M. Jannausch, Y. Jiang, P. Garnero, J. Jacobson, Longitudinal changes of serum COMP and urinary CTX-II predict X-ray defined knee osteoarthritis severity and stiffness in women, Osteoarthr. Cartil. (2009). https://doi.org/10.1016/j.joca.2009.06.001.

[177] V.O. do C. Carvalhais, V.L. de Araújo, T.R. Souza, G.G.P. Gonçalves, J. de M. Ocarino, S.T. Fonseca, Validity and reliability of clinical tests for assessing hip passive stiffness, Man. Ther. (2011). https://doi.org/10.1016/j.math.2010.10.009.

[178] J. Zafereo, R. Devanna, E. Mulligan, S. Wang-Price, Hip stiffness patterns in lumbar flexion- or extension-based movement syndromes, Arch. Phys. Med. Rehabil. (2015). https://doi.org/10.1016/j.apmr.2014.09.023.

[179] S.R. Cummings, L.J. Melton, Osteoporosis I: Epidemiology and outcomes of osteoporotic fractures, Lancet. (2002). https://doi.org/10.1016/S0140-6736(02)08657-9.

[180] S. Hwang, J. Kim, J. Yi, K. Tae, K. Ryu, Y. Kim, Development of an active ankle foot orthosis for the prevention of foot drop and toe drag, in: ICBPE 2006 - Proc. 2006 Int. Conf. Biomed. Pharm. Eng., 2006.

https://doi.org/10.1109/ICBPE.2006.348627.

[181] S.M. Cain, K.E. Gordon, D.P. Ferris, Locomotor adaptation to a powered ankle-foot orthosis depends on control method, J. Neuroeng. Rehabil. (2007). https://doi.org/10.1186/1743-0003-4-48.

[182] X.S. Yang, S.S.S. Hosseini, A.H. Gandomi, Firefly Algorithm for solving non-convex economic dispatch problems with valve loading effect, Appl. Soft Comput. J. (2012). https://doi.org/10.1016/j.asoc.2011.09.017.

[183] S. Burer, A.N. Letchford, Non-convex mixed-integer nonlinear programming: A survey, Surv. Oper. Res. Manag. Sci. (2012). https://doi.org/10.1016/j.sorms.2012.08.001.

[184] P. Gong, C. Zhang, Z. Lu, J.Z. Huang, J. Ye, A general iterative shrinkage and thresholding algorithm for non-convex regularized optimization problems, in: 30th Int. Conf. Mach. Learn. ICML 2013, 2013.

[185] S. Marsland, Machine learning: An algorithmic perspective, 2014. https://doi.org/10.1201/b17476.

[186] J.F.E. IV, D. Michie, D.J. Spiegelhalter, C.C. Taylor, Machine learning, neural, and statistical classification., J. Am. Stat. Assoc. (1996). https://doi.org/10.2307/2291432.

[187] Y. Liu, A.E. Kerdok, R.D. Howe, A nonlinear finite element model of soft tissue indentation, Lect. Notes Comput. Sci. (Including Subser. Lect. Notes Artif. Intell. Lect. Notes Bioinformatics). (2004). https://doi.org/10.1007/978-3-540-25968-8_8.

[188] M. Fazil, K.R. Rajagopal, Nonlinear dynamic modeling of a single-phase permanent-magnet brushless DC motor using 2-D static finite-element results, IEEE Trans. Magn. (2011). https://doi.org/10.1109/TMAG.2010.2103955.

[189] A.K. Silverman, J.M. Wilken, E.H. Sinitski, R.R. Neptune, Whole-body angular momentum in incline and decline walking, J. Biomech. (2012). https://doi.org/10.1016/j.jbiomech.2012.01.012.

[190] N.T. Pickle, A.M. Grabowski, J.R. Jeffers, A.K. Silverman, The functional roles of muscles, passive prostheses, and powered prostheses during sloped walking in people with a transtibial amputation, J. Biomech. Eng. (2017). https://doi.org/10.1115/1.4037938.